

Summer 2014

Quantum levitation using metamaterials

Venkatesh K. Pappakrishnan
Louisiana Tech University

Follow this and additional works at: <https://digitalcommons.latech.edu/dissertations>

 Part of the [Condensed Matter Physics Commons](#), and the [Electromagnetics and Photonics Commons](#)

Recommended Citation

Pappakrishnan, Venkatesh K., "" (2014). *Dissertation*. 210.
<https://digitalcommons.latech.edu/dissertations/210>

This Dissertation is brought to you for free and open access by the Graduate School at Louisiana Tech Digital Commons. It has been accepted for inclusion in Doctoral Dissertations by an authorized administrator of Louisiana Tech Digital Commons. For more information, please contact digitalcommons@latech.edu.

QUANTUM LEVITATION USING METAMATERIALS

by

Venkatesh K. Pappakrishnan, B.E., M.S.

A Dissertation Presented in Partial Fulfillment
of the Requirements of the Degree
Doctor of Philosophy

COLLEGE OF ENGINEERING AND SCIENCE
LOUISIANA TECH UNIVERSITY

August 2014

UMI Number: 3662470

All rights reserved

INFORMATION TO ALL USERS

The quality of this reproduction is dependent upon the quality of the copy submitted.

In the unlikely event that the author did not send a complete manuscript and there are missing pages, these will be noted. Also, if material had to be removed, a note will indicate the deletion.

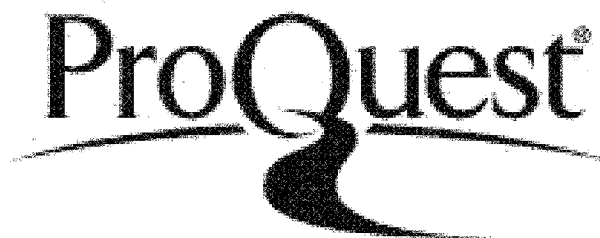


UMI 3662470

Published by ProQuest LLC 2015. Copyright in the Dissertation held by the Author.

Microform Edition © ProQuest LLC.

All rights reserved. This work is protected against unauthorized copying under Title 17, United States Code.



ProQuest LLC
789 East Eisenhower Parkway
P.O. Box 1346
Ann Arbor, MI 48106-1346

LOUISIANA TECH UNIVERSITY

THE GRADUATE SCHOOL

MAY 5, 2014

Date

We hereby recommend that the dissertation prepared under our supervision by
Venkatesh K. Pappakrishnan, B.E., M.S.

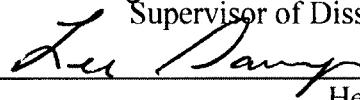
entitled Quantum Levitation using Metamaterials

be accepted in partial fulfillment of the requirements for the Degree of

Doctor of Philosophy in Engineering



Supervisor of Dissertation Research

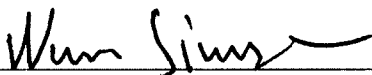


Head of Department

Physics

Department

Recommendation concurred in:



S. Zivanovic

Advisory Committee



Approved:



Director of Graduate Studies

Approved:



Dean of the Graduate School



Dean of the College

ABSTRACT

The emergence of an attractive vacuum force (Casimir force) between two purely dielectric materials can lead to an increase in the friction and the stiction effects in nanoscale devices, resulting in degradation or decreased performance. Thus, it is of high practical importance that the conditions for the reversal of the Casimir force from attractive to repulsive are identified. Although the repulsive Casimir force has been considered for high dielectric materials as an intermediate (between the plates) medium, so far no realistic system has been proposed that can demonstrate quantum levitation with air/vacuum as a host medium. Since air is the natural environment for almost all nano- and microscopic devices, it is therefore imperative to seek a better understanding of the nature of the Casimir force under such ambient conditions. In this thesis, the conditions for achieving quantum levitation at an arbitrary temperature are investigated by considering a simple configuration consisting of two parallel plates separated by air. The proposed parallel-plate designs are based on artificial nano-engineered electromagnetic materials commonly referred to as the electromagnetic metamaterials.

In the case of an ideal system consisting of non-dispersive plates, we have uncovered the existence of six universal Casimir force types. We have also derived an explicit necessary condition for Casimir force reversal as a function of the non-retarded specular functions of the plates. By introducing a modification of the Lifshitz theory, we have performed an extensive investigation of the Casimir force for general dispersive

magneto-dielectric plates. Simple necessary and sufficient conditions for force reversal have been derived that can serve as a useful tool in designing quantum levitation systems. Based on the sufficient condition, the complete parametric domain for the Casimir force repulsion has been identified. A strongly magnetic response for at least one of the plates is required to achieve quantum levitation with the air as an intermediate medium.

To achieve magnetism at high frequencies, we have considered three potential metamaterial designs based on the split ring resonators (SRRs), the parallel-wires, and the Ni-polystyrene nanocomposites. The SRRs and the parallel-wires composites are “diamagnetic”, whereas the Ni-polystyrene nanocomposites are paramagnetic in nature. By combining the above para- and diamagnetic metamaterial plates, we have demonstrated practically feasible designs of a quantum levitation system. If successfully implemented, the proposed designs could find applications in the frictionless bio-fluid transport devices, the micro and nano-accelerators, and as the coatings for an ultra-clean room environment.

APPROVAL FOR SCHOLARLY DISSEMINATION

The author grants to the Prescott Memorial Library of Louisiana Tech University the right to reproduce, by appropriate methods, upon request, any or all portions of this Dissertation. It is understood that "proper request" consists of the agreement, on the part of the requesting party, that said reproduction is for his personal use and that subsequent reproduction will not occur without written approval of the author of this Dissertation. Further, any portions of the Dissertation used in books, papers, and other works must be appropriately referenced to this Dissertation.

Finally, the author of this Dissertation reserves the right to publish freely, in the literature, at any time, any or all portions of this Dissertations.

Author John A. S.

Date 07/08/2014

DEDICATION

To

My parents,

Father, Pappakrishnan,

Mother, Kalarani,

who

taught me how to reach my goals.

TABLE OF CONTENTS

ABSTRACT.....	iii
DEDICATION.....	vi
LIST OF FIGURES	x
ACKNOWLEDGMENTS	xvi
CHAPTER 1 INTRODUCTION.....	1
1.1 Casimir Force.....	1
1.2 Vacuum Fluctuations	4
1.3 Casimir Force Between Two Parallel Metal Plates	7
1.4 Implications Due to the Attractive Nature of the Casimir Force.....	9
1.5 Repulsive Casimir Force and Applications	10
1.6 Casimir Force Reversal Strategies.....	11
1.6.1 Dzyaloshinskii’s Condition.....	12
1.6.2 Boyer’s Condition.....	12
1.6.3 Leonhardt and Philbin Condition.....	13
1.6.4 Proposed Systems with Repulsive Casimir Force	14
1.7 Related Research.....	14
1.8 Dissertation Overview	16
CHAPTER 2 CASIMIR FORCE THEORY.....	18
2.1 Introduction.....	18
2.2 Casimir Theory - Force Between Two Uncharged Metallic Plates.....	19
2.3 Lifshitz Formula - Force Between Two Uncharged Dielectric Plates.....	22

2.4	Casimir Force at Large Plate Separations.....	32
2.5	Casimir Force at Small Plate Separations.....	34
CHAPTER 3 CASIMIR FORCE BETWEEN TWO NONDISPERSIVE PARALLEL PLATES (IDEAL CASE).....		36
3.1	Casimir Force for Parallel-Plate Configurations	36
3.2	Attractive and Repulsive Casimir Forces	37
3.3	Repulsive Casimir Force Parametric Analysis	39
3.4	General Conditions for Repulsive Casimir Force.....	42
3.5	Challenges in Realizing the Six Universal Casimir Force Types.....	54
CHAPTER 4 CASIMIR FORCE BETWEEN A WEAKLY DISPERSIVE DIELECTRIC PLATE AND A METAMATERIAL PLATE		58
4.1	Introduction.....	58
4.2	Lorentz Oscillator Model for Dispersive Magneto-Dielectric Properties	59
4.3	Casimir Force Reversal at High and Low Temperatures.....	61
4.4	Upper Bound of the Casimir Force.....	63
4.5	Sufficient Condition.....	70
CHAPTER 5 CASIMIR FORCE BETWEEN A DIELECTRIC PLATE AND A METAMATERIAL PLATE.....		78
5.1	Introduction.....	78
5.2	Critical Mode Number for Casimir Force Repulsion	79
5.3	Upper Bound for the Casimir Force	81
5.4	Sufficient Condition for Repulsive Casimir Force	86
CHAPTER 6 ELECTROMAGNETIC METAMATERIALS		91
6.1	Introduction.....	91
6.2	Split Ring Resonators	94
6.2.1	Analytical Model for Split Ring Resonator Including Radiation Resistance.....	95

6.2.1.1	RLC Model of a Split Ring Resonator	95
6.2.1.2	Radiation Resistance of the SRR.....	100
6.2.2	Analytical Model for Split Ring Resonator Satisfying Causality	108
6.2.3	Permeability of the SRR at Imaginary Frequencies.....	112
6.3	Ferromagnetic Nanocomposites	114
6.4	Nanowire Composite Materials	117
CHAPTER 7 PRACTICAL MATERIAL CONFIGURATIONS FOR CASIMIR FORCE REVERSAL		121
7.1	Introduction.....	121
7.2	Materials with Dissimilar Magnetic and Electric Resonant Frequencies	122
7.3	A Dielectric Plate and a Magneto-Dielectric Plate	125
7.4	A Diamagnetic and a Paramagnetic Plate.....	129
CHAPTER 8 CONCLUSIONS AND FUTURE WORK.....		134
8.1	Conclusions.....	134
8.2	Future Work.....	136
BIBLIOGRAPHY		139

LIST OF FIGURES

Figure 1.1: Illustration which exemplifies the fact that, in free space, fluctuating modes of virtually arbitrary energies (depicted with different colors) can be manifested simultaneously [13].	6
Figure 1.2: Parallel semi-infinite metal plates separated by a distance d with vacuum fluctuations in between and on either side of the plates.	8
Figure 2.1: Semi-infinite parallel plates separated by a distance d .	23
Figure 3.1: Casimir forces (solid lines) and large distance asymptotic (dashed lines) for two different configurations. (a): $\epsilon_1 = 2, \mu_1 = 1, \epsilon_2 = 0.5,$ and $\mu_2 = 1$ (blue) and (b): $\epsilon_1 = 2, \mu_1 = 1, \epsilon_2 = 2,$ and $\mu_2 = 1$ (red).	38
Figure 3.2: Repulsive Casimir force domains according to Dzyaloshinskii's (yellow domain) and Kenneth <i>et al.</i> 's (gray domain) conditions and the LDA condition in Equation 3.2 (red domain, $F_{LDA} < 0$) for fixed permeability of plate 1: (a) $\mu_1 = 1$ and (b) $\mu_1 = 2$. The point A correspond to the values $\epsilon_1 = 2, \epsilon_2 = 2,$ and $\mu_2 = 6$ and similarly, the point B correspond to the values $\epsilon_1 = 10, \epsilon_2 = 2,$ and $\mu_2 = 10$.	40
Figure 3.3: Casimir force for the two configurations chosen from the parametric space in Figures 3.2 (a) and (b). A: $\epsilon_1 = 2, \mu_1 = 1, \epsilon_2 = 2,$ and $\mu_2 = 6,$ and B: $\epsilon_1 = 10, \mu_1 = 2, \epsilon_2 = 2,$ and $\mu_2 = 10$.	42
Figure 3.4: Force quadrants in terms of F_0 and F_∞ , showcasing the six universal types of the Casimir force.	47
Figure 3.5: (a) The weight function $W(s, m, q)$ for $m = 1$ (solid blue), $m = 3$ (dotted blue), and $m = 5$ (dashed blue) for fixed $s = 2$, and different values of $s = 0.001$ (solid red) and $s = 20$ (solid green) for fixed $m = 1$. (b) Plot of $\delta(s, m)$ normalized over its maximum value for $m = 1$, and for different plate separation distances $s = 0.001$ (solid red), $s = 2$ (solid blue), and $s = 20$ (solid green).	49
Figure 3.6: Parametric plot showcasing the parametric domains that identify the different types of the Casimir forces. The domains are plotted for fixed $\epsilon_1 = 5$ and $z_1 = 0.05$.	52

- Figure 3.7:** Six different types of the Casimir forces: ① type 1 (dashed orange), ② type 2 (dashed purple), ③ type 3 (dashed blue), ④ type 4 (dashed gray), ⑤ type 5 (green), and ⑥ type 6 (red)..... 53
- Figure 4.1:** The parametric domains corresponding to the cases where the upper bound (Equation 4.8) is not satisfied (red) and the force is repulsive $F < 0$ (blue). In the calculation we use $\epsilon_1 = 2$ and $n_s = 2$, (a) plotted in terms of z_2 and (b) plotted in terms of μ_2 65
- Figure 4.2:** (a) The Casimir force (solid lines) and its upper bound (dashed lines) calculated for two ratios of plate 2's dielectric and magnetic plasma frequencies $\omega_{pe2}/\omega_{pm2}$ and fixed $\omega_{om2}/\omega_T = 1$. (b) The temperature dependence of the force and its upper bound is calculated for different temperatures with fixed plasma and resonance frequencies $\omega_{pe2}/\omega_{pm2} = 0.25$, $\omega_{oe2}/\omega_{om2} = 2$, and $\omega_{pm2}/\omega_{om2} = 0.5$. The large distance F_∞ and the small distance F_0 asymptotic are included and in all calculations we have set plate 1's permittivity at $\epsilon_1 = 2$ 68
- Figure 4.3:** (a) Repulsive Casimir force domain according to Equation 4.14 (region *A*, blue) and Equation 4.12 (region *B*, gray). (b) The range of plate separation distances for force repulsion is calculated at fixed $\omega_{om2}/\omega_T = 1$, and $\omega_{pe2}/\omega_{pm2} = \omega_{pm2}/\omega_{om2} = 0.5$. The dots corresponds to the parametric domain for force reversal obtained through exact numerical solutions of the actual force given by Equation 2.35. In all cases we have set plate 1's permittivity at $\epsilon_1 = 2$ 69
- Figure 4.4:** Plot showing the $\omega_{pe2}/\omega_{pm2}$ required for achieving repulsion at different temperatures (a) $\omega_{om2}/\omega_T = 0.1$, (b) $\omega_{om2}/\omega_T = 0.4$, (c) $\omega_{om2}/\omega_T = 0.8$, and (d) $\omega_{om2}/\omega_T = 10$ for $\omega_{oe2}/\omega_{om2} = 2$. The dashed line corresponding to each domain represents the $\omega_{pe2}/\omega_{pm2}$ required from our assumption for $s = s_{min}$ 71
- Figure 4.5:** Quantum levitation in magneto-dielectric plate configurations. (a) The complete parametric domain for Casimir force reversal according to the sufficient condition in Equation 4.17. (b) The parametric domain represented by the optical constants described Lorentz oscillator model with $\omega_{pm2}/\omega_{om2} = 0.5$. In all cases, we have set plate 1's permittivity as $\epsilon_1 = 2$ 74

- Figure 4.6:** A comparison between the repulsive Casimir force domains calculated based on the sufficient condition of Equation 4.17 (blue domain) and through exact numerical integration of Equation 2.20 (dots). In the calculations we vary the compound parameters and have fixed (a) $\omega_{pe2}/\omega_{pm2} = 0.9$ and $\omega_{pm2}/\omega_{om2} = 0.5$, and (b) $\omega_{om2}/\omega_T = 0.5$ and $\omega_{pe2}/\omega_{pm2} = 0.1$. In all cases, we have set plate 1's permittivity as $\epsilon_1 = 2$ 75
- Figure 5.1:** Parametric plot depicting the necessary condition in Equation 5.1 satisfied for different mode numbers as categorized based on the critical mode number n_c 80
- Figure 5.2:** Parametric domains corresponding to the cases where the bounds in Equation 5.2 are not satisfied (red) and $Li_0[R_p^n(q)e^{-ns/q}] < 0$ (blue). (a) TM and (b) TE polarizations are studied separately and in the calculation we use $\epsilon_1 = 2$ 83
- Figure 5.3:** Casimir force calculated numerically based on Equation 2.35 (solid lines), the upper bound Equation 5.3 (dotted lines), and the approximated result Equation 5.5 (dotted lines). In the calculations we use $\omega_{pe,1} = 0.5\omega_{oe,1}$ for the nonmagnetic plate 1 while the optical parameters of the plate 2 are set as (a) $\omega_{om,2} = 4\omega_T$ and (b) $\omega_{om,2} = 1.01\omega_T$ with $\omega_{om,2} = 0.6\omega_{oe,2}$, $\omega_{pm,2} = \omega_{om,2}$ and $\omega_{pe,2} = 0.5\omega_{pm,2}$ 85
- Figure 5.4:** Casimir force calculated based on Equation 2.35 (solid lines), the upper bound of the Casimir force in Equation 5.3 (dotted lines) and the approximation of Equation 5.5 (dotted lines). In the calculations we use $\omega_{pe,1} = 0.5\omega_{oe,1}$ for the nonmagnetic plate 1 while the optical parameters of plate 2 are set as (a) $\omega_{om,2} = 1.5\omega_T$ and (b) $\omega_{om,2} = 1.01\omega_T$ with $\omega_{oe,2} = 0.55\omega_{om,2}$, $\omega_{om,2} = 2.2\omega_{pm,2}$, and $\omega_{pe,2} = 1.1\omega_{pm,2}$ 86
- Figure 5.5:** Parametric domain depicting the sufficient condition for Casimir force repulsion. 88

- Figure 5.6:** Parametric domains corresponding to various conditions for realization of quantum levitation. The yellow domain corresponds to the sufficient condition given by Equation 5.8, red domain corresponds to the case where the necessary condition is satisfied for all modes $n \geq 1$, the blue domain corresponds to the case where the necessary condition is satisfied for modes less than the critical ($1 \leq n \leq n_c$) and the green domain corresponds to the case where the necessary condition is satisfied for modes greater than the critical ($n > n_c \geq 1$). The white dots represents the actual limit obtained through direct numerical calculations of the Casimir force using Equation 2.35 (the area below the dotted line). 89
- Figure 6.1:** Illustration of a composite medium consisting of a host medium with ϵ_1 and μ_1 and inclusions with ϵ_2 and μ_2 92
- Figure 6.2:** Illustration of the split ring resonator with the polarization and propagation direction of the incident electromagnetic wave indicated. 96
- Figure 6.3:** Plot of real part of the current I_1 (dashed blue) and I_2 (solid red) for $a = 20 \mu\text{m}$, $w = 1 \mu\text{m}$, $h = 1 \mu\text{m}$, $2\varphi_0 = 5^\circ$, $\lambda = 100a$, and $B_0 = 1$. The material considered for the SRR is gold with plasma frequency $\omega_p = 1.396 \cdot 10^{16}$ rad/sec and relaxation frequency $\gamma = 3.25 \cdot 10^{13}$ rad/sec. 103
- Figure 6.4:** Plot of internal resistance (solid blue, Equation 6.7), exact radiation resistance (solid green, Equation 6.33), analytical radiation resistance (dashed red, Equation 6.34) and total resistance $R_{\text{rad}} + R_{\text{in}}$ (black dashed) for $a = 20 \mu\text{m}$, $w = 1 \mu\text{m}$, $h = 1 \mu\text{m}$, (a) $2\varphi_0 = 2^\circ$, and (b) $2\varphi_0 = 0.02^\circ$ 106
- Figure 6.5:** Percentage relative error between the actual radiation resistance (Equation 6.33) and the approximated radiation resistance (Equation 6.34) with $a = 20 \mu\text{m}$ and $2\varphi_0 = 2^\circ$ for different ka and w/a ratio. 107
- Figure 6.6:** Percentage relative error between the actual radiation resistance (Equation 6.33) and the approximated radiation resistance (Equation 6.34) with $a = 20 \mu\text{m}$ for different ka and $2\varphi_0$ 108
- Figure 6.7:** The analytical model of the permeability μ'_{SRR} (solid blue, Equation 6.36), μ''_{SRR} (solid red, Equation 6.41), and μ''_{SRR} (dashed black, Equation 6.37). Plotted for $\omega_{\tau 0} = 0.5$, $\alpha = 0.01$, $\omega_0 = 5\text{eV}$, and $p = 0.4$ 111
- Figure 6.8:** Permeability of the SRR for $a = 1 \mu\text{m}$, $2\varphi_0 = 2^\circ$ and (a) $w = h = 0.1a$, (b) $w = h = 0.2a$, and (c) $w = h = 0.3a$. The solid black line denoted by $n = 1$ represents the frequency corresponding to the first vacuum mode $k_{\tau}a = 2\pi a/\lambda_{\tau}$ 113

- Figure 6.9:** Maximum radius of the SRR a (red dots) allowable in the limit of $ka \leq 1$ 114
- Figure 6.10:** Nickel polystyrene nanocomposites with air as a host medium..... 115
- Figure 6.11:** Effective permittivity ϵ_d (dashed red) and effective permeability μ_d (solid blue) of the nickel polystyrene nanocomposites. The solid black lines denotes the first, second, and third Matsubara frequencies..... 116
- Figure 6.12:** (a) Illustration of the nanowire composite media. (b) The composite is made of nano-wire pairs where w and a are the diameter and length of the wire, respectively, d is the separation distance between the wires. 117
- Figure 6.13:** The permittivity and the permeability of the wire media showing diamagnetic properties at high frequencies. The solid black lines denotes the first, second, and third Matsubara frequencies. 119
- Figure 7.1:** Permittivity and permeability of a magneto-dielectric material with equal magnetic and electric resonance frequencies. The dashed red line, blue, and black solid lines corresponds to the permittivity, and the permeabilities with $\omega_{pm}/\omega_{pe} = 1.2$, and $\omega_{pm}/\omega_{pe} = 0.8$, respectively. We have also fixed the resonant frequencies $\omega_{0e} = \omega_{0m} = 1.5 \cdot 10^{15}$ rad/sec, the plasma frequency $\omega_{pe} = 1.5\omega_{0e}$ and the relaxation frequencies $\gamma_e = \gamma_m = 0.1\omega_{0e}$. The first few Matsubara frequencies are included with gray vertical lines. 123
- Figure 7.2:** Permittivity and permeability of a magneto-dielectric material with highly mismatched resonance frequencies plotted for (a) real and (b) imaginary frequencies with the parameters of the Lorentz model used in the plots are as follow: $\omega_{0e} = 1.5 \cdot 10^{15}$ rad/sec, $\omega_{pe} = 1.5\omega_{0e}$, $\omega_{0m} = 0.3\omega_{0e}$, $\omega_{pm} = 0.5\omega_{pe}$, and $\gamma_e = \gamma_m = 0.1\omega_{0e}$ 125
- Figure 7.3:** Parallel-plate system with one plate made of polystyrene ferromagnetic nanocomposites and the other being a pure dielectric plate. 126
- Figure 7.4:** Parametric domain satisfying the necessary condition for repulsive Casimir force. In the calculations, we have fixed the volume fractions of the constituents $f_1 = 0.2$ (nickel) and $f_2 = 0.1$ (polystyrene)..... 127
- Figure 7.5:** Casimir force for different nickel nanoparticle sizes a_{Ni} . (a) 60 nm, (b) 80 nm, and (c) 100 nm..... 128

- Figure 7.6:** Quantum levitation system with a paramagnetic plate (plate 1) made of polystyrene ferromagnetic nanocomposites and a diamagnetic plate (plate 2) made of parallel nanowires dispersed in a dielectric host. 129
- Figure 7.7:** Parametric domain for which the nanowire composite plate is diamagnetic..... 130
- Figure 7.8:** Casimir force for different length of the nanowire pairs (plate 2), (a) $a = 200$ nm, (b) $a = 400$ nm, and (c) $a = 600$ nm. The fixed size of nickel nanoparticles (plate 1) is fixed at $a_{Ni} = 20$ nm. 131
- Figure 7.9:** Casimir force for different nickel nanoparticle sizes (plate 1), (a) $a_{Ni} = 20$ nm, (b) $a_{Ni} = 40$ nm, and (c) $a_{Ni} = 80$ nm. The length and diameter of the nanowires (plate 2) are fixed as $a = 100$ nm and $w = 10$ nm, respectively, and separated by $d = 0.1a$ 132

ACKNOWLEDGMENTS

I would like to express my deepest gratitude to my academic advisor Dr. Dentcho A. Genov for his strong commitment, constant encouragement, support, and guidance which helped me in successfully completing my doctoral research work. He taught me the power of persistence and hard work in achieving goals. I would like to acknowledge and thank my advisory committee members Dr. Neven Simicevic, Dr. Sandra Zivanovic, Dr. Long Que, and Dr. John Shaw for their support and assistance.

I would like to extend my appreciation to my friend and colleague Pattabhiraju Mundru for valuable discussions, encouragement, and creating an interest to attend many technical conferences. I would also like to thank Mona Alsaleh, Shravan Rakesh, and Rajkumar Vinnakota for their support. I am indebted to Dr. Tom John and Dr. Bobby Mathew for their guidance.

Most of all, I would like to express my gratitude to my sister Rajakumari and brother-in-law Ramanan for their encouragement and continued support throughout my research. I would also like to thank my friends Sangeetha Krishnamurthy, Saravanan Periyakaruppan, and Rajivalochan Subramanian for their inspiration and assistance in helping me to succeed in my doctoral studies.

CHAPTER 1

INTRODUCTION

1.1 Casimir Force

Casimir force is a quantum force between two neutral objects separated by distances ranging from a few nanometers up to tens of micrometers. The force appears due to an imbalance in the total number of vacuum fluctuation modes in-between and on either side of the objects. The Casimir force was first predicted to exist between two particles by H. G. B. Casimir and D. Polder in 1947 [1].

According to the van der Waals theory, two neutral particles are attracted to each other (or repelled away) due to the interaction of the fluctuating dipole field that is inherent to any neutral particle [2–6]. The electromechanical charge fluctuations in the neutral particles can be induced by the quantum zero-point fluctuations in the energy. Generally, the corresponding interaction energy between the particles follows a power law $\sim 1/d^6$, where d is the separation distance between the objects. This is valid under the assumption that the separation distance is much larger than the size of the particle a and much smaller than the wavelength λ under consideration, which usually corresponds to the energy difference between the ground level and the first excited level states of the atomic constituents ($\lambda \gg d \gg a$). In this case, the dipole field interaction between multiple particles is not considered [1–5, 7].

However, when the separation distance is comparable to or greater than the wavelength ($d \geq \lambda$), the finite time the dipole field takes to travel from one particle to the other needs to be included in the calculation, and as a result, the interaction energy falls rapidly. This phenomenon is known as *retardation effect*. Hence, with further increase in the separation distance $d \gg \lambda$, the retardation effect becomes important and the interaction energy falls rapidly as $\sim 1/d^7$ (instead of $\sim 1/d^6$ as per van der Waals interaction). Casimir and Polder observed this effect for a first time for colloidal particles. Hence the Casimir force between particles is also called a *retarded van der Waals interaction* [1–3, 7].

Based on their observations, Casimir and Polder argued that the force is due to the vacuum fluctuation modes that are responsible for inducing charge fluctuations in the otherwise neutral atoms. The quantum fluctuating field can be viewed as an ensemble of virtual photons that are created by the emergence and consequent annihilation of virtual particles such as quarks, anti-quarks, and gluons in a short period of time of the order of the Planck's time ($t_p \sim 5.32 * 10^{-44} s$) [8]. In a later study, Casimir considered a system made of two parallel conducting plates [9]. Similar to the case of two neutral particles, he observed the above mentioned retardation effect between the plates, with the vacuum force falling rapidly as $1/d^4$ instead of $1/d^3$. Casimir provided a theory for this particular case assuming semi-infinite plates with thickness t much larger than the plate separation distance $d \ll t$ and the thermal equilibrium for the system.

The nature of the Casimir force, whether attractive or repulsive, mainly depends on the object's material constituents, separation distance, shape, and temperature. It is important to note that in the literature a number of interactions are commonly referred to

as the Casimir effect and to clarify the distinction between them, we define them as follows [3, 6, 7]:

1. Retarded van der Waals interaction: Interaction between atoms or molecules, with a separation distance much larger compared to the relevant wavelength.
2. Casimir-Polder interaction: Interaction between an atom and a surface of a bulk material, usually a semi-infinite plate.
3. Casimir interaction: Interaction between two neutral material bodies.

The Casimir force is a striking example of the second quantization of the zero-point field and can be better understood using quantum field theory (QFT). According to the QFT, the vacuum field may be envisioned as interconnected oscillators present at each and every point in space (first quantization of the vacuum field). The strength of the vacuum field relates to the amplitudes of the oscillations. According to the second quantization of harmonic oscillators, the energy is quantized. The energy quantization leads to a nonzero ground state energy $E = \hbar\omega/2$ of the harmonic oscillators, also called the vacuum state. In order to determine the total energy of all vacuum fluctuations in space, one needs to perform an infinite summation. Hence, the total energy of the vacuum field is ill defined (infinite) and cannot be measured directly without an obstruction (an object). It is only possible to measure the difference in the vacuum force between two or more objects. This is because, in the case of a single object, the vacuum energy on either side of the object is the same and hence the net force acting on the object is zero. The presence of conducting and/or dielectric entities splits the physical space into various domains with each domain having infinite, but different, expectation values of the zero-point energy. The difference

in the expectation values between the domains, however, can be finite and may result in the manifestation of a force between them, the Casimir force [1, 3, 7, 10, 11].

In 1948, Casimir and Polder proposed a simple theory that described the particle-particle interactions (retarded van der Waals interaction) and plate-particle interactions (Casimir-Polder interactions) [1]. Later in the same year, Casimir investigated the force between two uncharged parallel metal plates and provided a simple but elegant theory [9]. According to Casimir, the force is due to the impact of the object's material boundaries on the zero-point energy fluctuations existent ubiquitously in space. The force is created due to the imbalance in the availability of vacuum fluctuations in-between and on either side of the plates. When two parallel plates are placed in the vacuum and separated by a distance d , only vacuum fluctuation of certain modes with wavelength limited by $\lambda \leq 2d$ can exist in between the plates, whereas vacuum fluctuations of all energies (wavelengths) exist on either side of the plates [9].

To clearly understand the origin of the Casimir force, next we review the concept of vacuum fluctuation modes in between two plates (similar to the case of the electromagnetic wave in a parallel plate waveguide).

1.2 Vacuum Fluctuations

According to classical electrodynamics, when there are no sources (charge and current), the energy associated with the system is zero ($E = 0$). The situation, however, is rather different when considered from the quantum electrodynamics (QED) point of view. According to QED, the minimum or the so-called zero-point energy of an oscillator is $E = \hbar\omega/2$, where \hbar is the reduced Plank constant and ω is the angular frequency [12]. Thus,

the free space with no material boundary constraints is comprised of a continuum of vacuum fluctuations modes with all possible energies ($E \rightarrow 0$ to ∞).

The vacuum fluctuations can be considered as creation and subsequent annihilation of the virtual particles in an extremely short time in the range of the Planck time. This is a process that is a direct consequence of the Heisenberg uncertainty principle which states that

$$\Delta E \Delta t \geq \frac{\hbar}{2}, \quad \text{Eq. 1.1}$$

or the product between the uncertainty in the energy and the time can never be less than $\hbar/2$ [12].

Figure 1.1 provides a rough depiction of the vacuum fluctuations as being a compendium of modes having different energies and existing all over the space. According to the law of conservation of energy, energy is neither created nor destroyed and the total energy remains constant. Since the vacuum fluctuations are emergent in space, it may seem that their existence violates the conservation of energy. However, as the vacuum fluctuations are extremely short lived, all energy perturbations are within the constraint of the Heisenberg principle and therefore the conservation of energy is not violated in any observable manner.

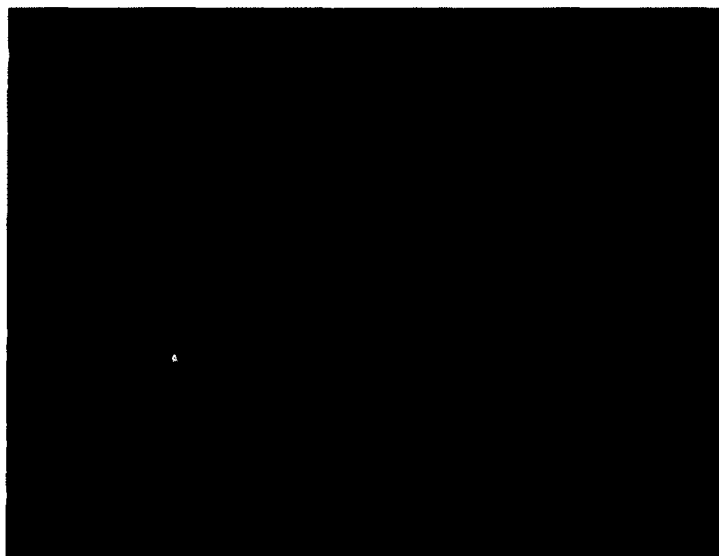


Figure 1.1: Illustration which exemplifies the fact that, in free space, fluctuating modes of virtually arbitrary energies (depicted with different colors) can be manifested simultaneously [13].

The vacuum field was an abstract idea before the discovery of the Casimir effect. Furthermore, apart from the Casimir effect, the vacuum fluctuations have other observable consequences that could be measured in experiments. For instance, the decay of an electron from excited energy level to ground state through spontaneous emission of a photon is due to the vacuum fluctuations. Without the notion of fluctuating fields and the Heisenberg uncertainty principle, the electron will remain in excited state for an infinitely long time. The process can thus be understood as being due to the perturbation introduced by the vacuum field on the electron at the excited state which leads to a transition to the ground state by radiation of a photon [14, 15].

In addition, the Lamb shift is one of the consequences of the vacuum field. The Lamb shift is the small energy difference between $2S_{1/2}$ and $2P_{1/2}$ orbitals of the hydrogen atom. According to Dirac, even though the energy levels of the $2S_{1/2}$ and $2P_{1/2}$ orbitals

are supposed to be the same, due to the interaction of electrons with vacuum fluctuations, there is a minor shift in the energy levels of the orbitals $2S_{1/2}$ and $2P_{1/2}$ [16].

1.3 Casimir Force Between Two Parallel Metal Plates

The Casimir effect occurs whenever a break of symmetry occurs in a given system. For example, when two parallel metal plates are placed in a vacuum and separated by a distance d , only vacuum fluctuations of certain modes with a maximum wavelength limited to $2d$ can exist in between the plates, whereas vacuum fluctuations of all energies exist on either side of the plates. The imbalance of the number of vacuum fluctuation modes in between and on either side of the plates is due to the boundaries of the plates [3, 5, 9, 11, 17].

As a result, the pressure due to the zero point fluctuation outside the plate will surpass that due to the fluctuating modes in between the plates. Concurrently, this radiation pressure imbalance pushes the two plates together and is manifested as a vacuum force. This force is generally attractive and mainly depends on the plate's optical properties, separation distance, and temperature. Figure 1.2 illustrates schematically the imbalance in the vacuum fluctuations modes when two parallel metal plates are placed in a vacuum. Similar to Figure 1.1, in Figure 1.2 the vacuum fluctuations of different frequencies are depicted as bubbles of different colors and sizes that correspond to different energies and wave vectors. The modes with low energies are depicted with red colors while the high energy modes are shown as blue.

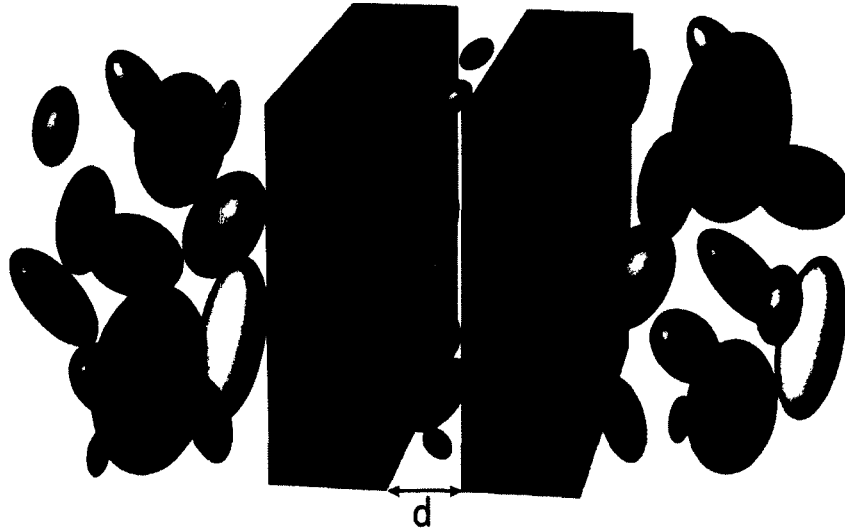


Figure 1.2: Parallel semi-infinite metal plates separated by a distance d with vacuum fluctuations in between and on either side of the plates.

The net force per unit area (vacuum pressure) was first derived by Casimir for two perfectly conducting plates at absolute zero and is given as [9],

$$F = \frac{\pi^2 \hbar c}{240d^4}. \quad \text{Eq. 1.2}$$

The Casimir pressure is inversely proportional to d^4 , which indicates that the force will decrease rather fast with the increase in the plates separation. For example, the Casimir pressure of $d = 1 \mu\text{m}$ is 1.3 mPa, which is much stronger compared to the Casimir pressure of $d = 10 \text{ nm}$ which is only 0.13 MPa.

The first successful experimental observation of the Casimir force was reported in 1958 by M. Sparnaay [18]. M. Sparnaay's results were in general agreement with the Casimir theory, but with large experimental errors mainly due to the difficulty in aligning the metallic mirrors as perfectly parallel to each other as possible. To eliminate alignment issues, thereafter, the experimental efforts have focused on using one flat plate and a second plate that is a segment of a sphere with a large radius of curvature. Using this new setup,

Steve K. Lamoreaux in 1997 [19], Umar Mohideen and A. Roy in 1998 [20], and A. Meurk *et al.* in 1997 [21] have reported experimental measurements with a much higher accuracy.

1.4 Implications Due to the Attractive Nature of the Casimir Force

One of the well-known implications due to the attractive nature of the Casimir force is the stiction effect in micro or nano devices such as comb drive, cantilevers, and other sensors and actuators that have components separated from each other in the range of a few micro/nano meters. The attractive Casimir force leads to decreased performances of nano devices due to increased friction between moving parts and may result in the sticking together of two or more components which is called as the “stiction effect”. The stiction effect hinders the proper functioning of the nano devices or in certain cases completely collapsing them [10, 22, 23].

In addition to the deleterious effects in microscopic devices, the attractive Casimir force can affect the state of macroscopic devices when they are close to each other. For instance, when two vessels are traveling parallel to each other in an ocean with strong tidal waves, they experience a force of attraction between them due to the difference in the availability of tidal-wave modes in between the vessels and on either side of the vessels. Thus, a classical Casimir force is generated that tends to pull the two vessels together with the ocean waves playing the role of the vacuum fluctuations [24].

The Casimir force plays a role in many natural phenomenon and can be even used by animals to get an evolutionary advantage. For instance, Geckos have a special type of feet that empowers them to stick to walls or glass surfaces effectively. The molecules in the outer part of the membrane of the Gecko’s foot facilitate a strong attractive force with

the walls or glasses. The Casimir force is not the only force that determines the sticking property of the Gecko's foot, but it is one of the main contributing forces [25].

1.5 Repulsive Casimir Force and Applications

Due to the implications that the attractive Casimir force has on nanodevices in the form of deleterious stiction effects, thus affecting their performances and proper functioning, it is desirable to find a way to nullify or reverse the force. Currently, there is a substantial impediment in a design of MEMS (micro electromechanical systems) or NEMS (nano electromechanical systems) devices or any other nano systems that have structures parallel to each other. For instance, in a case of a comb drive with parallel arms, the force on both sides of an arm needs to be balanced mechanically or electronically such that the air gap on either side of the arm is the same; otherwise, the arms will stick together and the whole system collapses [10, 22, 23]. So, it is highly important to balance the force to protect the integrity of the nanoscopic devices against the attractive Casimir force.

Hence, in this thesis, we investigate the possibility to reverse the Casimir force through the use of artificial electromagnetic material. Despite the many studies related to the reversal of the Casimir force [26–36], the conditions for force reversal in the case of air/vacuum as the intermediate medium are not well understood. Since air is the natural host medium for almost all MEMS/NEMS devices, the possibility of reversing the Casimir force can be of great practical importance.

The range of prospective applications of the Casimir force reversal or quantum levitation is rather broad. To list a few:

1. Highly accurate micro cantilevers to detect and measure extremely weak forces could be manufactured when the Casimir force of attraction is neutralized.

2. Quantum levitation devices allowing frictionless transportation of an object from one place to the other could be designed. For example, micro/nano channels for bio-fluid transportation: one can envision a viscous bio fluid levitating above a designed metamaterial plate with air as an intermediate medium. The fluid can possibly be made to flow over the metamaterial plate (channel) with no friction, thereby reducing corrosion or degradation of the plate.
3. Coating the surfaces of the experimental tables and equipment in a clean room with a metamaterial that repels dust particles, the incoming air flow will wash away the hanging dust particle resulting in a clean room with lower contamination and low maintenance costs.
4. Actuators and sensors based on the Casimir force could also be realized [23, 37, 38]. For example, an optical switch based on the attractive/repulsive Casimir force could be considered in the form of two parallel plates. If the force is repulsive and one of the plates is illuminated by an external laser beam, the electron concentration of that plate can rise and shift the plate's plasma frequency. If properly tuned this can change the polarity of the Casimir force from repulsive to attractive, collapsing the plates, and thus closing the switch mechanically.

1.6 Casimir Force Reversal Strategies

Recently, studies have shown that reversal of the Casimir force may be obtained at low temperature for a particular combination of materials, geometrical designs, and

distance between the plates. Currently, there are few known constraints for the Casimir force reversal that depends on the optical properties of the objects involved.

1.6.1 Dzyaloshinskii's Condition

As early as 1961, Dzyaloshinskii *et al.* showed that the Casimir force becomes repulsive if the permittivity of the intermediate medium is the intermediate value of the permittivity of the two plates ($\epsilon_{plate1} > \epsilon_{medium} > \epsilon_{plate2}$) [17]. However, satisfying the Dzyaloshinskii's condition is not possible with vacuum or air as the intermediate medium, except for materials with gain. This is because the permittivities of both plates estimated at the complex Matsubara frequencies are greater than unity for dissipative materials ($\epsilon_{plate1}, \epsilon_{plate2} \geq 1$) by assuming the Lorentz model for the permittivities. Though repulsion may be possible in the case of the active materials which usually requires an arrangement that changes the temperature of the plate like optical pumping [39] or quantum cascade lasing techniques [40], the Casimir or Lifshitz theory may not be applicable [41,42]. This is because the Casimir and Lifshitz theories are based on the fluctuation–dissipation theorem, which requires thermal equilibrium of the system. Recently, a few new theories have been proposed that considers systems that are not in thermal equilibrium and thus may be applicable for active materials [42]. However, these theories have not experimentally validated and will not be considered in this work.

1.6.2 Boyer's Condition

In 1974, Boyer proposed a different approach towards Casimir force reversal by considering a perfectly permeable plate ($\epsilon_{plate1} = 1$ and $\mu_{plate1} \rightarrow \infty$) and a perfectly conducting plate ($\epsilon_{plate2} \rightarrow \infty$ and $\mu_{plate2} = 1$) [43]. The magnitude of the repulsive force is determined to be 7/8 times the attractive force between two perfectly

conductive plates (see Equation 1.2). However, it is clear that Boyer's condition is highly unphysical and may not be achieved in practice. Recently, Kenneth *et al.* have investigated ways to relax the Boyer's condition mainly through the use of non-dispersive permeabilities [33]. They have proposed that the Casimir force will be reversed if one of the plates is purely magnetic ($\epsilon_{plate1} = 1$ and $\mu_{plate1} > 1$) while the other plate is purely dielectric ($\epsilon_{plate2} > 1$ and $\mu_{plate2} = 1$). However, this approach is also challenging to realize in practice, as it is not yet known how to achieve strong magnetic properties without a strong dielectric response.

1.6.3 Leonhardt and Philbin Condition

In 2007, Leonhardt and Philbin proposed a levitating system consisting of two dielectric/metal plates with a negative refractive index material in between them [44]. A material with magnetic permeability and electric permittivity that are simultaneously negative is called a negative index medium (NIM) [45]. The system consists of a base metal/dielectric plate with a thin metal sheet above it, with a NIM ($\epsilon = \mu = -1$) in between them. The NIM was shown mathematically to play the role of a parity inversion of Maxwell's equations that transforms the Cartesian $+x$ half-space into $-x$ half-space and vice versa. This process effectively results in the reversal of the Casimir force for all spatial frequencies. Metamaterial exhibiting negative index properties have been recently proposed as a mean to fabricate "perfect lenses" [46, 47]. However, as shown by Rosa *et al.*, this approach is also problematic due to the Drude nature of the metals that are used in the design [48]. In addition, the index of refraction has to be negative for a broad range of frequencies, as the Casimir force involves integration over all frequencies.

1.6.4 Proposed Systems with Repulsive Casimir Force

Apart from the theory, progress in the experimental validation of these concepts has been rather limited. In 2009, Munday *et al.* experimentally verified Dzyaloshinskii's condition using a silicon plate and a gold sphere with bromobenzene as the intermediate medium [49]. A maximum repulsive force of 100 pN was measured at room temperature, and the force decreased almost linearly at larger distances. Recently, another repulsive system, based on Dzyaloshinskii's condition, has been proposed with silicon dioxide as one of the plates and a high T_c superconductor (T_c – Curie temperature), bismuth strontium calcium copper oxide (BSCCO, $\text{Bi}_2\text{Sr}_2\text{CaCu}_2\text{O}_{8+\delta}$) as the other plate with bromobenzene as the intermediate medium [50].

Considering that air/vacuum is the natural medium for most of the NEMS/MEMS devices in which the Casimir force plays an important role, the need for achieving repulsion under such typical conditions remains imperative.

1.7 Related Research

Recent developments in the field of nanotechnology now permit manufacturing of devices with sizes in the range of a few nanometers. This advance in nano-manufacturing allows for the design of artificial materials with pre-set optical properties that may not be available in nature. Therefore, the field of electromagnetic metamaterials (EMMs) have recently gained a prominent role in optics and have been recognized as one of the most promising candidates for realizing Casimir force repulsion [28, 30, 35, 36, 44, 48, 51–53]. The EMMs are engineered materials that can provide unique optical properties such as magnetism at the infrared and optical frequency range [54], reversal of many optical phenomenon such as Doppler shift, Cherenkov's radiation and Snell's law [55], and

cloaking objects from EM waves [56–58] or matter waves [59]. The EMMs can be viewed as composite materials comprised of small metal-dielectric resonators that act as artificial “atoms” or “molecules” but with much larger magnetic and dipole moments, thus dramatically enhancing the range of optical properties of the naturally existing constituents. In what follows, we discuss some of the recent works that aim at achieving repulsive Casimir force using electromagnetic metamaterials.

In 2005, Henkel and Joulain provided a comprehensive theory for the Casimir force between dispersive magneto-dielectric plates for arbitrary temperatures. Most importantly, the authors showed that in principle it is possible to achieve a force reversal with air as the intermediate medium using metamaterials with strong magnetic response that are not commonly used in nano/micro devices. Few cases have been presented with a repulsive Casimir force achieved either with magnetic materials or multi-layered plates involving magnetic materials as thin films [28].

In 2008, I. G. Pirozhenko and A. Lambrecht studied the possibility of the Casimir force reversal using metamaterials for non-equal plate thicknesses [34]. As Dzyaloshinskii’s condition cannot be satisfied for a system with air as the intermediate medium, only Boyer’s condition is considered for achieving repulsion. Various configurations have been discussed including two nonmagnetic plates and the case of a purely magnetic plate and a purely dielectric plate for which the Casimir force is reversed as expected. The authors have shown that repulsion can be achieved in the case of a dielectric plate and a mainly magnetic metamaterial plate. The force is attractive for small plate separations and repulsive for intermediate and large plate separations.

In 2009, V. Yannopapas and N. V. Vitanov studied a configuration consisting of a metallic plate and a second plate made of various magnetic metamaterials [52]. The metamaterial plate modeled consisted of dielectric spheres made of Al_2O_3 infused with a paramagnetic Ni particles. The authors have shown that in principle this system can manifest quantum levitation for intermediate plate separation distances.

In 2010, L. Rosa and A. Lambrecht provided a sufficient condition for the Casimir force reversal in terms of the surface impedances of the two plates at zero temperature [36]. Even though the condition seems simple, involving only the surface impedances rather than the dielectric and magnetic material properties, the internal degrees of freedom of the plates including the temperature were not apparent.

From the previous works mentioned above, it is evident that a strongly magnetic plate is needed to achieve repulsive Casimir force. However, none of these works have provided an explicit sufficient condition for Casimir force reversal in general magneto-dielectric plate configurations. Hence, the main goal of this thesis is to provide a comprehensive study of Casimir force, mainly for the practically significant parallel-plate configuration. The goal is to provide an explicit formulation, in the form of necessary and sufficient conditions, for achieving quantum levitation in general dispersive magneto-dielectric systems. Such conditions will be highly useful for practically designing a quantum levitation system.

1.8 Dissertation Overview

The chapters in this dissertation are organized as follows. In Chapter 2, we provide the derivations of the Casimir force as proposed by Casimir and Lifshitz, separately. We provide the large and small separation distance asymptotic limits of the Casimir force and

introduce a modified Lifshitz theory that allows studies of dispersive magneto-dielectric plates. In Chapter 3, we consider an ideal system with non-dispersive plates. We show that there are in total six Casimir force types and have obtained a necessary condition for force reversal. In Chapter 4, we consider a system consisting of one dielectric plate with non-dispersive properties and a second magneto-dielectric plate that mimics nanoscale devices. We have identified the explicit parametric domain and the necessary and sufficient corresponding conditions for force reversal. In Chapter 5, we consider a general system with two dispersive plates and have identified the parametric domain and sufficient conditions for force reversal. In Chapter 6, we discuss in detail some prospective composite materials that can manifest strong magnetic response and thus may be used in the practical realization of a quantum levitating system. In Chapter 7, we discuss two specific designs that we have identified as the most promising candidates for repulsive Casimir force. Finally, in Chapter 8, we conclude and present future research directions.

CHAPTER 2

CASIMIR FORCE THEORY

2.1 Introduction

The first theory for the vacuum force between two objects has been formulated by Casimir in 1948. The Casimir theory is based on the idea of zero-point energies fluctuations and provides the force between two perfectly conducting metal plates at zero temperature [9]. In 1956, a comprehensive theory for the vacuum force was formulated by Lifshitz, who considered dielectric plates at non-zero temperature [2]. The Lifshitz theory is based on the fluctuation-dissipation theorem which states that a fluctuating field can be radiated from an atom/molecule due to vacuum induced dipole moments. Therefore, from the interacting fields in between the plates, the vacuum force is calculated [2]. Since Lifshitz method, several other methods have also been proposed to calculate the Casimir force between parallel plates [6, 7, 10, 17, 60, 61].

To better understand the origin of the Casimir force, we first consider the approaches provided by Casimir and Lifshitz, separately. We must point out that in both cases, the magnetic properties of the plates are not considered which, as we mentioned above, play a major role in the force reversal. Recently, Henkel and Joulain [28] have provided a generalization of the Lifshitz theory which includes the effects of magnetism. A discussion related to Henkel and Joulain theory is included in this chapter.

2.2 Casimir Theory - Force Between Two Uncharged Metallic Plates

Casimir described the origin of the attractive vacuum force between two conducting parallel half spaces separated by a distance d by considering the vacuum fluctuations as the source. The thickness t of the plates are assumed to be much larger than the plate separation distance $d \ll t$. The vacuum fluctuating modes are analogous to EM waves and the problem in hand is similar to EM waves in a parallel plate waveguide. The availability of the vacuum fluctuations in between the plates is limited due to the material boundaries of the plates. Hence, vacuum fluctuations of only certain modes (frequencies) can exist in between the plates, whereas vacuum fluctuations of all possible energies (frequencies) exist on either side of the plates. Casimir calculated the force between the plates by determining the energy associated with the vacuum modes in between and on either side of the plates at absolute zero and calculated the energy difference between them [9].

For perfectly conducting metal plates and low frequencies, the permittivity is very large [$\epsilon(\omega) \rightarrow -\infty$] which forces the tangential component of the electric field to be zero at the surface of the plates. This results in quantization of the z-component of the wave vectors of all modes in between the plates,

$$k_z = \frac{n \pi}{d}, \quad \text{Eq. 2.1}$$

where n is the mode number. The zero-point energy associated with each mode of frequency ω is $\hbar\omega(\vec{k})/2$ and the total energy of all fluctuating modes in between the plates is given by,

$$E(d) = 2 \sum'_{k_x, k_y, k_z} \frac{\hbar\omega_{k_x, k_y, k_z}}{2} = \hbar c \sum'_{k_x, k_y, n} \sqrt{k_x^2 + k_y^2 + \frac{n^2 \pi^2}{d^2}}, \quad \text{Eq. 2.2}$$

where k_x and k_y are the wave vectors in the x and y directions, respectively. A factor of 2 is added to account for the two polarizations [transverse electric (TE) and transverse magnetic (TM)] and the prime in the summation indicates that for $n = 0$ mode there is only one polarization mode and hence it has to be multiplied by 1/2. When the sides of the plates $L \gg d$, the k_x and k_y can be assumed to be continuous functions and could be summed over the corresponding integrals $\sum_{k_x} \rightarrow (L/\pi) \int_0^\infty dk_x$ and $\sum_{k_y} \rightarrow (L/\pi) \int_0^\infty dk_y$ in Equation 2.2. The total energy then follows as,

$$E(d) = \frac{\hbar c L^2}{\pi^2} \int_{k_x=0}^{\infty} \int_{k_y=0}^{\infty} \sum'_n \sqrt{k_x^2 + k_y^2 + \frac{n^2 \pi^2}{d^2}} dk_x dk_y. \quad \text{Eq. 2.3}$$

The vacuum fluctuations on either side of the plates are not quantized and hence the summation in Equation 2.3 is replaced by an integral along the wave vector k_z in the z direction. Therefore, the total energy in the fluctuating field on either side of the plates can be calculated as,

$$E(\infty) = \frac{d \hbar c L^2}{\pi^3} \int_{k_x=0}^{\infty} \int_{k_y=0}^{\infty} \int_{k_z=0}^{\infty} \sqrt{k_x^2 + k_y^2 + k_z^2} dk_x dk_y dk_z. \quad \text{Eq. 2.4}$$

The interaction energy then follows as,

$$U(d) = E(d) - E(\infty) \\ = \frac{\pi^2 \hbar c L^2}{4d^3} \left[\frac{1}{2} F(0) + \sum_{n=1}^{\infty} F(n) - \int_0^{\infty} F(\kappa) d\kappa \right], \quad \text{Eq. 2.5}$$

where $F(\kappa) = \int_0^\infty \sqrt{x + \kappa^2} f[\sqrt{x + \kappa^2} \pi/d] dx$, $x = k^2 d^2 / \pi^2$, $k = \sqrt{k_x^2 + k_y^2}$, and $\kappa = k_z d / \pi$. The cutoff function has the property that $f(k) \rightarrow 1$ for $k \ll k_m$ and $f(k) \rightarrow 0$ for $k \gg k_m$, where $ck_m \approx \omega_p$, the plasma frequency of the metal constituting the plates.

From Equations 2.3 and 2.4, it is clear that the energy of the vacuum fluctuation in-between and on either sides of the plates are infinite. However, the energy difference between two infinite values $E(d)$ and $E(\infty)$ can be finite as shown in Equation 2.5. The difference between two infinite integrals or sums can be calculated using one of the regularization methods such as Euler-Maclaurin summation formula or the zeta function regularization method. Here, we apply the Euler-Maclaurin summation formula in Equation 2.5 and obtain the difference as,

$$\begin{aligned} \sum_{n=1}^{\infty} F(n) - \int_0^{\infty} F(\kappa) d\kappa \\ = -\frac{1}{2}F(0) - \frac{1}{12}F'(0) + \frac{1}{720}F'''(0) + \dots \end{aligned} \quad \text{Eq. 2.6}$$

By considering the limits of $f(k)$, we determine that $F(\kappa) = -(2/3)\kappa^3 f[\kappa \pi/d]$. Then for $\kappa \rightarrow 0$, all the derivatives of $F(\kappa \rightarrow 0)$ in the series (Equation 2.6) goes to zero except $F'''(0) = -4$ and we obtain a simple form for the Casimir energy as,

$$U(d) = -\frac{\pi^2 \hbar c}{720 d^3} L^2. \quad \text{Eq. 2.7}$$

Finally, the Casimir force per unit area between two uncharged metal plates is obtained as,

$$F(d) = -\frac{dU(d)}{dd} = -\frac{\pi^2 \hbar c}{240 d^4}. \quad \text{Eq. 2.8}$$

From Equation 2.8 the Casimir force depends only on the separation distance between the plates d . The force decreases as a power law $1/d^4$ with the increase in the plates' separation distance and the negative sign implies that the force is attractive.

2.3 Lifshitz Formula - Force Between Two Uncharged Dielectric Plates

Lifshitz theory for calculating the Casimir force between parallel plates is based on Rytov's theory of charge and current fluctuations in a material body. When compared to Casimir theory, the Lifshitz theory is more general as it can be used to determine the force between dielectric plates as well as for arbitrary temperature. According to Rytov's theory, every atom or molecule has a fluctuating charge which creates a fluctuating electromagnetic field that radiates in all directions away from the source [62]. When we apply this theory to a bulk material, for instance a plate, the fluctuating electromagnetic field radiates from all sides of the plate. Lifshitz proposed his theory based on this assumption and the force between two parallel plates is created due to the interaction of the radiating fields in the region between the plates [2]. The magnitude and attractive or repulsive nature of the force mainly depends on the material of the plates, the medium between the plates, plate separation distance, and temperature.

In the calculation of the Casimir force, the fluctuating field acts as the source which is used in Maxwell's equations to obtain the associated electric and magnetic fields by applying the boundary conditions due to the material/object's body surfaces. Approaching the problem macroscopically, the interaction force between two objects is determined considering the fluctuating electromagnetic field. The fluctuating electromagnetic field is always present inside the absorbing medium and also extends outside its boundaries, partially as travelling waves and partially as standing waves, that decays (damped) exponentially as it propagates away from the surface of the material. It is important to note that this fluctuating electromagnetic field does not vanish at absolute zero, at which it is related to the zero-point vibrations (lowest possible energy) of the charges which is $\hbar\omega/2$.

Unlike the Casimir theory, the Lifshitz theory provides the change in the interaction energy due to retardation effects at large plate separations. Casimir energy is the difference between the energy associated with the field in between and on either side of the plates [2].

Here, we present the derivation of the Lifshitz formula using the method which has been developed and reformulated recently [7, 63–67]. For the calculation, a purely dielectric parallel-plates system is considered and the fluctuating field due to the dielectric material acts as a source. We consider the simplest configuration of two parallel semi-infinite plates separated by a vacuum gap of width d and the boundaries of the plates are at $z = \pm d/2$ (see Figure 2.1).

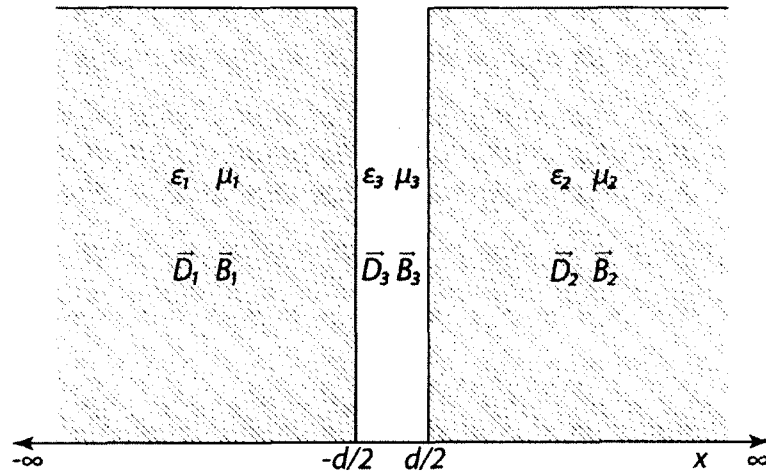


Figure 2.1: Semi-infinite parallel plates separated by a distance d .

For non-magnetic materials in the absence of charge and current densities, Maxwell's equations are given as,

$$\begin{aligned} \nabla \cdot \vec{D}(t, \vec{r}) &= 0, & \nabla \times \vec{E}(t, \vec{r}) + \frac{\partial \vec{B}(t, \vec{r})}{\partial t} &= 0, \\ \nabla \cdot \vec{B}(t, \vec{r}) &= 0, & \nabla \times \vec{H}(t, \vec{r}) - \frac{\partial \vec{D}(t, \vec{r})}{\partial t} &= 0. \end{aligned}$$

Eq. 2.9

where $\vec{D}(t, \vec{r})$ is the electric displacement, $\vec{E}(t, \vec{r})$ is the electric field, and $\vec{B}(t, \vec{r})$ is the magnetic field. Switching the time domain to the frequency domain we write,

$$\begin{aligned}\vec{E}(t, \vec{r}) &= \vec{E}(\vec{r})e^{-i\omega t}, \\ \vec{B}(t, \vec{r}) &= \vec{B}(\vec{r})e^{-i\omega t}.\end{aligned}\tag{Eq. 2.10}$$

Using the constituent relationship $\vec{D} = \epsilon_0 \epsilon(\omega) \vec{E}$ Maxwell's equations (Equation 2.9) can be written in the form of the wave equations,

$$\begin{aligned}\nabla^2 \vec{E}(t, \vec{r}) + \epsilon(\omega) \frac{\omega^2}{c^2} \vec{E}(t, \vec{r}) &= 0, \\ \nabla^2 \vec{B}(t, \vec{r}) + \epsilon(\omega) \frac{\omega^2}{c^2} \vec{B}(t, \vec{r}) &= 0.\end{aligned}\tag{Eq. 2.11}$$

For the region between the plates, the solutions of Equation 2.11 can be written in the form,

$$\begin{aligned}\vec{E}_J(\vec{r}) &= \vec{E}_{0,p}(z, k_{\perp})e^{i\vec{k}_{\perp} \cdot \vec{r}}, \\ \vec{B}_J(\vec{r}) &= \vec{B}_{0,p}(z, k_{\perp})e^{i\vec{k}_{\perp} \cdot \vec{r}},\end{aligned}\tag{Eq. 2.12}$$

where $\vec{r} = (x, y, z) = (r_{\perp}, z)$, $k_{\perp} = (k_x, k_y)$, $J = \{p, k_{\perp}, \omega\}$ is a compound index, and $p = \{TM, TE\}$ represents the two polarizations of the field. On substituting the fields in Equation 2.12 back into Equation 2.11, we obtain the equations for $\vec{E}_{0,p}$ and $\vec{B}_{0,p}$ as,

$$\begin{aligned}\vec{E}_{0,p}'' - l^2 \vec{E}_{0,p} &= 0, \\ \vec{B}_{0,p}'' - l^2 \vec{B}_{0,p} &= 0,\end{aligned}\tag{Eq. 2.13}$$

where $l^2 = k_{\perp}^2 - \epsilon(\omega) \omega^2 / c^2$ and for the intermediate medium the wave vector is replaced with $l^2 \rightarrow k^2 = k_{\perp}^2 - \omega^2 / c^2$. Similarly, when applying the fields in Maxwell's equations involving divergence, we obtain the projections of the $\vec{E}_{0,p}$ and $\vec{B}_{0,p}$ on the x , y , and z axes as,

$$\begin{aligned}
E'_{0,p,z} + ik_x E_{0,p,x} + ik_y E_{0,p,y} &= 0, \\
B'_{0,p,z} + ik_x B_{0,p,x} + ik_y B_{0,p,y} &= 0.
\end{aligned}
\tag{Eq. 2.14}$$

To obtain the fields associated with each regime in the system, see Figure 2.1. The continuity boundary conditions need to be satisfied which are given as,

$$\begin{aligned}
E_{\alpha t}(t, \vec{r}) &= E_{2t}(t, \vec{r}), & D_{\alpha n}(t, \vec{r}) &= D_{2n}(t, \vec{r}), \\
B_{\alpha n}(t, \vec{r}) &= B_{2n}(t, \vec{r}), & B_{\alpha t}(t, \vec{r}) &= B_{2t}(t, \vec{r}).
\end{aligned}
\tag{Eq. 2.15}$$

Here, n and t refer to the normal and tangential components, respectively. The suffix 2 and $\alpha = (1, 3)$ refer to the intermediate region and the dielectric semi-infinite regimes, respectively.

First, we consider the electric field and electric displacement. From the first equation in Equation 2.14 and the first condition in Equation 2.15, it is clear that $E_{0,p,x}$, $E_{0,p,y}$, and $E'_{0,p,z}$ need to be continuous across the boundary planes $z = \pm d/2$. Similarly, from the first equation in Equation 2.14 and the second condition in Equation 2.15, $\epsilon(\omega)E_{0,p,z}$ needs to be continuous across the boundary planes. Most importantly, $E_{0,p,z} \neq 0$ only for TM mode and hence only TM is considered for the electric field. Therefore, we present the electric field components in the different regions as,

$$E_{0,TM,z}(z, k_{\perp}) = \begin{cases} Ae^{lz} & z < -d/2 \\ Be^{kz} + Ce^{-kz} & |z| < d/2 \\ De^{-lz} & z > d/2. \end{cases}
\tag{Eq. 2.16}$$

Then, by applying the boundary conditions (Equation 2.15) the continuity of $E'_{0,p,z}$ and $\epsilon(\omega)E_{0,p,z}$ at the boundaries provides the following system of equations,

$$\begin{aligned}
Ae^{-ld/2} &= Bke^{-kd/2} - Cke^{kd/2}, \\
-Dle^{-ld/2} &= Bke^{kd/2} - Cke^{-kd/2}, \\
A\epsilon e^{-ld/2} &= Be^{-kd/2} + Ce^{kd/2}, \\
D\epsilon e^{-ld/2} &= Be^{kd/2} + Ce^{-kd/2}.
\end{aligned}
\tag{Eq. 2.17}$$

The unknown coefficients of the electric fields A, B, C , and D in Equations 2.16 and 2.17 have a non-trivial solution when the determinant of the known coefficients is equal to zero [7, 68], or

$$\Delta^{TM}(\omega, k_{\perp}) \equiv e^{-ld}[(\epsilon k + l)^2 e^{kd} - (\epsilon k - l)^2 e^{-kd}] = 0. \tag{Eq. 2.18}$$

Similarly, by using the second set of equations in Equation 2.15 for the magnetic field, we find that the components $B_{0,p,x}$, $B_{0,p,y}$, and $B_{0,p,z}$ need to be continuous across the boundary planes. In the case of the magnetic field, $B_{0,p,z} \neq 0$ for the TE mode and hence only TE modes are considered here. Matching the boundary conditions at the interfaces, similar to the electric field, we obtain a non-trivial solution for the magnetic field only when the below dispersion condition is satisfied,

$$\Delta^{TE}(\omega, k_{\perp}) \equiv e^{-ld}[(k + l)^2 e^{kd} - (k - l)^2 e^{-kd}] = 0. \tag{Eq. 2.19}$$

The solution to the dispersion relationships in Equations 2.18 and 2.19 give the modes Eigen frequencies as a function of the wave vectors $\omega_{k_{\perp},n}^{TM}$ and $\omega_{k_{\perp},n}^{TE}$ where n is the mode number.

The vacuum energy of the fluctuating field in between the plates, at absolute zero, is given as,

$$E_0(d) = \frac{\hbar}{4\pi} \int_0^{\infty} k_{\perp} dk_{\perp} \sum_n (\omega_{k_{\perp},n}^{TM} + \omega_{k_{\perp},n}^{TE}) S, \tag{Eq. 2.20}$$

where S is the surface area of the plates. The summation in the Equation 2.20 can be determined using the argument principle. For that we consider a closed contour consisting of a semi-circle C_+ of infinite radius on the right half of the complex plane with its center at the origin, and the imaginary axis bypassed in a counterclockwise direction. Provided that Δ^{TM} and Δ^{TE} do not have poles inside the contour, we get

$$\sum_n \omega_{k_\perp, n}^{TM, TE} = \frac{1}{2\pi i} \left[\int_{i\infty}^{-i\infty} \omega d \ln \Delta^{TM, TE}(\omega, k_\perp) + \int_{C_+} \omega d \ln \Delta^{TM, TE}(\omega, k_\perp) \right]. \quad \text{Eq. 2.21}$$

The second integral in Equation 2.21 can be determined using the natural assumption that $\lim_{\omega \rightarrow \infty} \varepsilon(\omega) = 1$ and $\lim_{\omega \rightarrow \infty} d\varepsilon(\omega)/d\omega = 0$ for the dielectric permittivity and given as,

$$\int_{C_+} \omega d \ln \Delta^{TM, TE}(\omega, k_\perp) = 4 \int_{C_+} d\omega. \quad \text{Eq. 2.22}$$

The value of the contour in the above equation is infinite and does not depend on the plate separation distance d .

By substituting Equation 2.22 back into Equation 2.21, and replacing $\omega \rightarrow -i\omega$, we obtain

$$\sum_n \omega_{k_\perp, n}^{TM, TE} = \frac{1}{2\pi} \int_{\infty}^{-\infty} \omega d \ln \Delta^{TM, TE}(i\omega, k_\perp) + \frac{2}{\pi} \int_{C_+} d\omega. \quad \text{Eq. 2.23}$$

Again the total energy is infinite. However, the Casimir energy per unit area is finite and can be determined as:

$$U(d) = \frac{E_0(d)}{S} - \lim_{d \rightarrow \infty} \frac{E_0(d)}{S}. \quad \text{Eq. 2.24}$$

It is important to note that the contour integral along C_+ in Equation 2.23 will be cancelled when calculating the energy difference (Equation 2.24). The Casimir energy per unit area between semi-infinite dielectric plates is thus given as,

$$U(d) = \frac{\hbar}{8\pi^2} \int_0^\infty k_\perp dk_\perp \int_\infty^{-\infty} \omega d \left[\ln \frac{\Delta^{TM}(i\omega, k_\perp)}{\Delta_\infty^{TM}(i\omega, k_\perp)} + \ln \frac{\Delta^{TE}(i\omega, k_\perp)}{\Delta_\infty^{TE}(i\omega, k_\perp)} \right], \quad \text{Eq. 2.25}$$

where $\Delta_\infty^{TM}(i\omega, k_\perp) = (\varepsilon k + l)^2 e^{(k-l)d}$ and $\Delta_\infty^{TE}(i\omega, k_\perp) = (k + l)^2 e^{(k-l)d}$.

By performing the integration in Equation 2.25 using Equations 2.18 and 2.19, we arrive at the Lifshitz formula,

$$U(d) = \frac{\hbar}{4\pi^2} \int_0^\infty k_\perp dk_\perp \int_0^\infty d\omega \{ \ln[1 - r_{TM}^2(i\omega, k_\perp)e^{-2kd}] + \ln[1 - r_{TE}^2(i\omega, k_\perp)e^{-2kd}] \}. \quad \text{Eq. 2.26}$$

The Fresnel reflection coefficients for the TM and TE waves used in the above equation are given as,

$$r_{TM}(i\omega, k_\perp) = \frac{\varepsilon(i\omega)k(i\omega, k_\perp) - l(i\omega, k_\perp)}{\varepsilon(i\omega)k(i\omega, k_\perp) + l(i\omega, k_\perp)}, \quad \text{Eq. 2.27}$$

$$r_{TE}(i\omega, k_\perp) = \frac{k(i\omega, k_\perp) - l(i\omega, k_\perp)}{k(i\omega, k_\perp) + l(i\omega, k_\perp)}.$$

The Casimir pressure can be determined using $F(d) = -\partial U(d)/\partial d$ and is given as,

$$F(d) = -\frac{\hbar}{2\pi^2} \int_0^\infty k_\perp dk_\perp \int_0^\infty k d\omega \left\{ \frac{r_{TM}^2(i\omega, k_\perp)}{e^{2kd} - r_{TM}^2(i\omega, k_\perp)} + \frac{r_{TE}^2(i\omega, k_\perp)}{e^{2kd} - r_{TE}^2(i\omega, k_\perp)} \right\} \quad \text{Eq. 2.28}$$

For finite temperature, the mode frequencies take discrete Matsubara values $\omega \rightarrow \omega_n = 2\pi n k_B T / \hbar$, where n is the mode number. Thus the Casimir pressure at finite temperature can be obtained by replacing in integration of the frequencies by summation, $(\hbar/2\pi) \int_0^\infty d\omega \rightarrow k_B T \sum_{n=0}^{\prime\infty}$ [7] and the wave vectors are $k^2 = k_\perp^2 + \varepsilon(i\omega_n) \omega_n^2 / c^2$ and $l^2 = k_\perp^2 + \omega_n^2 / c^2$. Inserting in Equation 2.28, we arrive at the Lifshitz formula for the Casimir pressure at finite temperature,

$$F(d, T) = -\frac{k_B T}{\pi} \sum_{n=0}^{\prime\infty} \int_0^\infty l k_\perp dk_\perp \left\{ \frac{[r_{TM}^n(i\omega_n, k_\perp)]^2}{e^{2ld} - [r_{TM}^n(i\omega_n, k_\perp)]^2} + \frac{[r_{TE}^n(i\omega_n, k_\perp)]^2}{e^{2ld} - [r_{TE}^n(i\omega_n, k_\perp)]^2} \right\} \quad \text{Eq. 2.29}$$

Here, the Fresnel reflection coefficients are estimated at the corresponding Matsubara frequencies ω_n . The prime next to the summation indicates that the $n = 0$ term is to be weighted by a factor of 1/2 as only one polarization mode exists. By transforming the integration in Equation 2.29 in terms of k we can also write the Casimir pressure as,

$$F(d, T) = -\frac{k_B T}{\pi} \sum_{n=0}^{\prime\infty} \int_{\omega_n/c}^\infty k^2 dk \left\{ \frac{[r_{TM}^n(i\omega_n, k)]^2}{e^{2kd} - [r_{TM}^n(i\omega_n, k)]^2} + \frac{[r_{TE}^n(i\omega_n, k)]^2}{e^{2kd} - [r_{TE}^n(i\omega_n, k)]^2} \right\} \quad \text{Eq. 2.30}$$

If we consider the case of two different dielectric plates with permittivities $\varepsilon_1(i\omega_n)$ and $\varepsilon_2(i\omega_n)$ then we have $r_p^n(\varepsilon, i\omega_n) \rightarrow \sqrt{r_{p,1}^n(\varepsilon_1, i\omega_n)r_{p,2}^n(\varepsilon_2, i\omega_n)}$ where $r_{p,1}^n(\varepsilon_1, i\omega_n)$ and $r_{p,2}^n(\varepsilon_2, i\omega_n)$, are the reflection coefficients of plate 1 and plate 2, respectively.

Finally, the Casimir pressure between two parallel dielectric plates at arbitrary temperature T is given as [2, 28],

$$F = \frac{k_B T}{\pi} \sum_p \sum_{n=0}^{\infty} \int_{nk_T}^{\infty} \text{Li}_0[R_p^n(k)e^{-2kd}]k^2 dk, \quad \text{Eq. 2.31}$$

where $\text{Li}_0[a] = a/(1-a)$ is the zero order polylogarithmic function, $p = (TM, TE)$ is the polarization index, $\omega_T = 2\pi k_B T/\hbar$, and $k_T = \omega_T/c$ are the thermal frequency and thermal wave vector, respectively. For convenience, the sign of the Casimir pressure in Equation 2.30 is reversed such that the force is attractive when the signature is positive and vice versa. The integration in Equation 2.31 is performed over the transversal wave vector k . The specular functions $R_p^n = r_{p,1}^n r_{p,2}^n$ are given by the Fresnel reflection coefficients at the respective plate interfaces. The Fresnel reflection coefficients for the TM and TE modes are written as,

$$r_{TM,l}^n(k) = \frac{\varepsilon_l(i\omega_n)k - \sqrt{(\varepsilon_l(i\omega_n) - 1)n^2 k_T^2 + k^2}}{\varepsilon_l(i\omega_n)k + \sqrt{(\varepsilon_l(i\omega_n) - 1)n^2 k_T^2 + k^2}}, \quad \text{Eq. 2.32}$$

$$r_{TE,l}^n(k) = \frac{k - \sqrt{(\varepsilon_l(i\omega_n) - 1)n^2 k_T^2 + k^2}}{k + \sqrt{(\varepsilon_l(i\omega_n) - 1)n^2 k_T^2 + k^2}}, \quad \text{Eq. 2.33}$$

where $\omega_n = n\omega_T$ are the Matsubara frequencies. The signature of the Casimir force can be altered by changing the material and geometry of the plates, temperature, and the separation distance between them. The Casimir force, either attractive or repulsive, will become negligible or zero for large separation distances.

Although the Lifshitz theory can be used to calculate the Casimir force at arbitrary temperature and for dielectric materials, in its current form (Equations 2.31, 2.32, and 2.33), the theory cannot be used to investigate general magneto-dielectric materials. More importantly, if both plates are dielectric with permittivities given by the Lorentz oscillator model [16], then it follows that for dissipative plates we have $\epsilon_1(i\omega_n) > 1$ and $\epsilon_2(i\omega_n) > 1$. Hence, Dzyaloshinskii's condition [$\epsilon_1(i\omega_n) > \epsilon_3(i\omega_n) > \epsilon_2(i\omega_n)$] cannot be satisfied, with air as the intermediate medium. Therefore, to consider the possibility for Casimir force reversal it is necessary to modify the Lifshitz theory to include magnetic materials.

Recently, Henkel and Joulain provided such a modification of the Lifshitz theory which includes magnetism [28]. The main and only difference compared to the original theory is the modification of the Fresnel reflection coefficients; for the TM mode are now given as,

$$r_{TM,l}^n(k) = \frac{\epsilon_l(i\omega_n)k - \sqrt{[\epsilon_l(i\omega_n)\mu_l(i\omega_n) - 1] n^2 k_T^2 + k^2}}{\epsilon_l(i\omega_n)k + \sqrt{[\epsilon_l(i\omega_n)\mu_l(i\omega_n) - 1] n^2 k_T^2 + k^2}} \quad \text{Eq. 2.34}$$

The reflection coefficient for the transfer electric (TE) polarization is obtained by exchanging $\epsilon_l \leftrightarrow \mu_l$ in Equation 2.34. It is important to note that the role of magnetic properties has already been considered by Boyer in 1974 [43], who also proposed a condition for quantum levitation (see section 1.6.2), but no elaborate theory have been provided. In what follows we will extensively use the Lifshitz formula Equation 2.31 with the general reflection coefficients Equation 2.34 to study the effects of magnetism on the Casimir force.

Performing the integration in Equation 2.31 is not a straightforward task. To simplify the analysis, we adopt a new integration variable, the inverse wave vector $q = nk_T/k \in (0,1)$ and substituting it in Equation 2.31 we write,

$$F = F_{n=0} + \frac{k_B T}{8\pi d^3} \sum_p \sum_{n=1}^{\infty} (ns)^3 \int_0^1 \text{Li}_0[R_p^n(q) e^{-ns/q}] \frac{dq}{q^4}, \quad \text{Eq. 2.35}$$

where $s = 2k_T d = 4\pi d / \lambda_T$ is the normalized plates separation distance. The Fresnel reflection coefficients for the TM polarization in terms of the new integration variable q are given as,

$$r_{TM,l}^n(q) = \frac{\varepsilon_l(i\omega_n) - \sqrt{(\varepsilon_l(i\omega_n)\mu_l(i\omega_n) - 1)q^2 + 1}}{\varepsilon_l(i\omega_n) + \sqrt{(\varepsilon_l(i\omega_n)\mu_l(i\omega_n) - 1)q^2 + 1}} \quad \text{Eq. 2.36}$$

For the TE waves the reflection coefficients are obtained again by interchanging $\varepsilon_l \leftrightarrow \mu_l$.

The force due to $n = 0$ mode is obtained by direct integration of Equation 2.31 and it can be written in close form as,

$$F_{n=0} = \frac{k_B T}{8\pi d^3} \sum_p \text{Li}_3[R_p^0(0)], \quad \text{Eq. 2.37}$$

where $R_p^0(0)$ are the static values of the specular functions. We have parted the $n = 0$ term in Equation 2.35. This particular rendering of the force allows us to infer the sign and zeroes of each term through the frequency dependence of the reflection coefficients Equation 2.34, which are now partially decoupled from the mode indexes and depends only on the dispersive properties of the plates (see Equation 2.36). By adopting this new integration variable for the integral, we obtain the finite limit for the integral $q \in (0,1)$, which is comparatively easier to analyze the nature of the force for different cases and investigate for the Casimir force reversal condition.

2.4 Casimir Force at Large Plate Separations

Before we study the material properties required for repulsive Casimir force, we find it useful to first investigate the asymptotic limits at large and small plate separation

distances. In the limit of large plate separations or high temperatures or both, $d/\lambda_T \gg 1$ or $s \gg 1$ where $\lambda_T = 2\pi c/\omega_T$ is the thermal wavelength. By applying the limit $s \gg 1$ in Equation 2.35, the polylogarithmic function approximates to $\text{Li}_0[R_p^n(q)e^{-ns/q}] \rightarrow R_p^n(q)e^{-ns/q}$ as $e^{-ns/q} \ll 1$. Hence, the force can be written as,

$$F = F_{n=0} + \frac{k_B T}{8\pi d^3} \sum_p \sum_{n=1}^{\infty} (ns)^3 \int_0^1 \frac{R_p^n(q)e^{-ns/q}}{q^4} dq. \quad \text{Eq. 2.38}$$

Furthermore, the term $(ns)^3 e^{-ns/q}$ in Equation 2.38 falls exponentially with an increase in mode number and normalized plate separation distance s . Hence, for $s \gg 1$, the force due to the higher order terms $n \geq 1$ is negligible compared to the force due to the zero order vacuum mode ($n = 0$). Therefore, the vacuum force at the large plate separations is accurately described using the zero frequency ($n = 0$) term, $F_{\infty} = F_{n=0}$ [28, 33]. The specular functions $R_p^0(0)$ then takes static values (in Equation 2.34) which are given as,

$$R_{TM}^0(0) = \left[\frac{\varepsilon_1(0) - 1}{\varepsilon_1(0) + 1} \right] \left[\frac{\varepsilon_2(0) - 1}{\varepsilon_2(0) + 1} \right], \quad \text{Eq. 2.39}$$

$$R_{TE}^0(0) = \left[\frac{\mu_1(0) - 1}{\mu_1(0) + 1} \right] \left[\frac{\mu_2(0) - 1}{\mu_2(0) + 1} \right]. \quad \text{Eq. 2.40}$$

Clearly, if a plate is non-magnetic, we have $R_{TE}^0(0) = 0$, and similarly, when a plate is purely magnetic then $R_{TM}^0(0) = 0$.

The asymptotic result shows us that to achieve quantum levitation at large separation distances or high temperatures or both, one or both of the specular functions must be negative. This may be achieved if $\varepsilon_1(0) < 1$ and $\varepsilon_2(0) > 0$ and/or one of the plates is diamagnetic and the other is paramagnetic in the static limit [43]. However, there

may be practical difficulties in realizing such materials, which will be discussed in Chapters 6 and 7.

2.5 Casimir Force at Small Plate Separations

Similar to the previous case, the Casimir force for small plate separations, low temperatures or both where $d/\lambda_T \ll 1$ or $s \ll 1$ could be obtained in closed form. For this we expand the polylogarithmic function in Equation 2.35 which now reads,

$$F = F_\infty + \frac{k_B T}{8\pi d^3} \sum_p \sum_{n=1}^{\infty} \sum_{m=1}^{\infty} (ns)^3 \int_0^1 \left[\frac{R_p^n(q)}{e^{ns/q}} \right]^m \frac{dq}{q^4}. \quad \text{Eq. 2.41}$$

In the limit $s \rightarrow 0$ we can use,

$$\lim_{\Delta \rightarrow 0} \left[\frac{e^{-4\Delta/q}}{q^4} \right] = \frac{1}{32\Delta^3} \delta_{[0,1]}(q - \Delta), \quad \text{Eq. 2.42}$$

where $\Delta = nms/4 \rightarrow 0$ and $\delta_{[0,1]}$ is the modified Dirac delta function defined in the unit interval such that $\int_0^1 f(q) \delta_{[0,1]}(q - a) dq = f(a)$ and $\int_0^1 \delta_{[0,1]}(q - a) dq = 1$. The integral in Equation 2.41 can now be estimated as,

$$\begin{aligned} (ns)^3 \int_0^1 \left[\frac{R_p^n(q)}{e^{ns/q}} \right]^m \frac{dq}{q^4} &\rightarrow (ns)^3 \lim_{\Delta \rightarrow 0} \left[\frac{1}{32\Delta^3} [R_p^n(\Delta)]^m \right] \\ &= \frac{2}{m^3} [R_p^n(0)]^m. \end{aligned} \quad \text{Eq. 2.43}$$

Finally, substituting in Equation 2.41, and performing the summation with respect to m , we obtain,

$$F_0 = \frac{k_B T}{4\pi d^3} \sum_p \sum_{n=0}^{\infty} \text{Li}_3 [R_p^n(0)]. \quad \text{Eq. 2.44}$$

This result implies that at very small separation distances, it is the non-retarded specular functions $R_p^n(0)$ that define the signature and magnitude of the force:

$$R_{TM}^n(0) = \left[\frac{\varepsilon_1(i\omega_n) - 1}{\varepsilon_1(i\omega_n) + 1} \right] \left[\frac{\varepsilon_2(i\omega_n) - 1}{\varepsilon_2(i\omega_n) + 1} \right], \quad \text{Eq. 2.45}$$

$$R_{TE}^n(0) = \left[\frac{\mu_1(i\omega_n) - 1}{\mu_1(i\omega_n) + 1} \right] \left[\frac{\mu_2(i\omega_n) - 1}{\mu_2(i\omega_n) + 1} \right]. \quad \text{Eq. 2.46}$$

We must note that the result of Equation 2.44 has also been obtained by other authors using a different procedure than ours [28, 33]. The possibility of the force reversal at small plate separations will be discussed in detail for specific cases in Chapters 3, 4, and 5.

Therefore, in this section, we have provided the theoretical background of the Casimir force that includes the derivation of the Casimir force between parallel metal plates (Casimir theory) and between parallel dielectric plates at an arbitrary temperature (Lifshitz theory). Finally, we also obtained the Casimir force at the asymptotic limits of large and small plate separations.

CHAPTER 3

CASIMIR FORCE BETWEEN TWO NONDISPERSIVE PARALLEL PLATES (IDEAL CASE)

3.1 Casimir Force for Parallel-Plate Configurations

We begin the analysis of the Casimir force by considering a simple case, a parallel-plate system with each plate having thickness t and are assumed to be made from non-dispersive materials. The plates are separated by a distance d and the system is at a temperature T . We will further simplify the analyses by considering the limiting case of $t \gg d$, or two semi-infinite plates. The Casimir force can be calculated using Equation 2.35. The Fresnel reflection coefficients for TM modes and for non-dispersive plates are given as,

$$r_{TM,l}(q) = \frac{\varepsilon_l - \sqrt{(\varepsilon_l \mu_l - 1)q^2 + 1}}{\varepsilon_l + \sqrt{(\varepsilon_l \mu_l - 1)q^2 + 1}}, \quad \text{Eq. 3.1}$$

where the permittivities ε_l and permeabilities μ_l of the plates are independent of the wave vector, and the frequency and the plate index takes the values $l = (1,2)$. The reflection coefficients for the TE waves are obtained from Equation 3.1 by exchanging $\varepsilon_l \leftrightarrow \mu_l$.

In the analysis that follows, we impose the practical limitation on the plates' permittivities and permeabilities which is that they must be positive [$\varepsilon_l, \mu_l \in (0, \infty)$]. The permittivity and permeability of real materials are usually described using one of the well-known analytical models: Lorentz, Drude, and Debye models. The Lorentz model is

generally used to describe the electromagnetic properties of dielectric materials. Similarly, the Drude model is used for metals, and the Debye model is used for stratified media. Estimated at the imaginary Matsubara frequencies, all three models give real and smooth (non-resonance) functions for ϵ_l , and μ_l (see Equation 2.36). In the case of the Lorentz and Drude models, the permittivities and permeabilities are always greater than one for the dissipative media. If gain is present, however, one can also have $\epsilon_l < 1$, and $\mu_l < 1$ within a finite frequency range. In the case of the Debye model, the permittivities and permeabilities are generally positive; however, they could become negative for a narrow frequency range. Considering the above limitations and the fact that the Casimir force includes contributions due to all modes (from $n = 0$ to ∞), we restrict our analysis by assuming positive values for both ϵ_l and μ_l .

3.2 Attractive and Repulsive Casimir Forces

First, to gain an understanding on the nature of the force for different plate separation distances, we plot in Figure 3.1 the Casimir force which was numerically calculated by using Equation 2.35 for two different configurations. The force can be repulsive (case 1) or attractive (case 2) for all separation distances. In the figure we have normalized the Casimir pressure so that it is constant at large separation distances. Furthermore, the thermal wavelength $\lambda_T = 2\pi c/\omega_T$ is introduced to provide a physically meaningful length scale. In the limit of small plate separations ($d \ll \lambda_T$), the force scales as $1/d^4$ and falls as $1/d^3$ at large plate separations ($d \gg \lambda_T$).

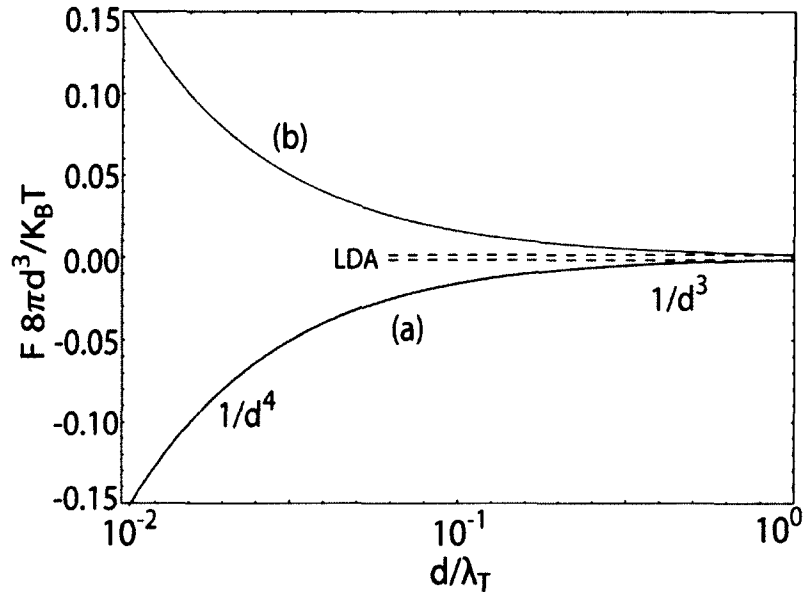


Figure 3.1: Casimir forces (solid lines) and large distance asymptotic (dashed lines) for two different configurations. (a): $\epsilon_1 = 2, \mu_1 = 1, \epsilon_2 = 0.5,$ and $\mu_2 = 1$ (blue) and (b): $\epsilon_1 = 2, \mu_1 = 1, \epsilon_2 = 2,$ and $\mu_2 = 1$ (red).

A simple analysis of Equation 2.35 shows that for large separation distances, $d \gg \lambda_T$, the large distance asymptotics (LDA), the value of the force $F_{LDA} = F_\infty$ depends only on the $n = 0$ mode and is indeed given by Equation 2.37 (dashed lines in Figure 3.1) [28, 33]. With a decrease in the separation distance an increasing number of modes (higher order modes) needs to be included in the summation in order to achieve convergence. This is evident by inspection of Equation 2.35, which shows that the integrands will become exponentially small only for $n > n_c = 1/s = \lambda_T/4\pi d$, or conversely all terms with $n < n_c$ will contribute substantially to the force and must be considered. Furthermore, since λ_T is inversely proportional to the temperature for a fixed separation distance, an increasing number of modes need to be included to achieve convergence with decreasing temperature. To summarize, a large number of modes needs to be included in the summation at low temperatures and/or small plate separations.

As shown in Figure 3.1, case (a) F_{LDA} is repulsive because it satisfies the Dzyaloshinskii's condition ($\epsilon_1 > 1 > \epsilon_2$), and case (b) F_{LDA} is attractive, as it does not satisfy any of the well-known repulsive conditions (see Section 1.6). In what follows we will show that the Casimir force may be repulsive even when the conventional (known) conditions for quantum levitations are not satisfied.

3.3 Repulsive Casimir Force Parametric Analysis

Here, we perform a parametric analyses aiming at identifying parallel-plate configurations showing quantum levitation that are not defined by the well-known conditions. For that, first we consider the vacuum force for large plate separations $s = 2k_T d \gg 1$, which is accurately described by Equation 2.37. By inspection it is clear that repulsion can be achieved provided,

$$\sum_p \text{Li}_3[R_p^0(0)] = \text{Li}_3 \left[\frac{(\epsilon_1 - 1)(\epsilon_2 - 1)}{(\epsilon_1 - 1)(\epsilon_2 - 1)} \right] + \text{Li}_3 \left[\frac{(\mu_1 - 1)(\mu_2 - 1)}{(\mu_1 - 1)(\mu_2 - 1)} \right] < 0. \quad \text{Eq. 3.2}$$

When Equation 3.2 is satisfied, the Casimir force is repulsive for large plate separations. Through parametric swipe, we can compare the repulsion condition due to Equation 3.2 with the Dzyaloshinskii's and Kenneth *et al.*'s conditions for different permittivities and permeabilities of the plates (see Figure 3.2).

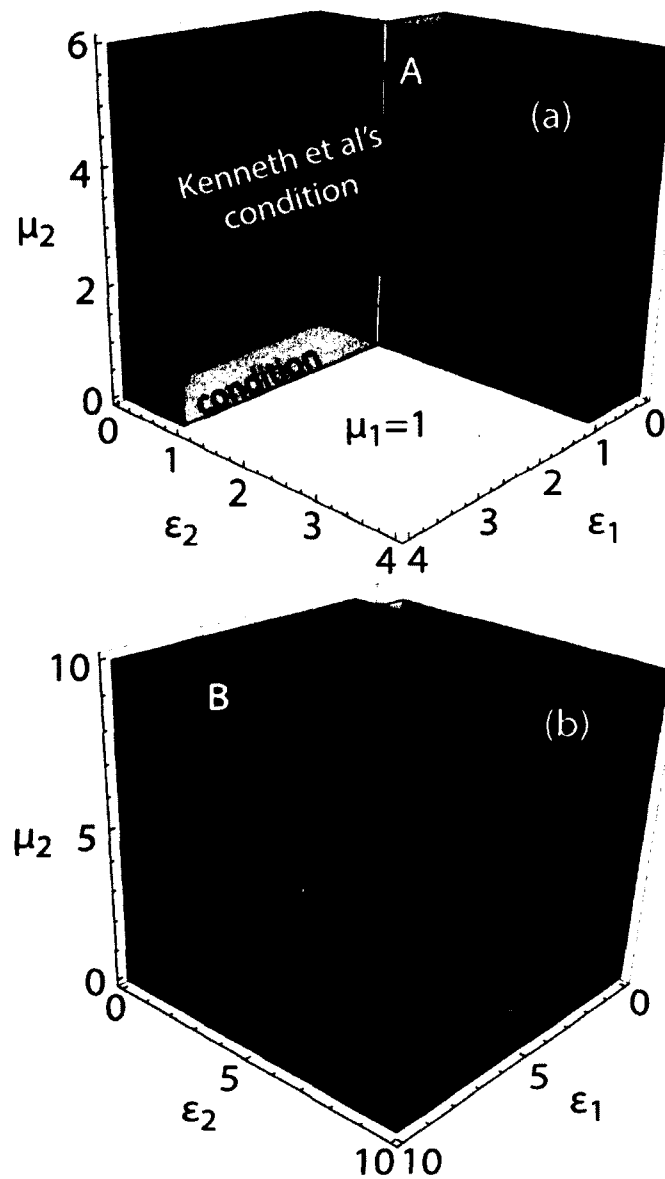


Figure 3.2: Repulsive Casimir force domains according to Dzyaloshinskii's (yellow domain) and Kenneth *et al.*'s (gray domain) conditions and the LDA condition in Equation 3.2 (red domain, $F_{LDA} < 0$) for fixed permeability of plate 1: (a) $\mu_1 = 1$ and (b) $\mu_1 = 2$. The point A correspond to the values $\epsilon_1 = 2$, $\epsilon_2 = 2$, and $\mu_2 = 6$ and similarly, the point B correspond to the values $\epsilon_1 = 10$, $\epsilon_2 = 2$, and $\mu_2 = 10$.

Figure 3.2 (a) shows the parametric domains for force reversal, assuming one of the plates is non-magnetic ($\mu_1 = 1$). In this case, the Dzyaloshinskii's condition coincided with the far field asymptotic condition Equation 3.2 while Kenneth *et al.*'s condition is a subset.

Although Boyer's condition also falls in the parametric space considered, it is not shown as it lies in a plane where the permeability of one of the plates and the permittivity of the other plate are infinitely large ($\epsilon_1 = 1, \mu_1 \rightarrow \infty, \epsilon_2 \rightarrow \infty$ and $\mu_2 = 1$). Leonhardt's condition is not applicable here, as it involves negative index medium (NIM) as a host, which is clearly different from the natural medium (air/vacuum) of the nano or micro devices.

Figure 3.2 (b) shows the parametric domain for $\mu_1 = 2$ in which case Kenneth *et al.*'s condition is not applicable and only Dzyaloshinskii's condition and the large distance asymptotic (LDA) condition of Equation 3.2 are studied. Clearly, the repulsion LDA condition is a subset of the Dzyaloshinskii's condition. This implies that if the Dzyaloshinskii's condition is satisfied, the force can be repulsive at small separations even if it is attractive at large separations.

More importantly, none of the conditions outlined above are necessary for force reversal. This is demonstrated in Figure 3.3 where we plot the force for two "random" points from the parametric spaces in Figures 3.2 (a) and (b), which do not satisfy the above conditions but show quantum levitation [the points are marked as A in Figure 3.2 (a) and B in Figure 3.2 (b)]. The Casimir forces for both cases are repulsive for small plate separations and attractive for large plate separations because they do not satisfy the large distance asymptotic (LDA) condition of Equation 3.2.

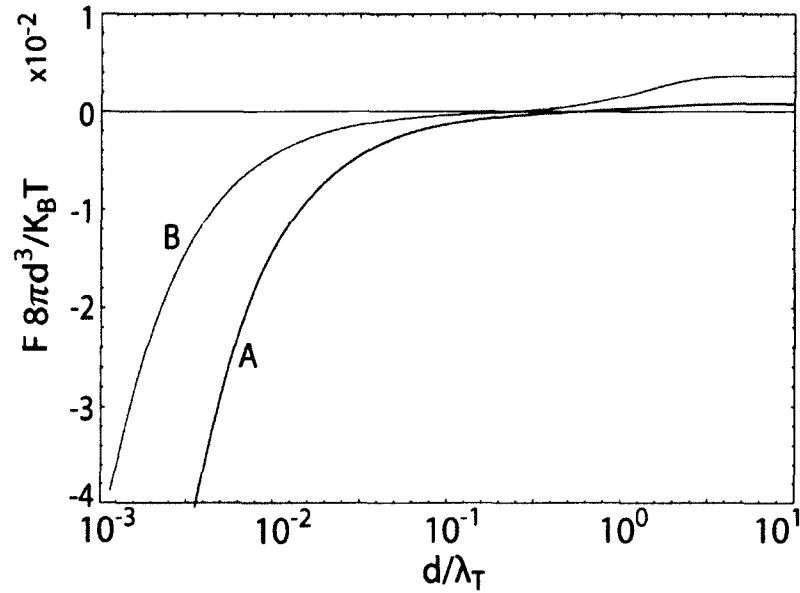


Figure 3.3: Casimir force for the two configurations chosen from the parametric space in Figures 3.2 (a) and (b). A: $\varepsilon_1 = 2$, $\mu_1 = 1$, $\varepsilon_2 = 2$, and $\mu_2 = 6$, and B: $\varepsilon_1 = 10$, $\mu_1 = 2$, $\varepsilon_2 = 2$, and $\mu_2 = 10$.

The two repulsive systems presented in Figure 3.3 clearly shows that quantum levitation can be achieved for a much broader range of parametric conditions far surpassing the much restrictive conditions due to Dzyaloshinskii and Kenneth *et al.* and the LDA repulsion condition in Equation 3.2. Therefore, we conclude that the LDA condition is a subset of Dzyaloshinskii's condition which in turn is a subset of a broader parametric domain showing quantum levitation. Hence, in the next section, our aim is to provide broader (all encompassing) necessary and sufficient conditions for quantum levitation.

3.4 General Conditions for Repulsive Casimir Force

In this subsection, we perform a detailed analyses aimed at finding the entire parametric domain for repulsive Casimir force. To perform this type of analysis, we work directly with Equation 2.35. If we expand the polylog function in series ($\text{Li}_0[a] = \sum_{m=1}^{\infty} a^m$) we can write,

$$F = F_\infty + \frac{k_B T}{8\pi d^3} \sum_p \sum_{n=1}^{\infty} (ns)^3 \sum_{m=1}^{\infty} \int_0^1 [R_p(q) e^{-ns/q}]^m \frac{dq}{q^4}. \quad \text{Eq. 3.3}$$

Introducing a new variable $\alpha = s/q$, we can also write,

$$F = F_\infty + \frac{k_B T}{8\pi d^3} \sum_p \sum_{n=1}^{\infty} n^3 \sum_{m=1}^{\infty} \int_0^1 \alpha^3 [R_p(q) e^{-n\alpha}]^m \frac{dq}{q}. \quad \text{Eq. 3.4}$$

The summation over the mode number n can be performed explicitly, thus resulting in,

$$F = F_\infty + \frac{k_B T}{8\pi d^3} \sum_p \sum_{m=1}^{\infty} \int_0^1 R_p^m(q) \frac{\alpha^3}{8} [2 + \cosh(m\alpha)] \text{csch}^4\left(\frac{m\alpha}{2}\right) \frac{dq}{q}. \quad \text{Eq. 3.5}$$

Introducing the function $C(m\alpha) = [(m\alpha)^4/48][2 + \cosh(m\alpha)]\text{csch}^4(m\alpha/2)$ we rewrite Equation 3.5 in a shorter format:

$$F = F_\infty + \frac{3k_B T}{4\pi d^3} \frac{1}{s} \sum_p \sum_{m=1}^{\infty} \int_0^1 \frac{C(m\alpha) R_p^m(q)}{m^4} dq. \quad \text{Eq. 3.6}$$

This new formulation of the Casimir force still involves the summation over m and integration over q and, in general, does not have an exact analytical solution. However, the summation is fast converging with the first term ($m = 1$), thus constituting the largest contribution to the total force (more than 80%). This is due to the fact that $\text{Li}_0[R_p(q) e^{-ns/q}] \approx R_p(q) e^{-ns/q} \ll 1$, a fact we used earlier to obtain the force at large separation distances. This also implies that, similar to the role of the mode number n at different separation distances, we may need to include a large number of m to describe as accurately the force for small separation distances.

We proceed by seeking simplified expressions for the force at critical regions with the goal of identifying various conditions for force repulsion. A simple analysis shows that the Casimir force is non-monotonic when repulsive, with a minimum at intermediate separation distances.

To perform an in-depth analysis for the repulsive conditions, first we need to understand better the dependence of the specular functions on the inverse wave vector. The specular functions for non-dispersive materials with $\epsilon_l \geq 0$ and $\mu_l \geq 0$ are confined within the strict limits with $R_p(1) \leq R_p(q) \leq R_p(0)$ and $-1 \leq R_p(q) \leq 1$, with single or no real roots. The specular functions at $q = 0$ and $q = 1$ take simple forms: $R_{TM}(0) = (\epsilon_1 - 1)(\epsilon_2 - 1)/[(\epsilon_1 + 1)(\epsilon_2 + 1)]$, $R_{TE}(0) = (\mu_1 - 1)(\mu_2 - 1)/[(\mu_1 + 1)(\mu_2 + 1)]$, and $R_{TM}(1) = R_{TE}(1) = [(z_1 - 1)(z_2 - 1)]/[(z_1 + 1)(z_2 + 1)]$, where $z_1 = \sqrt{\mu_1/\epsilon_1}$ and $z_2 = \sqrt{\mu_2/\epsilon_2}$ are the impedances of the first and second plates, respectively.

For large plate separations, the force is mainly described by the zero-order vacuum mode and $F(s \rightarrow \infty) = F_\infty$ [28, 33]. Hence, the force will be repulsive if the LDA condition of Equation 3.2 is satisfied (depending on $R_p(0) < 0$), irrespective of the value of $R_p(1)$. The LDA condition implies that the non-retarded specular functions need to be predominantly negative such that $F_\infty = \text{Li}_3[R_{TM}(0)] + \text{Li}_3[R_{TE}(0)] < 0$. We must note that this does not necessarily require simultaneous negative signature of the specular functions.

For small plate separation distances, we have $C(m\alpha) \rightarrow 1$ and the Casimir force $F \rightarrow F_0$, which is written as,

$$\frac{8\pi d^3 F_0}{k_B T} = \frac{6}{s} \sum_p \int_0^1 \text{Li}_4[R_p(q)] dq. \quad \text{Eq. 3.7}$$

Hence, in this case, the force depends on specular functions for the entire range of wave vectors ($0 \leq q \leq 1$) and F_∞ is negligible for $s \rightarrow 0$.

For intermediate separation distances ($s > 1$ or $m\alpha > 1$), the force in Equation 3.6 can be expanded in the power series about $e^{-m\alpha/2} \rightarrow 0$, and by considering only the first term in the series, we obtain

$$\frac{8\pi d^3 F_s}{k_B T} = \sum_p \text{Li}_3[R_p(0)] + s^3 \sum_{m=1}^{\infty} \int_0^1 \frac{R_p^m(q) e^{-ms/q}}{q^4} dq. \quad \text{Eq. 3.8}$$

For $ms > 1$, the weighted term in the integral (Equation 3.8) $e^{-ms/q}/q^4$ has a maxima for $q = ms/4$. Since $q \leq 1$, the expression Equation 3.8 can be further simplified by expanding $R_p^m(q)$ in the power series about $q \rightarrow 1$. Considering the first term in the series and after simple algebraic manipulation by including only the dominant terms, we obtain

$$\frac{8\pi d^3 F_s}{k_B T} = \sum_p \text{Li}_3[R_p(0)] + s^2 \text{Li}_1[e^{-s} R_p(1)]. \quad \text{Eq. 3.9}$$

The Casimir force for intermediate plate separations explicitly depends on both $R_p(0)$ and $R_p(1)$. It is apparent that the force is repulsive when both $R_p(0) < 0$ and $R_p(1) < 0$. However, this does not suggest that the force is repulsive only for intermediate plate separations; the force might be repulsive for large plate separation and/or small separation distances as well. For instance, when $R_p(0) > 0$ and $R_p(1) < 0$, the force may be repulsive for intermediate and small plate separations with attractive force at large separations.

From the analyses performed for small, intermediate, and large plate separations, we can categorize the Casimir force based on its attractive and repulsive nature at different separation distances. There are six different types based on the values of F_0 , F_∞ , $R_p(0)$, and $R_p(1)$ as shown below.

1. Type 1: The force is attractive for all plate separation distances when $F_0 > 0$, $F_\infty > 0$ [$R_p(0) > 0$], and $R_p(1) > 0$ (① in Figure 3.4).
2. Type 2: The force is repulsive for all plate separation distances when $F_0 < 0$, $F_\infty < 0$ [$R_p(0) < 0$], and $R_p(1) < 0$ (② in Figure 3.4).
3. Type 3: The force is attractive for small plate separations and repulsive for large plate separations when $F_0 > 0$ and $F_\infty < 0$ [$R_p(0) < 0$], irrespective of $R_p(1)$ (③ in Figure 3.4).
4. Type 4: The force is repulsive for small plate separations and attractive for large plate separations when $F_0 < 0$ and $F_\infty > 0$ [$R_p(0) > 0$], irrespective of $R_p(1)$ (④ in Figure 3.4).
5. Type 5: The force is attractive for small and large plate separations and may be repulsive for intermediate separations, which is termed as a *repulsive kink*, when $F_0 > 0$, $F_\infty > 0$ [$R_p(0) > 0$], and $R_p(1) < 0$ (⑤ in Figure 3.4).
6. Type 6: The force is repulsive for small and large plate separations and may be attractive for intermediate separations, which is termed as an *attractive kink*, when $F_0 < 0$, $F_\infty < 0$ [$R_p(0) < 0$], and $R_p(1) > 0$ (⑥ in Figure 3.4).

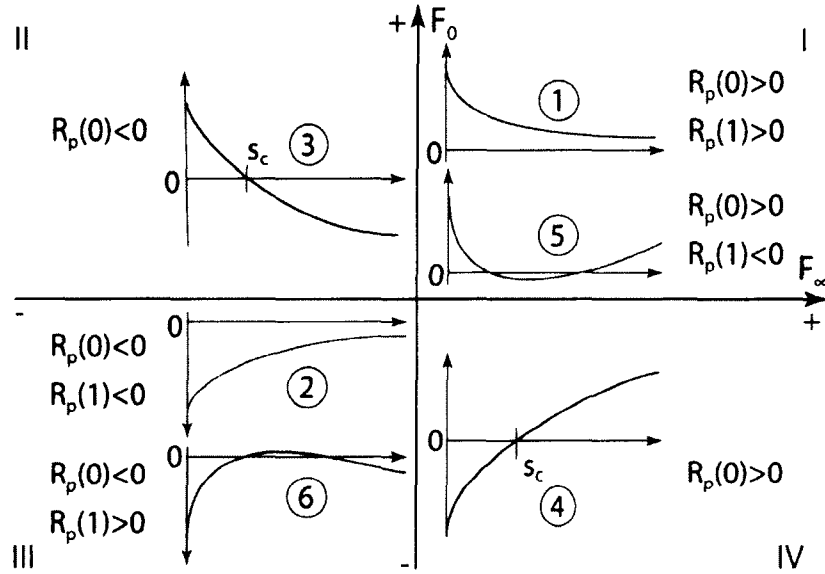


Figure 3.4: Force quadrants in terms of F_0 and F_∞ , showcasing the six universal types of the Casimir force.

Figure 3.4 presents all four quadrants with respect to the values of the Casimir force at large and small separation distances. The nature of the force according to the specifications from above is identified. Specifically, the first quadrant (I) includes type 1 and type 5, the second quadrant (II) includes type 3, the third quadrant (III) includes type 2 and type 6, and the fourth quadrant (IV) includes type 4. The cutoff distance $s = s_c$, that is related to type 3 and type 4, is the plate separation distance at which the force changes its signature. The conditions provided for types 1-4 (with respect to the specular functions) can be considered as sufficient conditions, whereas the conditions provided for types 5 and 6 are necessary but not sufficient. Therefore, in the following analysis, we seek a sufficient condition for the Casimir force of types 5 and 6.

We proceed by writing (Equation 3.6) in terms of a weighted function as,

$$F = F_\infty + \frac{k_B T}{8\pi d^3} \sum_p \sum_{m=1}^{\infty} \delta(s, m, 1) \int_0^1 W(s, m, q) R_p^m(q) dq, \quad \text{Eq. 3.10}$$

where the weight function is $W(s, m, q) = \delta(s, m, q)/\delta(s, m, q = 1)$ and $\delta(s, m, q) = 6C(m\alpha)/sm^4$. The introduction of the weight function allows us to understand the dependence of the integrant better and the selection of the dominant value of specular functions on various parameters including q .

Figure 3.5 shows the weight function $W(s, m, q)$ for different q , and summation index m [Figure 3.5 (a)], and the normalized separation distance s [Figure 3.5 (b)]. With an increase in s , the weight $W(s, m, q)$ to the specular functions shifts towards $q = 1$ [see Figure 3.5 (a), solid green], and with a decrease in s , the weight function broadens, thus covering a wide range of q and shifts towards $q = 0$ [see Figure 3.5 (a), solid blue]. Finally, for small separation distances, the specular functions are weighted equally for all q [see Figure 3.5 (a), solid red].

The weight function W for intermediate separation distance could be approximated as a Heaviside function with new limits for the integral in Equation 3.10 with $W(s, m, q) \rightarrow \theta(q - q_c)$, where q_c is the cutoff inverse wave vector, thereby reducing the complexity of the integral [see solid blue curve in Figure 3.5 (a)]. Similarly, with an increase in m , the weight shifts towards $q = 1$ for fixed s [see Figure 3.5 (a), solid, dotted, and dashed blue curves] and for $m \rightarrow \infty$, the specular functions at $q = 1$ is sufficient to determine the force. To summarize, the sign of the specular functions at $q \rightarrow 1$ are of great importance and mainly determines the nature of the force (attractive or repulsive).

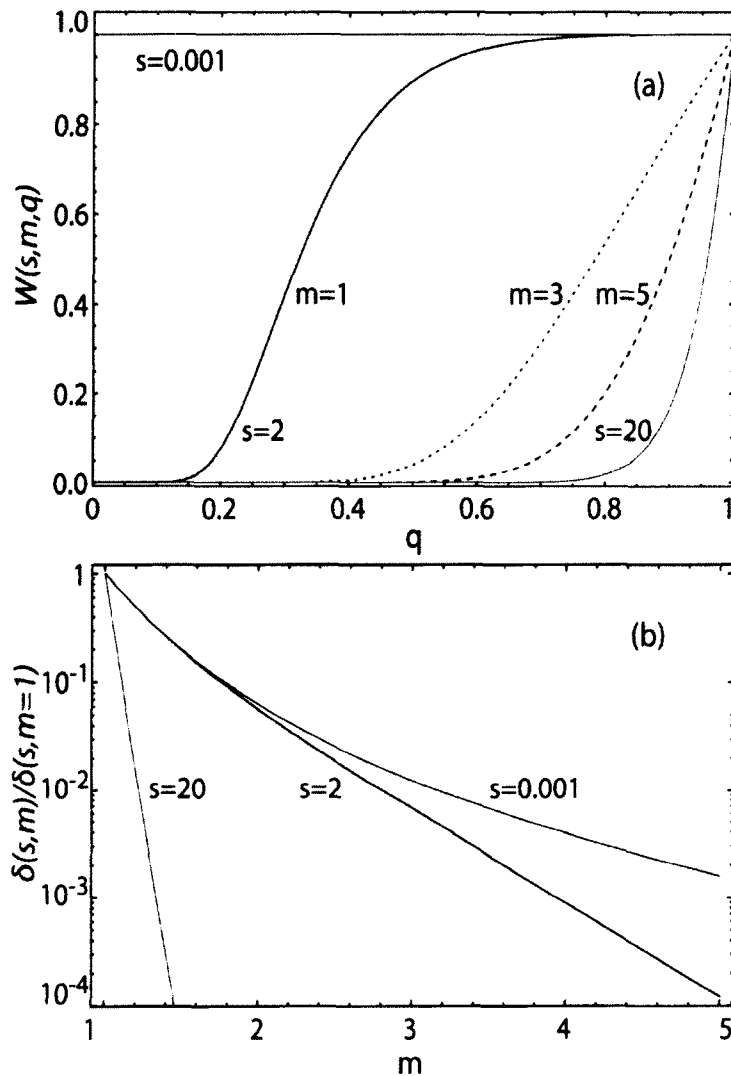


Figure 3.5: (a) The weight function $W(s, m, q)$ for $m = 1$ (solid blue), $m = 3$ (dotted blue), and $m = 5$ (dashed blue) for fixed $s = 2$, and different values of $s = 0.001$ (solid red) and $s = 20$ (solid green) for fixed $m = 1$. (b) Plot of $\delta(s, m)$ normalized over its maximum value for $m = 1$, and for different plate separation distances $s = 0.001$ (solid red), $s = 2$ (solid blue), and $s = 20$ (solid green).

In Figure 3.5 (b), we analyze the function $\delta(s, m)$ which is to be summed up with the weighted specular functions (see Equation 3.10). The function $\delta(s, m)$ determines the magnitude of the force, as the weight function is normalized $0 \leq W(s, m, q) \leq 1$ and $-1 \leq R_p^m(q) \leq 1$. In Figure 3.5 (b), we plot the normalized $\delta(s, m)$. The plot clearly shows that this function rapidly decreases with an increase in the values of m , regardless

of the separation distances s . For large plate separations or high temperatures or both $s \gg 1$, $m = 1$ term in $\delta(s, m)$ is sufficient to reproduce the force $\delta(s \gg 1, m) \rightarrow \delta(s, m = 1)$. It is important to note that in Figure 3.5 (b) the variation of $\delta(s, m)/\delta(s, m = 1)$ is continuous for different m ; however, we know that m is a discrete variable and only the values of $\delta(s, m)$ at $m = 1, 2, 3, \dots$ must be considered in the analysis.

For large plate separations or at high temperatures [see solid green curve in Figure 3.5 (b)], $m = 1$ is the dominant term, whereas with a decrease in the plate separations or temperature, for smaller separation distances [see solid red curve in Figure 3.5 (b)], though the force due to higher values of $m > 1$ contributes to the force, it may not be significant enough to change the sign of the force. To conclude, the $m = 1$ term in the summation is sufficient for further analysis of the Casimir force, and most importantly, the specular functions at $q \rightarrow 1$ is considered as the main factor that sets the signature of the force.

The analysis is much simplified when we consider the first term in the summation of Equation 3.10, which is the dominant as identified above. Furthermore, by the parametric sweep, it can be shown that the force has minima/maxima (extreme values) for $s = s_e \geq 2$. Hence, by substituting $s = 2$, we obtain a simplified form of the Casimir force at minima/maxima as,

$$F(s = s_e) = F_\infty + \frac{k_B T}{8\pi d^3} \sum_p \int_0^1 \delta(q) R_p(q) dq, \quad \text{Eq. 3.11}$$

where $\delta(q) = (1/q^4)[2 + \text{Cosh}(2/q)]\text{Csch}(1/q)^4$.

The function $\delta(q)$ now plays the role of a weight for the specular functions $R_p(q)$. More importantly, the weight function $\delta(q)$ is similar to that of a Heaviside function and can be approximated as $\delta(q) = \delta(1)\theta(q - q_c)$. The cutoff wave vector is obtained from

the normalization condition $\int_0^1 \delta(q) = \delta(1)(1 - q_c)$ and can be explicitly written as $q_c = (1 + e^2 + 23e^4 - e^6)/[4(e^2 + 4e^4 + e^6)] = 0.342$. Equation 3.11 is written in terms of new limits for the integral as,

$$F(s = s_e) = F_\infty + \frac{k_B T}{8\pi d^3} \delta(1) \sum_p \int_{q_c}^1 R_p(q) dq. \quad \text{Eq. 3.12}$$

Although the Casimir force in Equation 3.12 can be presented in a short form by explicitly performing the integral, the end result is rather cumbersome. However, it can be utilized to perform a fast parametric swipe and identify the conditions for the kink in the force. These are given as,

1. *Positive kink*: $F_0 > 0, F_\infty > 0, R_p(1) < 0$ and $F(s = s_e) < 0$ and
2. *Negative kink*: $F_0 < 0, F_\infty < 0, R_p(1) > 0$ and $F(s = s_e) > 0$.

In Figure 3.6 we have plotted the conditions for *positive* and *negative kinks* along with the sufficient conditions for Casimir force reversal. Figure 3.6 is analogous to Figure 3.4 and provides the parametric regions for which different types of the Casimir force reversals could be achieved. It is important to note that the condition provided for the kinks are not sufficient conditions; however, it closely captures the parametric region required for achieving the kinks (black domains in Figure 3.6).

The description of different regions in Figure 3.6 are as follows:

- i. First quadrant: The red domain shows the region where the force is attractive under the condition $R_p(1) > 0$ (type 1). The gray domain corresponds to $R_p(1) < 0$, and the black domain with $F(s = s_e) < 0$ (type 5). Both satisfy the necessary condition for the *negative kink*.

- ii. Second quadrant: The light orange domain with $R_p(1) > 0$ shows the region where the force is attractive for small separation distances and repulsive for large separation distances (type 3).
- iii. Third quadrant: The orange domain shows the region where the force is repulsive with $R_p(1) < 0$ (type 2). The gray domain with $R_p(1) > 0$ and the black domain with $F(s = s_e) > 0$ (type 6), both satisfying the necessary condition for the *positive kink*.
- iv. Fourth quadrant: The yellow domain with $R_p(1) < 0$ shows the region where the force is repulsive for small separation distances and attractive for large separation distances (type 4).

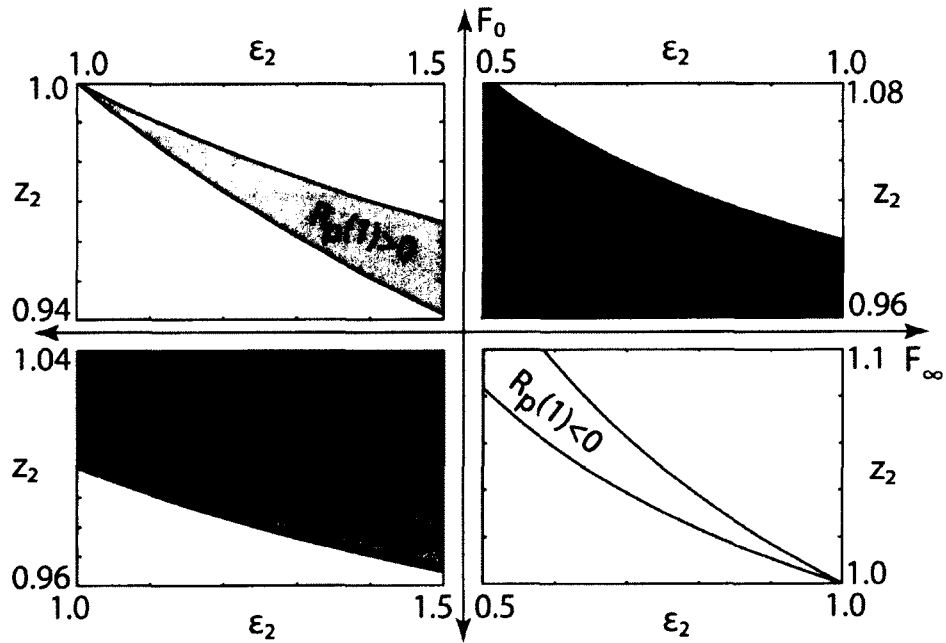


Figure 3.6: Parametric plot showcasing the parametric domains that identify the different types of the Casimir forces. The domains are plotted for fixed $\epsilon_1 = 5$ and $z_1 = 0.05$.

Using the parametric region plots as per Figure 3.6, we pick six different configurations (one from each domain, except the gray domains) to illustrate the types of Casimir forces that can be expected (see Figure 3.7). The material parameters for plate 1 is fixed as $\epsilon_1 = 5$ and $z_1 = 0.05$, and the properties of plate 2 is varied. For type 1: $\epsilon_2 = 0.7$ and $z_2 = 0.98$, type 2: $\epsilon_2 = 1.2$ and $z_2 = 1.05$, type 3: $\epsilon_2 = 1.5$ and $z_2 = 0.95$, type 4: $\epsilon_2 = 0.5$ and $z_2 = 1.1$, type 5: $\epsilon_2 = 0.5$ and $z_2 = 1.09$, and type 6: $\epsilon_2 = 4$ and $z_2 = 0.9072$.

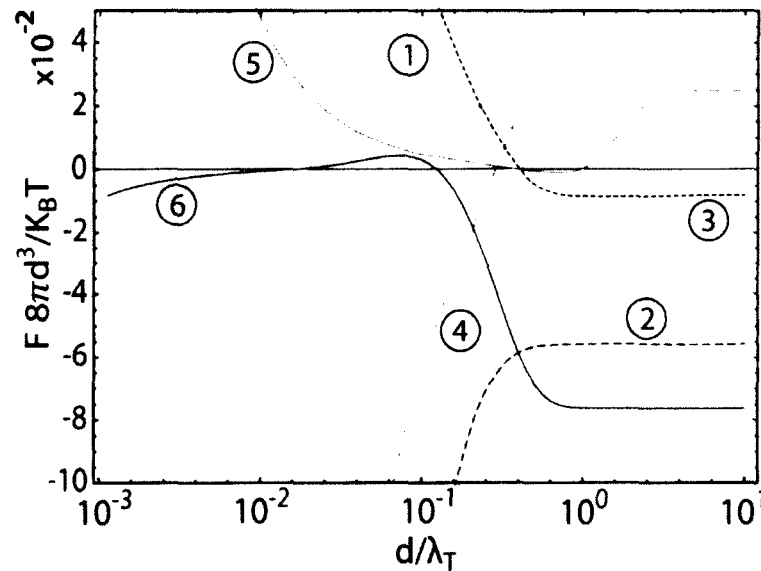


Figure 3.7: Six different types of the Casimir forces: ① type 1 (dashed orange), ② type 2 (dashed purple), ③ type 3 (dashed blue), ④ type 4 (dashed gray), ⑤ type 5 (green), and ⑥ type 6 (red).

In this section, we have studied six different types of Casimir force behavior (as the function of plate separation distance) that can be expected for non-dispersive plates. Each of the six cases can be considered for various practical applications based on the requirements of attraction or repulsive for different separation distances. For instance, let us consider type 4, which is repulsive for small plate separations and attractive for large plate separations. For this case, one particular application could be in a quantum levitating

system with one of the plates levitated on top of the other. The plate will be at an equilibrium distance from one another such that the force is zero. This system could be used to transport materials with no friction (in vacuum). For practical designs, we also need to include other associated forces such as gravitational force, etc. It is important to note that, of all six cases, the configurations with kinks in the force are extremely difficult to achieve practically since the parametric domain corresponding to those specific cases are extremely narrow.

3.5 Challenges in Realizing the Six Universal Casimir Force Types

Although there are six different Casimir force types, it may not be possible to realize all of them in practice. Some of the challenges include finding naturally existing or artificially designed material with a strong magnetic response, or a material with optical gain, for a broad range of frequencies. Since the main focus is to achieve quantum levitation of nanoscale devices, we have to note that these devices commonly contain metallic layers or dielectric coatings that are dispersive in nature. We already discussed the fact that these materials are described using one of three analytical models, namely the Lorentz oscillator, Drude, and Debye models [16, 69, 70]. Thus, the assumption of non-dispersivity and the analyses above provide the knowledge regarding the material properties required to achieve different types of the Casimir force. However, while practically designing a system the dispersive properties of the constituent materials need to be considered.

According to the Lorentz oscillator model [16], the permittivity and permeability of a dissipative material is always positive and larger than unity (at the complex Matsubara frequencies). However, the permittivity/permeability could be negative when gain is present. It is worthwhile to note that active (gain) materials had already been considered

for the prospect of achieving quantum levitation by Leonhardt and Philbin [44], and Y. Sherkunov [41]. Generally, optical gain in metamaterials [71] is attained through optical pumping [39] or quantum cascade lasing techniques [40] which would disturb the thermal equilibrium of the system. Therefore, in the case of gain media the contribution of excited-state emission of electrons and the thermal fluctuations (due to pumping of electrons) has to be considered in the calculation of the Casimir force. As the Lifshitz theory is based on fluctuation-dissipation theory, which demands thermal equilibrium, for the applicability of Lifshitz theory in the case of gain, a media is highly doubtful [42].

Recently, theories that include the effects of gain has been proposed [41, 42]. These works have shown that a correction factor has to be added to the vacuum force predicted by the Lifshitz theory in order to account for the emission of electrons from excited states [42]. Although the role of gain may hold the key in reversing the force, for in-depth analysis, the correction factors to the Lifshitz theory have to be considered, which is out of the scope of this thesis. Hence, in the rest of this work we consider only dissipative materials with the permittivities and permeabilities of the plates described by the Lorentz oscillator model and thus always larger than unity ($\epsilon > 1$ & $\mu > 1$). While materials with $\epsilon \gg 1$ do exist in nature (metals), magnetic materials with $\mu \gg 1$ are difficult to find. In Chapter 6, we will identify a variety of strategies that may allow for artificial engineering of such magnetic materials.

In addition to the well-known conditions for force reversal proposed by Boyer [43], Dzyaloshinskii [17], and Leonhardt [44], our analyses from above and due to other authors [26, 27, 32–36, 72] show that quantum levitation could be achieved for a broad range of material properties. In order to identify a practically feasible configuration with

repulsive Casimir force, we identify and analyzed all available conditions below. The discussion is inclusive with the only exception being Leonhardt's condition, as we focused only on systems with air as the intermediate medium.

1. Boyer's condition: $\epsilon_1 \rightarrow \infty, \mu_1 \rightarrow 1$ and $\epsilon_2 \rightarrow 1, \mu_2 \rightarrow \infty$.

According to Boyer's condition, one of the plates has to be perfectly metallic and nonmagnetic (note that at imaginary frequencies $\epsilon \gg 1$ for metals) while the other plate has to be perfectly magnetic with weak (non-existent) electric polarizability [43]. While natural materials with strong dielectric response and weak (non-existent) magnetic response do exist (for instance noble metals), it is not clear how to develop a material with a strong magnetic response without a dielectric response (no such material exists in nature).

2. Kenneth *et al.* condition: $\epsilon_1 > 1, \mu_1 \rightarrow 1$ and $\epsilon_2 \rightarrow 1, \mu_2 > 1$.

Kenneth *et al.* condition [33] is a relaxed form of Boyer's condition where again the levitating configuration includes one of the plates being non-magnetic while the other must be non-dielectric, but the difference is that the permeabilities and permittivities are now finite. Still, this condition is difficult to achieve in practice since as we mentioned earlier it is not clear how one can have a material with magnetic response but no dielectric response.

3. Dzyaloshinskii's condition: $\epsilon_2 > 1 > \epsilon_1$ and/or $\mu_2 > 1 > \mu_1$.

As we discussed above, if a material is not active and described by the Lorentz oscillator model, its permittivity and permeability are always larger than unity. To achieve Dzyaloshinskii's condition with air/vacuum as the intermediate medium, one of the plates must have $\epsilon < 1$ and/or $\mu < 1$ [17]. This suggests that one of the plates need to be diamagnetic and the other a paramagnetic plate for quantum levitation. Hence, this

condition is not practical for air/vacuum as the intermediate medium, and if the plates are described by the Lorentz oscillator model. However, if the material properties are described using a model other than the Lorentz oscillator model (such as Pendry's model), then the permittivity and permeability of a material could be less than unity when estimated at the Matsubara frequencies. Such possible materials will be discussed in more details in Chapter 6.

4. Leonhardt's condition: $\epsilon_2 > 1$, $\epsilon_1 > 1$ and $\epsilon_{medium} < 0$.

Leonhardt's condition requires a negative index medium as an intermediate medium [44]. To realize negative values for the permittivity and/or permeability (in complex frequencies), both dielectric and magnetic gain is required, and hence, this configuration is not practical.

5. Magneto-dielectric plates with $\mu_1 < \epsilon_1$ and $\mu_2 > \epsilon_2$.

According to this configuration, one of the plates needs to be strongly magnetic and the other is strongly dielectric [27, 30, 36, 52, 72]. This condition could be achieved even in the case of air/vacuum as the intermediate medium. One of the plates could be a simple dielectric with $\epsilon_1 > \mu_1 = 1$. However, the challenging task is to design a strongly magnetic material with $\mu_2 > \epsilon_2$. No such material exists in nature, and thus, it must be engineered. Particular nanostructured materials that could satisfy such a condition may be a ferromagnetic material in a low permittivity dielectric host [32], geometrically optimized split ring resonators (SRR) with resonance frequencies in the optical and near infrared frequency range [73], dielectric spheres [74], dielectric rectangular plates [75], or Bi-Helix structures [76].

CHAPTER 4

CASIMIR FORCE BETWEEN A WEAKLY DISPERSIVE DIELECTRIC PLATE AND A METAMATERIAL PLATE

4.1 Introduction

In this chapter, we study the Casimir force for systems with material properties that are similar to that of NEMS or MEMS devices in which the permittivity of the material is approximately constant for a wide range of frequencies and can be assumed to be non-dispersive and non-magnetic. Hence, we consider plate 1 to be a weak dispersive dielectric plate and non-magnetic and plate 2 as dispersive with arbitrary values for the permittivity and permeability. Examples for weakly dispersive materials are Si, glass, and etc., with permittivity and permeability that are nearly constant for a broad range of frequencies. Plate 2 is considered to be a metamaterial plate with arbitrary values of the permittivity and permeability. Metamaterials have been demonstrated across the microwave, infrared and optical frequency [56, 58, 73, 75–85]. Our goal is a sufficient condition for quantum levitation, which will be a useful tool in designing practical systems that could help resolve the stiction problem in nanoscale devices. Again, similar to the previous studied configurations, we assume that the thickness of the plates are much larger compared to the separation distance between the plates ($t \gg d$), and both plates are dissipative.

4.2 Lorentz Oscillator Model for Dispersive Magneto-Dielectric Properties

The optical response of plate 1 and plate 2 are modeled using the Lorentz oscillator model with the permittivities and permeabilities at the discrete complex Matsubara frequencies given as,

$$\varepsilon_l(i\omega_n) = 1 + \frac{\omega_{pe,l}^2}{\omega_{0e,l}^2 + \omega_n^2 + \gamma_{e,l}\omega_n}, \quad \text{Eq. 4.1}$$

$$\mu_l(i\omega_n) = 1 + \frac{\omega_{pm,l}^2}{\omega_{0m,l}^2 + \omega_n^2 + \gamma_{m,l}\omega_n}, \quad \text{Eq. 4.2}$$

where $(\omega_{0e,l}, \omega_{0m,l})$ and $(\omega_{pe,l}, \omega_{pm,l})$ are the plates' electric and magnetic resonance and plasma frequencies, respectively. The dissipation rates $(\gamma_{e,l}, \gamma_{m,l})$ are positive if the material is dissipative and negative if there is a gain. The suffix l represents the plate number ($l = 1, 2$). We note that provided the resonant frequency of the first plate is much greater than the resonant frequency of the second plate, $\omega_{0e,1} \gg \omega_{0e,2}$, we can approximate that the first plate is weakly dispersive without affecting the results since for all modes with $\omega_n \geq \omega_{0e,1} \gg \omega_{0e,2}$, where the dispersive properties of plate 1 become important, we have $R_p^n(q) \rightarrow 0$ and the contribution of these modes to the Casimir force is negligible. Therefore, the electromagnetic properties of plate 1 are $\varepsilon_1(i\omega_n) = \varepsilon_1 = \text{constant}$ and $\mu_1 = 1$. Assuming the specular functions' dissipative materials for the plates are given as,

$$R_{TM}^n(q) = \left(\frac{\varepsilon_l - \sqrt{(\varepsilon_l \mu_l - 1)q^2 + 1}}{\varepsilon_l + \sqrt{(\varepsilon_l \mu_l - 1)q^2 + 1}} \right)^2 \geq 0, \quad \text{Eq. 4.3}$$

$$R_{TE}^n(q) = \left(\frac{\mu_l - \sqrt{(\varepsilon_l \mu_l - 1)q^2 + 1}}{\mu_l + \sqrt{(\varepsilon_l \mu_l - 1)q^2 + 1}} \right)^2 \geq 0. \quad \text{Eq. 4.4}$$

It is important to note that if the two plates have the same optical properties the specular functions are positive for all parameters (see Equations 4.3 and 4.4) and the Casimir force is positive (attractive) or zero for all separation distances. The classical example of two perfect metal plates, used by Casimir, falls in the same category and thus the force in this case is attractive [9]. Hence, to achieve force reversal, it is necessary to design a system where the two plates are dissimilar in nature. We must also note that the split ring resonators (SRRs) are one of the promising candidates for the design of metamaterials with a strong magnetic response [73, 84]. When describing the magnetic permeability of complex metamaterials based on the SRRs, it is common to use the Pendry model [73], according to which,

$$\mu_{SRR}(\omega) = \mu'_{SRR} + i\mu''_{SRR} = 1 + \frac{f\omega^2}{\omega_0^2 - \omega^2 - i\omega\omega_\tau}, \quad \text{Eq. 4.5}$$

and for imaginary Matsubara frequencies,

$$\mu_{SRR}(i\omega_n) = 1 - \frac{f\omega_n^2}{\omega_0^2 + \omega_n^2 + \omega_\tau\omega_n}, \quad \text{Eq. 4.6}$$

where f is the SRR's filling fraction and ω_τ is the constant relaxation frequencies (does not depend on ω_n). Though Pendry's model accurately describes the permeability of the SRR at low frequencies (compared to width of the SRR), it is invalid at high frequencies as it provides unphysical values for permeability $\lim_{n \rightarrow \infty} \mu(i\omega_n) = 1 - f < 1$ and cannot be used without proper modifications in the calculation of the Casimir force, where summation for the overall modes needs to be performed. Furthermore, Pendry's model does not satisfy the causality. In considering the asymptotic behavior for large frequencies, we obtain $\lim_{\omega \rightarrow \infty} (\mu'_{SRR} - 1) = f$ [violating the $1/\omega^2$ asymptotic required by Kramers-Kronig relation], and $\lim_{\omega \rightarrow \infty} \mu''_{SRR} \propto 1/\omega$ (violating the $1/\omega^3$ asymptotic required by the

Kramers-Kronig relation) [86]. Hence, in our work, we restrict our study to EMMs that can be described by the Lorentz oscillator model.

4.3 Casimir Force Reversal at High and Low Temperatures

For the material configuration under consideration, the Casimir force at large and small separation distances compared to the thermal wavelength ($\lambda_T = 2\pi c/\omega_T$) can be determined using Equations 2.37 and 2.44 and by utilizing the corresponding specular functions provided in Equations 2.39, 2.40, 2.45, and 2.46. For the permittivities and permeabilities of the plates, we use the Lorentz oscillator model provided in Equations 4.1 and 4.2, respectively.

In the case of large plate separations, we have already shown that the force is accurately defined by the $n = 0$ term, and we have $\varepsilon_l = 1 + \omega_{pe,l}^2/\omega_{0e,l}^2 \geq 1$ and $\mu_l = 1 + \omega_{pm,l}^2/\omega_{0m,l}^2 \geq 1$. Consequently, the specular functions are positive ($0 \leq R_p^0 \leq 1$) and so is the force (attractive). We must note that the attractive nature of the Casimir force in the high temperature limit have already been discussed in the case of non-dispersive materials [28, 33]. Here, however, we show that for realistic dispersive materials, the Casimir force will reverse to attractive even for cryogenic temperatures provided the plates' separation is sufficiently large ($d \gg \lambda_T$) or sufficiently small ($d \ll \lambda_T$) as shown next.

In the case of small plates separations, we have $\varepsilon_l(i\omega_n)$ and $\mu_l(i\omega_n)$. When the plates are dissipative with $\gamma_{e,l} > 0$ and $\gamma_{m,l} > 0$, we have $0 \leq R_p^n(0) \leq 1$ and the force is attractive, regardless of the nature of the plates. However, if gain is present the force may turn into repulsive provided (i) $\varepsilon_1(i\omega_n) < 1 < \varepsilon_2(i\omega_n)$ and/or (ii) $\mu_1(i\omega_n) < 1 <$

$\mu_2(i\omega_n)$ when one of the plates is diamagnetic and the other is paramagnetic. We must note that this approach is a particular manifestation of the Boyer's condition for the Casimir force reversal [43] here with vacuum as the intermediate media and as discussed by Kenneth *et al.* [33]. Metamaterials with loss compensation have been reported recently [39, 71], which suggests that use of gain may be a feasible approach for achieving repulsive force.

Though the validity of the Lifshitz theory is questionable in the case of gain medium [41,87], we show here that even if the Lifshitz theory is applicable, extremely high gain is required for repulsion. We consider the best case scenario where one of the plates (plate 1) is dissipative while the other (plate 2) is active. An inspection of Equations 4.1 and 4.2 reveals the condition for signature change of the specular functions which is,

$$|\gamma| \geq \frac{\omega_T^2 + \omega_c^2}{\omega_T}, \quad \text{Eq. 4.7}$$

where $\gamma = (\gamma_{e,1}, \gamma_{m,1})$ and $\omega_c^2 = (\omega_{0e,1}^2, \omega_{0m,1}^2)$. If this condition is satisfied, then negative contributions to the force are provided by all terms in Equation 2.35 with Matsubara frequencies in the range $\gamma - \sqrt{\gamma^2 - 4\omega_c^2} \leq 2\omega_n \leq \gamma + \sqrt{\gamma^2 - 4\omega_c^2}$. The condition in Equation 4.7 clearly shows that extremely high gain across a broad frequency range must be applied. For instance, in the case of metals (silver) that are commonly used in the design of metamaterials and under ambient condition ($T = 300K$), one must have $\gamma > \omega_T/c = 8200cm^{-1}$. It is difficult to conceive how such levels of gain across a broad frequency range can be achieved in practices. Hence, material gain may no longer be considered for Casimir force reversal. In addition, as mentioned in the previous chapter (see chapter 3.5), the effect of spontaneous emission of electrons from higher energy levels

and the thermal fluctuations has to be considered while calculating the Casimir force [41, 87].

As the specular functions are always positive for both large and small separation distances, we conclude that under realistic material configurations relevant to MEMS/NEMS devices, which generally consist of dissipative dielectric materials lacking magnetic response, and by considering EMM as plate 2, the Casimir force is always attractive (positive) or zero for a large and a small plate separation distances. Nevertheless, the force could be reversed for a range of intermediate separation distances as we will show below.

4.4 Upper Bound of the Casimir Force

To reduce the complexity of the analysis, both the plates are assumed to be dispersive with relatively low losses ($\gamma_{m,l} \ll \omega_{0m,l}$ and $\gamma_{e,l} \ll \omega_{0e,l}$) and the role of the dissipation factor in reversing the Casimir force is not considered. To derive a sufficient condition for the Casimir force reversal, we seek an upper analytical bound \bar{F} of the force in Equation 2.35 such that $F \leq \bar{F}$ for all plate separation distances. Since dissimilar plates are required for repulsion, we chose one of the plates to be purely dielectric while the other is dominantly magnetic at least for a finite set of frequencies such that $z_2 = \sqrt{\mu_2/\epsilon_2} > 1$. In this case, the specular functions are confined within the strict limits $R_p^n(1) \leq R_p^n(q) \leq R_p^n(0)$, where $R_p^n(1) < 0$, $R_{TM}^n(0) \geq 0$ and $R_{TE}^n(0) = 0$, with a single or no real roots. Since $-1 \leq R_p^n(q) \leq 1$, it can be shown by the parametric swipe that for $n \geq 1$ and within the domain of applicability of the normalized wave vector $q \in (0,1)$, the following upper bound of the specular functions hold

$$\sum_p \text{Li}_0[R_p^n(q)e^{-ns/q}] \leq \sum_p \tilde{R}_p^n(q)e^{-ns/q}, \quad \text{Eq. 4.8}$$

where $\tilde{R}_p^n(q) = R_p^n(1)q^2 + R_p^n(0)(1 - q^2) \geq R_p^n(q)$.

Figure 4.1 shows the parametric domains for which the upper bound (Equation 4.8) is not satisfied (red) and for which the force is repulsive (blue). In both cases [Figures 4.1 (a) and (b)], the material parameters of plate 1 are fixed as $\epsilon_1 = 2$ and $\mu_1 = 1$, and the material properties of plate 2 is varied. The upper bound is not satisfied for $\mu_2 < 1$ and the force could be repulsive only for $\mu_2 > 1$. Thus, by considering the system for $z_2 = \sqrt{\mu_2/\epsilon_2} > 1$, our upper bound holds and can be used to derive sufficient condition for the force reversal.

Direct integration of the force in Equation 2.35 represented by its upper bound Equation 4.8 immediately follows as,

$$\begin{aligned} \tilde{F} = F_\infty + \frac{k_B T}{8\pi d^3} \sum_p \sum_{n=1}^{\infty} e^{-ns} \left(2R_p^n(0)(1 \right. \\ \left. + ns) + n^2 s^2 R_p^n(1) \right). \end{aligned} \quad \text{Eq. 4.9}$$

We note that the first term in the sum is always positive [$R_p^n(0) \geq 0$] and the repulsive Casimir force may be provided only if $R_p^n(1) < 0$, which is our necessary condition for at least one vacuum mode. This implies that with the first plate purely dielectric ($z_1 < 1$), plate 2 has to be dominantly magnetic with $z_2 = \sqrt{\mu_2/\epsilon_2} > 1$ to have the possibility of force reversal.

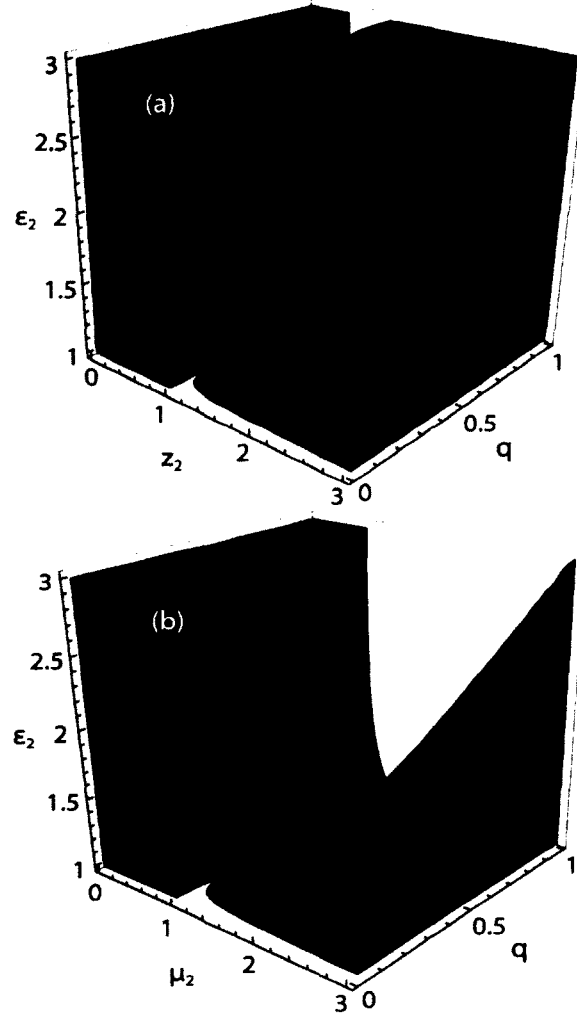


Figure 4.1: The parametric domains corresponding to the cases where the upper bound (Equation 4.8) is not satisfied (red) and the force is repulsive $F < 0$ (blue). In the calculation we use $\varepsilon_1 = 2$ and $ns = 2$, (a) plotted in terms of z_2 and (b) plotted in terms of μ_2 .

The first term in the sum, Equation 4.9 can then be estimated explicitly giving,

$$\begin{aligned} \tilde{F} = F_\infty + \frac{k_B T}{8\pi d^3} & \left[\left\{ \frac{R_{TM}^1(0)(\Omega + i)e^{-s}}{\Omega} [{}_2F_1(1, 1 + i\Omega; 2 \right. \right. \\ & \left. \left. + i\Omega; e^{-s}) + s {}_2F_1(2, 1 + i\Omega; 2 + i\Omega; e^{-s}) \right] \right. \\ & \left. - c.c. \right\} + \sum_p \sum_{n=1}^{\infty} e^{-ns} n^2 s^2 R_p^n(1) \right], \end{aligned} \quad \text{Eq. 4.10}$$

where $\Omega = (1/\omega_T) \sqrt{\omega_{0e,2}^2 + \omega_{pe,2}^2/2}$ and ${}_2F_1$ is the Gauss hypergeometric function. For the general case of plate 2 having both magnetic and dielectric responses, the remaining sum in Equation 4.10 does not have an exact solution. However, if we impose the restriction $R_p^n(1) < 0$ for all n , which is equivalent of having simultaneously $\omega_{pe,2}\omega_{om,2}/\omega_{pm,2}\omega_{oe,2} < 1$ and $\omega_{pe,2}/\omega_{pm,2} < 1$, then we can consider the lower bound of this sum through the related generalized hypergeometric function,

$$\begin{aligned} \sum_p \sum_{n=1}^{\infty} e^{-ns} n^2 s^2 R_p^n(1) \\ \leq 2R_{TM}^1(1) s^2 e^{-s} {}_4F_3[2, 2, \alpha, \alpha; 1, \alpha + 1, \alpha \\ + 1; e^{-s}], \end{aligned} \quad \text{Eq. 4.11}$$

where $\alpha = (1/\omega_T) \sqrt{(\omega_{pm,2}^2 - \omega_{pe,2}^2)/4r_{TM,2}^1(1)}$.

We note that this lower bound of the negative contributions to the force leads to an upper bound for the total force (see Equation 4.12) and captures the exact dependence of the sum for small and large mode numbers. The upper bound of the Casimir force thus can be written in the explicit analytical form as,

$$\begin{aligned} \bar{F} = F_{\infty} + \frac{k_B T e^{-s}}{8\pi d^3} \left[2R_{TM}^1(1) s^2 {}_4F_3(2, 2, \alpha, \alpha; 1, \alpha + 1, \alpha \\ + 1; e^{-s}) \right. \\ \left. + \left\{ \frac{R_{TM}^1(0)(\Omega + i)}{\Omega} [{}_2F_1(1, 1 + i\Omega; 2 + i\Omega; e^{-s}) \right. \right. \\ \left. \left. + s {}_2F_1(2, 1 + i\Omega; 2 + i\Omega; e^{-s})] - c. c. \right\} \right], \end{aligned} \quad \text{Eq. 4.12}$$

where *c. c.* represents the complex conjugate of the corresponding terms.

To compare the upper bound with the actual Casimir force, we plotted them at different plasma frequencies and at different temperatures. Figure 4.2 shows a comparison between the Casimir force (Equation 2.35) and the analytical upper bound (Equation 4.12). A repulsive domain appears with a decrease of plate 2's dielectric to the magnetic plasma frequency's ratio $\omega_{pe2}/\omega_{pm2}$ [Figure 4.2 (a)]. The repulsive domain also increases with a decrease in temperature [Figure 4.2 (b)], a fact that will be used below to derive a sufficient condition for the force reversal. In every case, and as expected, the upper analytical bound holds and capture the relevant physics.

Furthermore, we have included in the figures the large (or high temperatures) and small (or low temperatures) separation distance asymptotic of the Casimir forces calculated using Equations 2.37 and 2.44. The force is attractive in both cases and scales as $1/d^3$ with the distance. Only for intermediate plates' separations, the force becomes repulsive.

The proper behavior of the upper bound allows for the derivation of a simple sufficient condition for the force reversal. We consider the high temperature limit ($\Omega \ll 1$, $\alpha \ll 1$) or the worst case scenario and expand Equation 4.12 in the power series. After simple algebraic manipulations, we obtain the leading terms in the expansion,

$$\begin{aligned} \frac{8\pi d^3 \tilde{F}}{k_B T} \leq & \text{Li}_3[R_{TM}^0(0)] + 2R_{TM}^1(0)(\text{Li}_2[e^{-s}] + s\text{Li}_1[e^{-s}]) \\ & + 2s^2 R_{TM}^1(1)\text{Li}_0[e^{-s}]. \end{aligned} \quad \text{Eq. 4.13}$$

In the above result, we have used the general properties of the specular functions $R_{TM}^1(1) = R_{TE}^1(1)$ and $R_{TE}^n(0) = 0$ (plate 1 is non-magnetic). Taking into account that $R_{TM}^1(0) \leq R_{TM}^0(0)$ and enforcing the bounds of the polylogarithmic functions, we can further simplify Equation 4.13 by writing,

$$\frac{8\pi d^3 \tilde{F}}{k_B T} \leq R_{TM}^0(0) \left[\zeta(3) + \left(2s + \frac{\pi^2}{3} \right) e^{-s} \right] + 2R_{TM}^1(1) s^2 e^{-s}, \quad \text{Eq. 4.14}$$

where ζ is the Riemann zeta function.

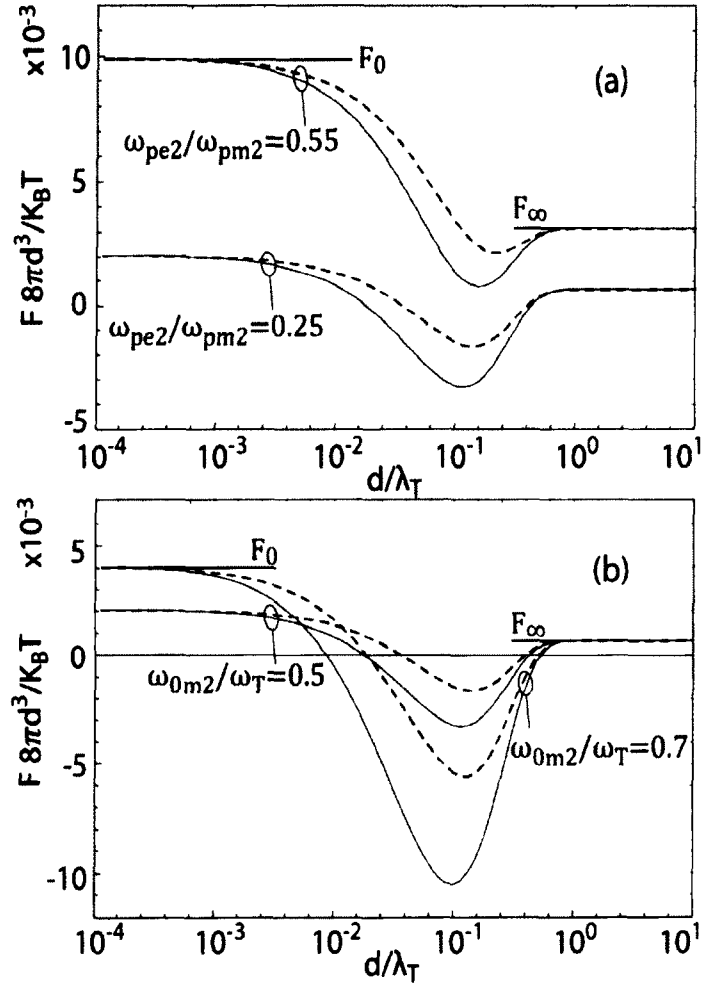


Figure 4.2: (a) The Casimir force (solid lines) and its upper bound (dashed lines) calculated for two ratios of plate 2's dielectric and magnetic plasma frequencies $\omega_{pe2}/\omega_{pm2}$ and fixed $\omega_{0m2}/\omega_T = 1$. (b) The temperature dependence of the force and its upper bound is calculated for different temperatures with fixed plasma and resonance frequencies $\omega_{pe2}/\omega_{pm2} = 0.25$, $\omega_{0e2}/\omega_{0m2} = 2$, and $\omega_{pm2}/\omega_{0m2} = 0.5$. The large distance F_∞ and the small distance F_0 asymptotic are included and in all calculations we have set plate 1's permittivity at $\epsilon_1 = 2$.

Figure 4.3 depicts the parametric domains for Casimir force reversal obtained from the analytical bounds in Equations 4.12 and 4.14. In the calculations we have restricted the

parametric space to assure that the bound's applicability condition $R_{TM}^n(1) = R_{TE}^n(1) < 0$ is satisfied for all n which is for $\omega_{pe2}\omega_{0m2}/\omega_{pm2}\omega_{0e2} < 1$ and $\omega_{pe2}/\omega_{pm2} < 1$. The figures also show the range of plate separation distances across which the Casimir force is repulsive.

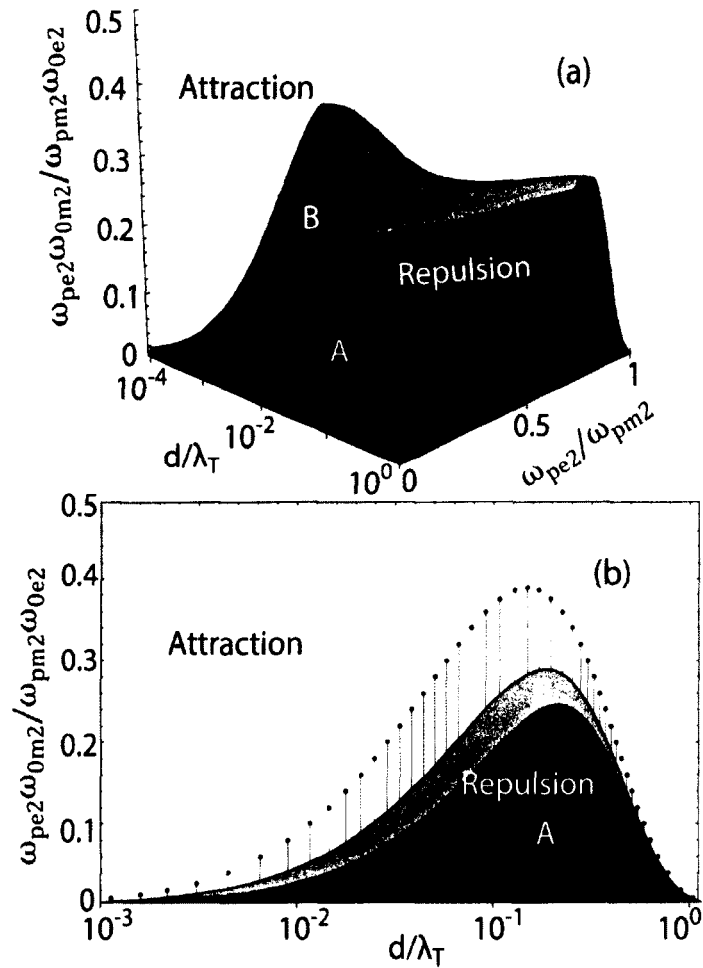


Figure 4.3: (a) Repulsive Casimir force domain according to Equation 4.14 (region *A*, blue) and Equation 4.12 (region *B*, gray). (b) The range of plate separation distances for force repulsion is calculated at fixed $\omega_{0m2}/\omega_T = 1$, and $\omega_{pe2}/\omega_{pm2} = \omega_{pm2}/\omega_{0m2} = 0.5$. The dots corresponds to the parametric domain for force reversal obtained through exact numerical solutions of the actual force given by Equation 2.35. In all cases we have set plate 1's permittivity at $\epsilon_1 = 2$.

As expected the parametric domains for Casimir force reversal obtained using the bounds in Equations 4.12 and 4.14 correspond to a subset of the parametric space obtained through exact numerical calculations using Equation 2.35, which would provide the sufficient condition for Casimir force repulsion. Furthermore, we observe that repulsion is only possible provided $\omega_{pe2}\omega_{0m2}/\omega_{pm2}\omega_{0e2} < 1$ and $d/\lambda_T \lesssim 1$ (which is $d \lesssim 7.64 \mu m$ at 300 K).

4.5 Sufficient Condition

The upper bound of the Casimir force in Equation 4.14 is easier to tackle analytically and allows for an explicit solution for the plate separation distance at the minima, which is

$$s_{min} = 1 + \frac{R_{TM}^0(0)}{2 |R_{TM}^1(1)|} + \sqrt{1 + \left(\frac{R_{TM}^0(0)}{2 |R_{TM}^1(1)|}\right)^2 + \frac{\pi^2}{6} \frac{R_{TM}^0(0)}{|R_{TM}^1(1)|}} \quad \text{Eq. 4.15}$$

From the minima of the plate separation distance, we could determine the material properties required to achieve repulsive force at s_{min} .

Figure 4.4 shows the repulsive Casimir force domain for different temperatures (ω_{0m2}/ω_T) shown in different colors. The dashed line represents the $\omega_{pe2}/\omega_{pm2}$ required for achieving repulsive at s_{min} . Hence, it is obvious from the figure that we need $\omega_{pe2}/\omega_{pm2} \leq \left|\omega_{pe2}/\omega_{pm2}\right|_{s=s_{min}}$ to reverse the force. In addition, in Figure 4.4 for a particular value of $\omega_{pe2}/\omega_{pm2}$ less than the $\left|\omega_{pe2}/\omega_{pm2}\right|_{s=s_{min}}$, the width of the repulsive domain represents the width of the repulsive window. Therefore, for a fixed value of $\omega_{0e2}/\omega_{0m2}$, a higher magnetic plasma frequency over the dielectric plasma frequency

is needed for the force reversal. The smaller the $\omega_{pe2}/\omega_{pm2}$ ratio, the wider the repulsive window.

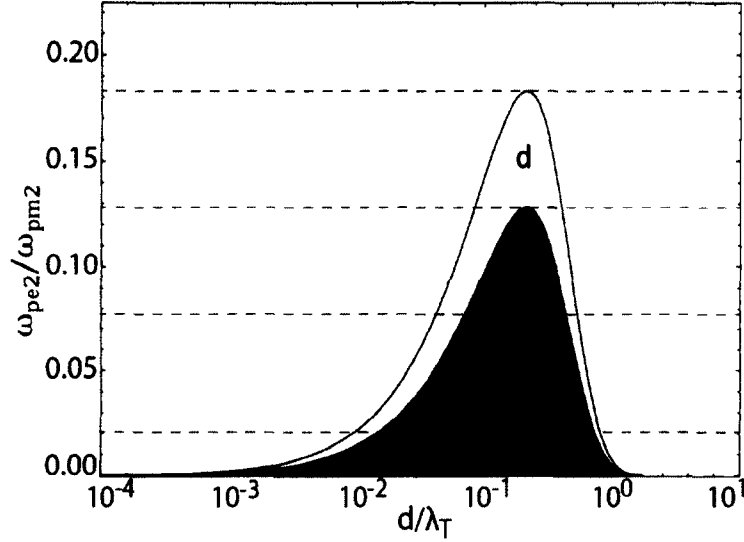


Figure 4.4: Plot showing the $\omega_{pe2}/\omega_{pm2}$ required for achieving repulsion at different temperatures (a) $\omega_{0m2}/\omega_T = 0.1$, (b) $\omega_{0m2}/\omega_T = 0.4$, (c) $\omega_{0m2}/\omega_T = 0.8$, and (d) $\omega_{0m2}/\omega_T = 10$ for $\omega_{0e2}/\omega_{0m2} = 2$. The dashed line corresponding to each domain represents the $\omega_{pe2}/\omega_{pm2}$ required from our assumption for $s = s_{min}$.

Furthermore, with an increase in temperature, comparatively higher magnetic plasma frequency or lower dielectric plasma frequency (smaller $\omega_{pe2}/\omega_{pm2}$ ratio) is required than at low temperatures. In other words, for a particular value of $\omega_{pe2}/\omega_{pm2}$, the width of the repulsive window decreases with an increase in temperature and vice versa. Further increase in the temperature would close the repulsive window making the force attractive for all separation distances. For instance, when $\omega_{pe2}/\omega_{pm2} = 0.15$ (see the Figure 4.4) and $\omega_{0m2}/\omega_T = 10$ (yellow domain), the Casimir force is repulsive for a certain range of separation distances, whereas when the temperature is increased to have $\omega_{0m2}/\omega_T = 0.8$ (red domain), $\omega_{pe2}/\omega_{pm2} > \left| \omega_{pe2}/\omega_{pm2} \right|_{s=s_{min}}$ and therefore there is no repulsive window and the force is attractive for all separation distances.

Finally, estimating the upper bound (Equation 4.15) at $s = s_{min}$ and through further simplification we obtain the following sufficient conditions for the Casimir force repulsion:

$$|R_{TM}^1(1)| \geq 2R_{TM}^0(0) \text{ and } R_{TM}^1(1) < 0. \quad \text{Eq. 4.16}$$

It is important to note that with decreases in temperature, the minimum of the actual force in Equation 2.35 shifts towards smaller plate separations and the repulsive force at the minima increases. Hence, the sufficient condition holds regardless of the temperature.

The sufficient condition only involves the specular functions for the $n = 0$ and $n = 1$ modes in the limit of large and small transversal wave vectors. From the condition that $R_{TM}^1(1) = (z_1 - 1)(z_2 - 1)/(z_1 + 1)(z_2 + 1) < 0$ for $n = 1$, it is obvious that $z_2 > 1$ (since $z_1 < 1$) to have the possibility of force reversal. Hence, we term $R_{TM}^1(1) < 0$ as the necessary condition for force reversal and we have recovered the condition discussed by Kenneth *et al.* [33] using our analytical theory. The sufficient conditions are most promising in terms of realizing a Casimir force based levitation system, as it requires only the permittivities and the impedances of the plates for $\omega = 0$ and $\omega = \omega_T$, to determine whether the force will be repulsive or not.

The process of determining the optical properties of the plates required to achieve force reversal is as follows. First, the necessary condition $R_{TM}^1(1) = \frac{(z_1-1)(z_2(\omega_T)-1)}{(z_1+1)(z_2(\omega_T)+1)} < 0$ must be satisfied. Since $z_1 = 1/\sqrt{\epsilon_1} < 1$, it immediately follows that $z_2(\omega_T) > 1$, or the metamaterial plate must be predominantly magnetic at frequencies equal to the thermal frequency $\omega = \omega_T$. The second step involves the sufficient condition of Equation 4.16, which in using the definition of the specular function can be written as,

$$\frac{z_2(\omega_T) - 1}{z_2(\omega_T) + 1} - 2a(\epsilon_1) \frac{\epsilon_2(0) - 1}{\epsilon_2(0) + 1} > 0, \quad \text{Eq. 4.17}$$

where $a(\varepsilon_1) = 1 + 2\sqrt{\varepsilon_1}/(1 + \varepsilon_1) > 0$. More importantly, the sufficient condition of Equation 4.17 depends only on three independent parameters and the sign of the force can be inferred from the permittivities and the impedances of the plates at $\omega = 0$ and $\omega = \omega_T$. This fact dramatically simplifies the analysis since the original problem depends on seven independent parameters such as electric and magnetic plasma and resonant frequencies of plate 2, temperature, separation distance, and the permittivity of plate 1.

Figure 4.5 depicts the parametric domain where quantum levitation can be achieved. In general, the analysis can be performed either with respect to the values of the permittivities and permeabilities of the plates estimated at $\omega = 0$ and $\omega = \omega_T$ [Figure 4.6 (a)], or equivalently [Figure 4.6 (b)] one can involve the Lorentz oscillator model. In the latter case, it is convenient to introduce three compound parameters that uniquely define the repulsion domain and directly involves the resonance and plasma frequencies of the plates: $\omega_{pe,2}\omega_{om,2}/\omega_{pm,2}\omega_{oe,2}$, $\omega_{pe,2}/\omega_{pm,2}$, and $\omega_{om,2}/\omega_T$. The results show that there should be a large variety of magneto-dielectric materials that can in principle be used for quantum levitation. However, there are some important restrictions. Equation 4.17 directly follows that force reversal cannot be guaranteed for $\varepsilon_2(0) > [2a(\varepsilon_1) + 1]/[2a(\varepsilon_1) - 1]$, even in the case of the infinitely permeable plate [$z_2(\omega_T) \rightarrow \infty$]. Since $1 \leq a(\varepsilon_1) \leq 2$, it is clear that one must have $\varepsilon_2(0) < 3$ in order for the sufficient condition to be satisfied. In terms of the dielectric plasma and resonance frequencies, this restriction translates as $\omega_{pe,2} \leq \omega_{oe,2}\sqrt{2}$.

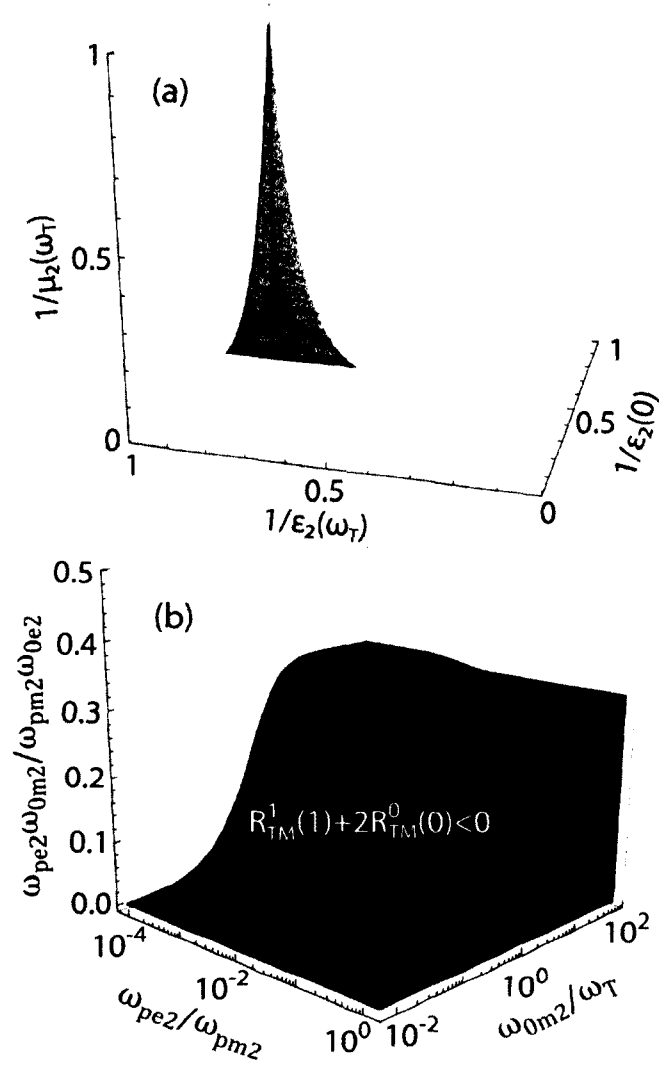


Figure 4.5: Quantum levitation in magneto-dielectric plate configurations. (a) The complete parametric domain for Casimir force reversal according to the sufficient condition in Equation 4.17. (b) The parametric domain represented by the optical constants described Lorentz oscillator model with $\omega_{pm2}/\omega_{0m2} = 0.5$. In all cases, we have set plate 1's permittivity as $\epsilon_1 = 2$.

Figure 4.6 shows the comparison of the parametric domains for repulsion provided by the sufficient conditions in Equation 4.17 and obtained from direct numerical calculations of Equation 2.35. As expected for all parameters the sufficient condition holds. From Figure 4.5 (b) and Figure 4.6, we observe that force reversal is possible only if $\omega_{pe2}\omega_{0m2}/\omega_{pm2}\omega_{0e2} < 1$, which also implies that provided the magnetic and dielectric

plasma frequencies of the magneto-dielectric plate 2 are matched ($\omega_{0m2} = \omega_{0e2}$), then $\omega_{pm2} > \omega_{pe2}$ or plate 2 must be predominantly magnetic. This requirement becomes rather extreme in the limit of very high temperatures with $\omega_{pm2}/\omega_{pe2} \rightarrow \infty$ for $\omega_{0m2}/\omega_T \rightarrow 0$ [see Figures 4.5 (b) and 4.6 (a)].

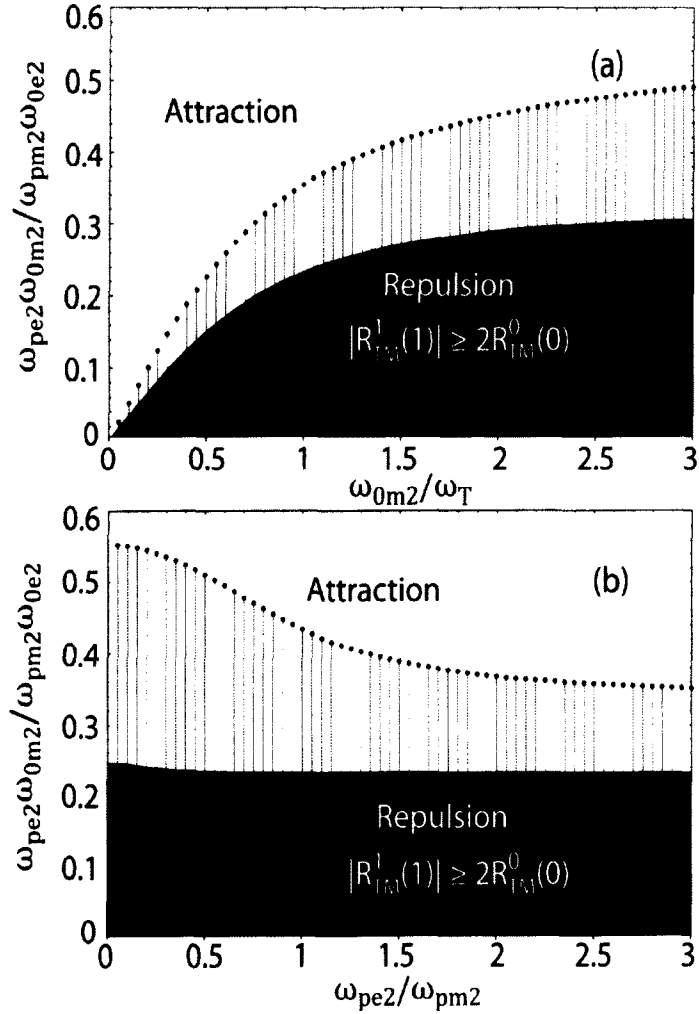


Figure 4.6: A comparison between the repulsive Casimir force domains calculated based on the sufficient condition of Equation 4.17 (blue domain) and through exact numerical integration of Equation 2.20 (dots). In the calculations we vary the compound parameters and have fixed (a) $\omega_{pe2}/\omega_{pm2} = 0.9$ and $\omega_{pm2}/\omega_{0m2} = 0.5$, and (b) $\omega_{0m2}/\omega_T = 0.5$ and $\omega_{pe2}/\omega_{pm2} = 0.1$. In all cases, we have set plate 1's permittivity as $\epsilon_1 = 2$.

We must note that in general the requirement $\omega_{pm2} > \omega_{pe2}$ is difficult to achieve in practice and the Casimir force reversal is highly unlikely to be accomplished at ambient conditions ($\omega_T = 0.163$ eV at 300 K) and matched metamaterial designs based on split ring resonators operating at the microwave or far infrared frequencies. An alternative approach will be to use metamaterial plates with magnetic and dielectric resonance frequencies that are highly dissimilar. For instance, if $\omega_{oe2} = 10\omega_{om2}$, the repulsion may be achieved for $\omega_{pm2}/\omega_{pe2} \geq 1/5$ [see Figure 4.6 (a) for $\omega_{om2} = 3\omega_T$]. However, in this case the strict applicability condition $R_{TM}^n(1) = R_{TE}^n(1) < 0$ for the bound in Equation 4.12 is no longer valid, and one must be careful when using the sufficient condition of Equation 4.17. In any case, the derived constrains shows that the Casimir force repulsion is, in principle, possible for a broader range of the plates' magneto-dielectric properties far beyond the much restrictive condition due to Boyer [43].

In this chapter, we have studied the problem of quantum levitation in parallel magneto-dielectric plate configuration. We have shown that when both plates are dissipative and one of the plates is non-magnetic, the Casimir force is always attractive for large and small plate separations. In the case of dispersive plate 2, described by the Lorentz oscillator model, we have obtained an explicit upper bound of the force and derived a simple sufficient condition for Casimir force repulsion. Based on the derived sufficient condition and the direct numerical calculations, we have shown that Casimir repulsion can be achieved for a broad range of optical parameters defining the magneto-dielectric plates, dramatically reducing the constrains imposed by the well-known Boyer's condition [43].

Most importantly, our approach of obtaining the upper bound for the Casimir force and from there a sufficient condition for Casimir force reversal can be rather helpful in

designing quantum levitation systems. This method could also be applied for any system provided the model for the permittivities and the permeabilities of the plates are known. When the sufficient condition is derived for the considered system with our approach, we explicitly obtain the limits on the material properties required for repulsion. For instance, consider a system with SiC as plate 1 and plate 2 is made of nickel polystyrene nanocomposites [32, 88] (mainly magnetic) that involves parameters like filling fraction of nickel, polystyrene and air. By obtaining the sufficient condition for this particular system, we get the bounds for the filling fraction of the materials involved and other associated materials' parameters. This would in principle allow us to realize the large variety of Casimir force based levitating MEMS devices. Therefore, our approach eliminates the tedious method of random numerical searches involving a large number of free optical parameters of the plates' required identifying domains where repulsive Casimir force may exist.

Overall, in this chapter the sufficient condition derived for Casimir force reversal provides important insights into the problem and can serve as a highly useful tool in future designs of levitating magneto-dielectric systems.

CHAPTER 5

CASIMIR FORCE BETWEEN A DIELECTRIC PLATE AND A METAMATERIAL PLATE

5.1 Introduction

Although some MEMS or NEMS devices can be made from nondispersive or weakly dispersive dielectric materials, there are many nanoscale devices that involve strongly dispersive materials (for instance having metal components). Hence, in this chapter, we consider a general system with two dispersive plates and air/vacuum as the intermediate medium. The systems that fall under this category are assumed to have (i) resonance frequencies close to the first few Matsubara frequencies, which mainly determines the nature of the force, and/or (ii) magnetic and dielectric resonance frequencies that are approximately the same. In addition to resolving the stiction effect in nanoscale devices, by considering the general case of two dispersive plates, we could design a quantum levitation system that has a wide range of applications. These include frictionless transportation, ultra clean rooms where metamaterial coating is used to repel the dust particles from the equipment surfaces, etc.

To reduce the complexity of the system and ease of the analysis, we consider plate 1 to be non-magnetic and the metamaterial plate 2 with values for permittivity and permeability satisfying the necessary condition $\mu_2 > \epsilon_2$. Again, the optical response of the plates is modeled using the Lorentz oscillator model (refer to Equations 4.1 and 4.2) and

the dissipation is assumed to be negligible compared to the corresponding resonant frequencies ($\omega_{0e,l} \gg \gamma_{e,l}$ and $\omega_{0m,l} \gg \gamma_{m,l}$).

5.2 Critical Mode Number for Casimir Force Repulsion

In Chapters 3 and 4, we showed that for a parallel-plate configuration consisting of two dissimilar plates described by the Lorentz oscillator model [16, 89], a repulsive Casimir force may only exist if the following condition is satisfied for at least one Matsubara frequency,

$$[z_1(i\omega_n) - 1][z_2(i\omega_n) - 1] < 0, \quad \text{Eq. 5.1}$$

where $z_l = \sqrt{\mu_l/\epsilon_l}$ are the plates' impedances. This is a necessary condition and indicates that force reversal may only occur if one of the plates is predominantly dielectric while the other is predominantly magnetic within a finite range of frequencies. The validity of the necessary condition can be assessed by inspecting the signature of the integrand in the Casimir force in Equation 2.35, which itself is determined by the signature of the sum of the specular functions. The specular functions vary from $R_p^n(0) \geq 0$ (non-retarded limit) to $R_p^n(1) = [z_1(i\omega_n) - 1][z_2(i\omega_n) - 1]/\{[z_1(i\omega_n) + 1][z_2(i\omega_n) + 1]\}$ (thermal-resonance limit). Then, pertaining to the optical properties of the plates, the force can be either positive (attractive) or negative (repulsive), provided the necessary condition is satisfied [$R_p^n(1) < 0$]. In the opposite case where the necessary condition is not satisfied or $R_p^n(1) > 0$, it can be shown by parametric swipe that the sum of the specular functions and concurrently the integrand in Equation 2.35 is positive regardless of the wave vectors or mode numbers.

However, it may not be possible to reverse the force by satisfying the necessary condition for a single vacuum mode, and on the opposite limit, it is not physically possible to satisfy the condition for all modes since all materials, including man-made, are nonmagnetic at high frequencies. Therefore, we need to identify the minimum number of modes or critical mode number n_c for which the necessary condition can be satisfied. In Figure 5.1, we depict the parametric regions where the necessary condition is satisfied. In the figure, for simplicity, we use a nonmagnetic plate 1 with frequency independent permittivity $\epsilon_1 = 2$ while the optical parameters of plate 2 are varied. The entire parametric domain is split into three subdomains, depending on a critical cutoff mode number $n_c = (1/\omega_T)[(\omega_{pe,2}^2\omega_{om,2}^2 - \omega_{pm,2}^2\omega_{oe,2}^2)/(\omega_{pm,2}^2 - \omega_{pe,2}^2)]^{1/2}$.

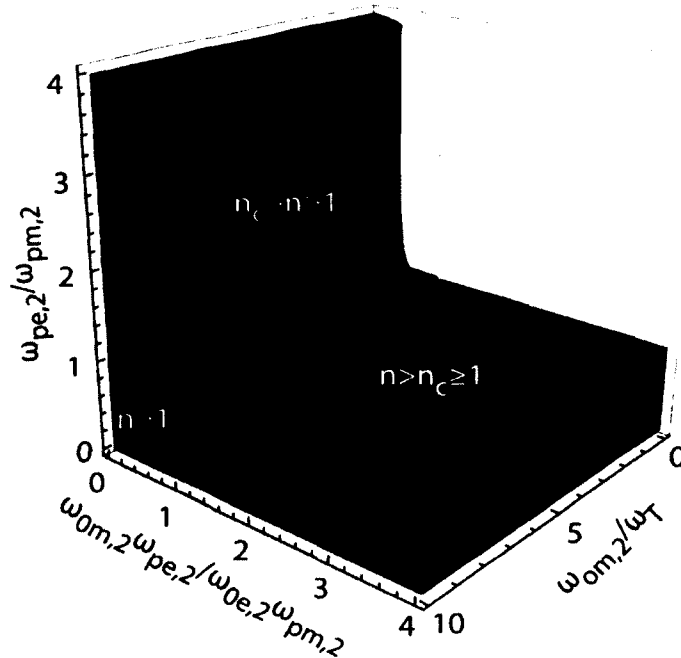


Figure 5.1: Parametric plot depicting the necessary condition in Equation 5.1 satisfied for different mode numbers as categorized based on the critical mode number n_c .

For the system under consideration where one of the plates (plate 1) is nonmagnetic, the necessary condition reduces to $z_2(i\omega_n) > 1$ and depends on three compound

parameters involving the resonance and plasma frequencies of the magneto-dielectric plate (plate 2). Three distinct parametric subdomains are observed such that the necessary condition is satisfied for (i) all modes (red domain), or for modes with (ii) $1 \leq n < n_c$ (blue domain) or (iii) $n > n_c \geq 1$ (green domain), where $n_c \geq 1$ is a critical mode number that depends on plate 2's magnetic and dielectric properties as well as the temperature. The first two subdomains [(i) red domain & (ii) blue domain in Figure 5.1] define the plates' parametric space most favorable for manifestation of repulsive Casimir force while in the third case [(iii) green domain in Figure 5.1] repulsion may only be achieved for low temperatures where the contribution of the higher order modes becomes significant. Furthermore, we observe that magneto-dielectric plates with $\omega_{pe,2} > \omega_{pm,2}$ and $\omega_{pe,2}/\omega_{0e,2} > \omega_{pm,2}/\omega_{0m,2}$ will always lead to attractive forces and the parametric domain where the force may turn repulsive increases for decreasing temperatures (lower thermal frequencies ω_T).

While the condition in Equation 5.1 provides a general guidance with respect to the plates' optical properties, it does not guarantee Casimir force reversal. Stricter constraints on the parametric domain that assure repulsion follows.

5.3 Upper Bound for the Casimir Force

As the Casimir force is rather difficult to solve analytically, similar to the previous case studied in Chapter 4, we seek an analytical upper bound for the force which can be solved analytically. As mentioned previously, to simplify the analysis, we consider plate 1 to be nonmagnetic and plate 2 is a magneto-dielectric such that the necessary condition in Equation 5.1 is satisfied for at least one mode. Then the specular functions are monotonically decreasing and confined within the strict limits of $R_p^n(1) \leq R_p^n(q) \leq$

$R_p^n(0)$, where $R_{TM}^n(1) = R_{TE}^n(1) < 0$, $R_{TM}^n(0) \geq 0$ and $R_{TE}^n(0) = 0$ (as plate 1 is nonmagnetic).

The specular functions have single or no real roots within the reciprocal wave vector range $0 \leq q \leq 1$ and the following upper bound of the integrant in Equation 2.35 is valid:

$$\begin{aligned} \text{Li}_0 \left[R_p^n(q) e^{-\frac{ns}{q}} \right] \\ \leq (1 - q^2) \text{Li}_0 \left[R_p^n(0) e^{-\frac{ns}{q}} \right] \\ + q^2 \text{Li}_0 \left[R_p^n(1) e^{-\frac{ns}{q}} \right]. \end{aligned} \quad \text{Eq. 5.2}$$

The parametric domains that identify the conditions for the validity of the upper bounds in Equation 5.2 are shown in Figure 5.2. It is clear that the specular function may only be negative provided $z_2 > 1$ or $[(z_1 - 1)(z_2 - 1) < 0]$ and bounds hold for all physical parameters and for both the TM and TE modes.

Integration of the Casimir force in Equation 2.35 represented by its upper bound in Equation 5.2 immediately follows:

$$\begin{aligned} F \leq F_\infty + \frac{k_B T}{4\pi d^3} \sum_p \sum_{n=1}^{\infty} \left(\text{Li}_3 \left[R_p^n(0) e^{-ns} \right] \right. \\ \left. + ns \text{Li}_2 \left[R_p^n(0) e^{-ns} \right] \right. \\ \left. + \frac{(ns)^2}{2} \text{Li}_1 \left[R_p^n(1) e^{-ns} \right] \right). \end{aligned} \quad \text{Eq. 5.3}$$

The first two terms in the sum are positive [$R_p^n(0) \geq 0$] and repulsive Casimir force may only appear, without being guaranteed, if the necessary condition $R_p^n(1) < 0$ is satisfied.

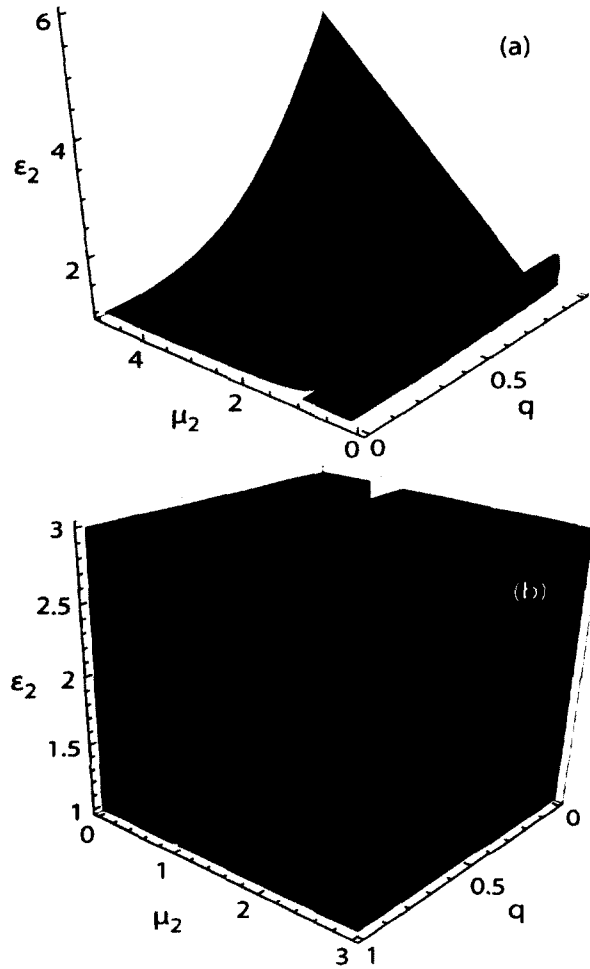


Figure 5.2: Parametric domains corresponding to the cases where the bounds in Equation 5.2 are not satisfied (red) and $\text{Li}_0[R_p^n(q)e^{-ns/q}] < 0$ (blue). (a) *TM* and (b) *TE* polarizations are studied separately and in the calculation we use $\epsilon_1 = 2$.

We note that Equation 5.3 correctly reproduces both the short distance ($s \rightarrow 0$) and large distance ($s \rightarrow \infty$) asymptotic limits as per Equations 2.44 and 2.37, respectively. Equation 5.3 shows that when the force is repulsive for $n = 1$ for fixed plate separation distance s , the force for higher order modes is also repulsive with a decrease in magnitude. Hence, we consider only the $n = 1$ term, underestimating the repulsive force, for obtaining sufficient condition.

Finally, using the properties of the polylogarithmic function $\text{Li}_\nu[R_p^n(0)e^{-ns}] \leq \text{Li}_\nu[R_p^n(0)]e^{-ns} \leq \text{Li}_\nu[R_p^n(0)]e^{-s}$ and $R_{TM}^0(0) \geq R_{TM}^1(0)$, by underestimating the repulsive term and overestimating the attractive term, we further simplify the force as,

$$\begin{aligned} \frac{8\pi d^3 F}{k_B T} &\leq \text{Li}_3[R_{TM}^0(0)] \\ &+ 2e^{-s}\{\text{Li}_3[R_{TM}^0(0)] + s \text{Li}_2[R_{TM}^0(0)] \\ &+ s^2 \text{Li}_1[R_{TM}^1(1)]\}. \end{aligned} \quad \text{Eq. 5.4}$$

Again by using the properties of the polylogarithmic function that $\text{Li}_3[R_p^n(x)] \leq \text{Li}_2[R_p^n(x)] \leq \text{Li}_1[R_p^n(x)]$ for $1 \geq R_p^n(x) \geq -1$, and by underestimating the repulsive term and overestimating the attractive term, we get

$$\begin{aligned} \frac{8\pi d^3 F}{k_B T} &\leq \text{Li}_1[R_{TM}^0(0)] \\ &+ 2e^{-s}\{(1+s) \text{Li}_1[R_{TM}^0(0)] \\ &+ s^2 \text{Li}_1[R_{TM}^1(1)]\}. \end{aligned} \quad \text{Eq. 5.5}$$

The Casimir force calculated through direct numerical integration of Equation 2.35, its upper bound Equation 5.3 and the approximation with $n = 1$ for the summation of Equation 5.5 are depicted in Figure 5.3. We consider a plate's configurations with $\omega_{pm,2}\omega_{0e,2} > \omega_{pe,2}\omega_{0m,2}$ and $\omega_{pm,2} > \omega_{pe,2}$, or both necessary and the sufficient conditions are concurrently satisfied. In Figure 5.3 we show the effect of change in temperature in the force and the bounds. As it is clearly shown, the upper bound Equation 5.3 follows the actual Casimir force and exactly recovers the force for small and large separation distances. In the case of the approximation with $n = 1$ for the summation of Equation 5.5, the force is recovered for large separation distances or high temperatures (as only $n = 0$ mode is required) and as expected the force for small separation distances is

not recovered as a large number of modes has to be included in the summation. However, it follows the Casimir force and its upper bound (Equation 5.3) for intermediate separation distances or near force minima $s \approx 2$. This allows us to investigate for the separation distance corresponding to the force minima and sufficient condition.

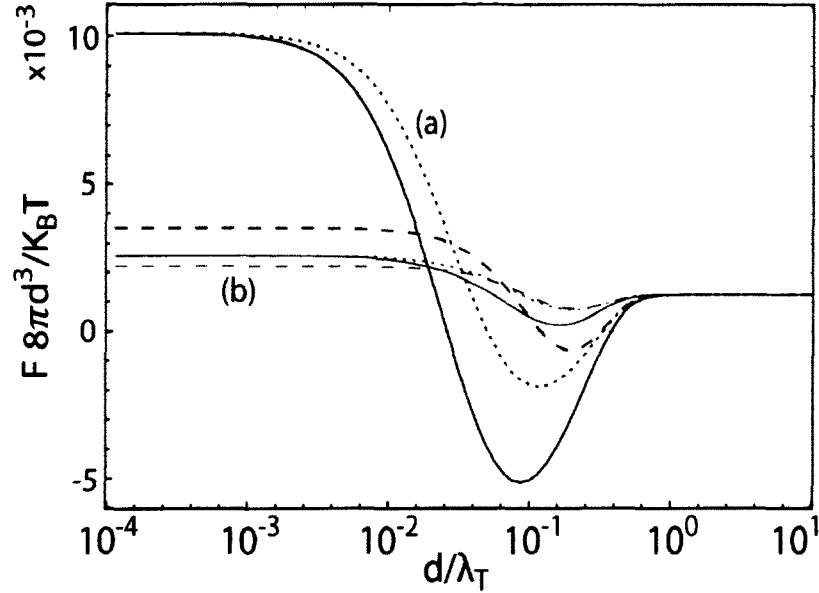


Figure 5.3: Casimir force calculated numerically based on Equation 2.35 (solid lines), the upper bound Equation 5.3 (dotted lines), and the approximated result Equation 5.5 (dashed lines). In the calculations we use $\omega_{pe,1} = 0.5\omega_{0e,1}$ for the nonmagnetic plate 1 while the optical parameters of the plate 2 are set as (a) $\omega_{0m,2} = 4\omega_T$ and (b) $\omega_{0m,2} = 1.01\omega_T$ with $\omega_{0m,2} = 0.6\omega_{0e,2}$, $\omega_{pm,2} = \omega_{0m,2}$ and $\omega_{pe,2} = 0.5\omega_{pm,2}$.

Figure 5.3 illustrates the Casimir force for the system at low temperatures with $\omega_{0m,2} = 4\omega_T$ [Figure 5.4 (a)] and high temperatures with $\omega_{0m,2} = 1.01\omega_T$ [Figure 5.4 (b)]. The parameters used in the calculations have been chosen such that the necessary condition (Equation 5.1) is satisfied for all modes. It is clear that for the same plate configuration with a decrease in temperature, the width of the repulsive window widens or the range of separation distance for which the repulsive force is achieved increases. It is

important to note that the force for large separation distance remains unchanged, whereas for small separation distances, the attractive force increases with decrease in temperature.

Figure 5.4 shows the Casimir force for a different system chosen such that it does not satisfy the necessary condition Equation 5.1.

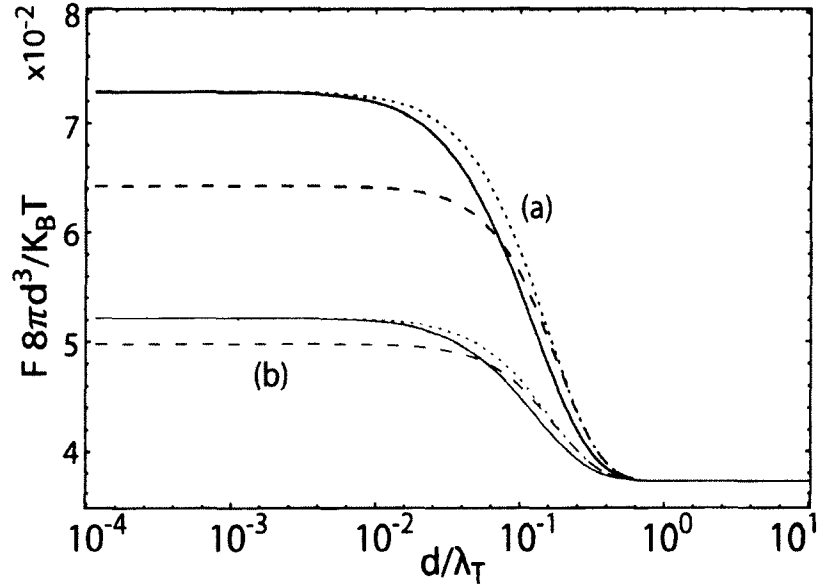


Figure 5.4: Casimir force calculated based on Equation 2.35 (solid lines), the upper bound of the Casimir force Equation 5.3 (dotted lines) and the approximation Equation 5.5 (dashed lines). In the calculations we use $\omega_{pe,1} = 0.5\omega_{0e,1}$ for the nonmagnetic plate 1 while the optical parameters of the plate 2 are set as (a) $\omega_{0m,2} = 1.5\omega_T$ and (b) $\omega_{0m,2} = 1.01\omega_T$ with $\omega_{0e,2} = 0.55\omega_{0m,2}$, $\omega_{0m,2} = 2.2\omega_{pm,2}$, and $\omega_{pe,2} = 1.1\omega_{pm,2}$.

Here, as expected the force is attractive and decreases with increase in temperature.

From Figures 5.3 and 5.4, it is clear that low temperatures are preferable for quantum levitating systems.

5.4 Sufficient Condition for Repulsive Casimir Force

The objective here is to determine a sufficient condition in terms of the material properties of the plates and temperature. We proceed by considering the minima of the upper bound in Equation 5.5, which is

$$s_{min} = 2 - \frac{\text{Li}_1[R_{TM}^0(0)]}{\text{Li}_1[R_{TM}^1(1)]}. \quad \text{Eq. 5.6}$$

It is important to note that $s_{min} \geq 2$ since $R_{TM}^1(1) < 0$ and $R_{TM}^0(0) > 0$, provided the force is repulsive. Substitute s_{min} in Equation 5.5 and we obtain,

$$\left. \frac{8\pi d^3 F}{k_B T} \right|_{min} \leq \text{Li}_1[R_{TM}^0(0)] \left[1 + 2e^{-2+\delta} \left(\frac{4}{\delta} - 1 \right) \right] \quad \text{Eq. 5.7}$$

where $\delta = \text{Li}_1[R_{TM}^0(0)]/\text{Li}_1[R_{TM}^1(1)]$. From Equation 5.7 we can obtain the limits of δ , and thus the sufficient condition for the force reversal.

Sufficient condition: For a parallel plate configuration where one of the plates is non-magnetic (plate 1) and the second plate (plate 2) is a magneto-dielectric, the repulsive Casimir force is manifested for a finite range of plate separations provided,

$$0 > \frac{\text{Li}_1[R_{TM}^0(0)]}{\text{Li}_1[R_{TM}^1(1)]} > -0.654658. \quad \text{Eq. 5.8}$$

Figure 5.5 shows the parametric domain representing the sufficient condition in terms of the specular functions $R_{TM}^0(0)$ and $R_{TM}^1(1)$. The plot range in Figure 5.5 is chosen such that the necessary condition is also satisfied $-1 \leq R_{TM}^1(1) \leq 0$ and $1 \geq R_{TM}^0(0) \geq 0$. When a system is designed such that its specular functions falls within the parametric domain depicted in Figure 5.5, it is guaranteed to have a repulsive Casimir force for a finite range of plate separations.

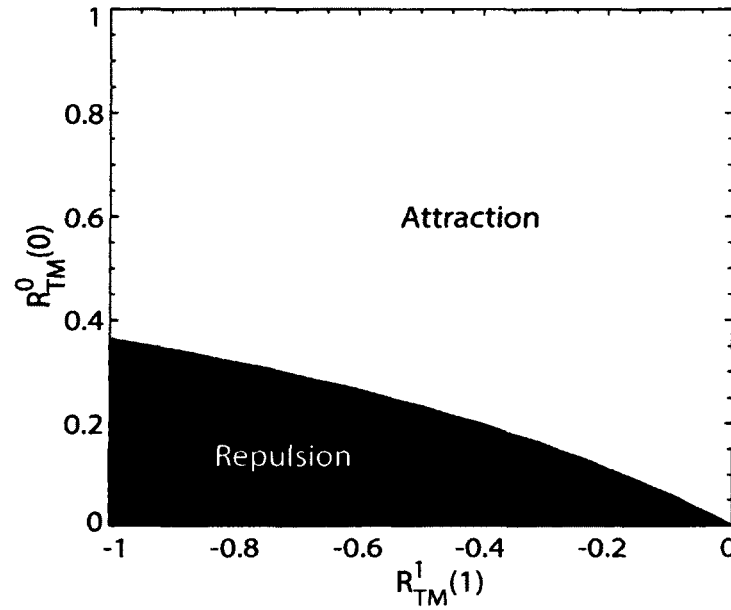


Figure 5.5: Parametric domain depicting the sufficient condition for Casimir force repulsion.

In Figure 5.6, we compare the parametric domains associated with the repulsive Casimir force calculated using the necessary and sufficient conditions and through exact numerical calculations of the force given by Equation 2.35. The yellow domain represents the sufficient condition and the region below the white dotted line represents the exact repulsive domain obtained numerically. It is apparent that by designing a system with plates whose material parameters fall in the yellow domain, we are assured to have a reversal of the Casimir force; hence, the sufficient conditions hold.

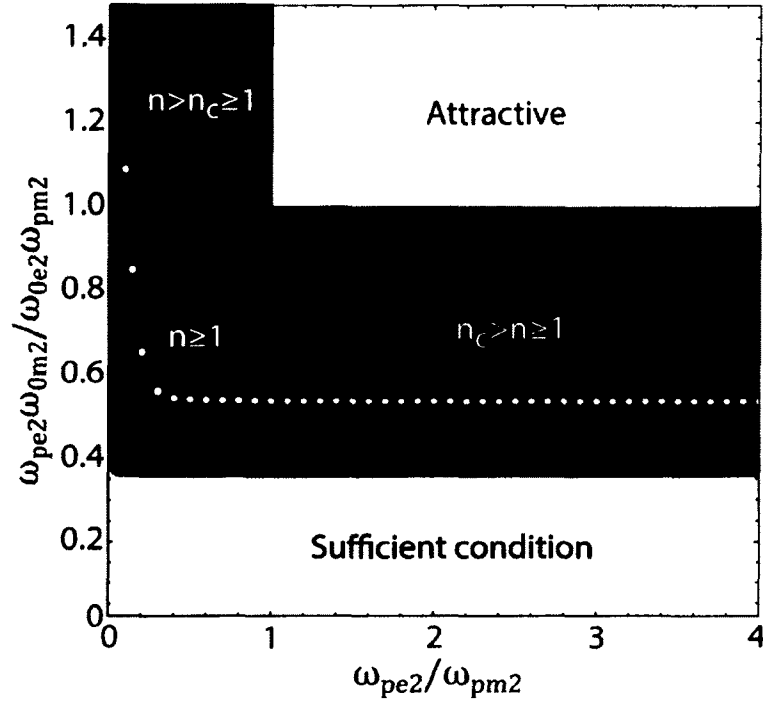


Figure 5.6: Parametric domains corresponding to various conditions for the realization of quantum levitation. The yellow domain corresponds to the sufficient condition given by Equation 5.8, red domain corresponds to the case where the necessary condition is satisfied for all modes $n \geq 1$, the blue domain corresponds to the case where the necessary condition is satisfied for modes less than the critical ($1 \leq n \leq n_c$), and the green domain corresponds to the case where the necessary condition is satisfied for modes greater than the critical ($n > n_c \geq 1$). The white dots represent the actual limit obtained through direct numerical calculations of the Casimir force using Equation 2.35 (the area below the dotted line).

It is important to note that the parametric domain defined by the sufficient condition in Equation 5.8 falls within the regions where the necessary condition is satisfied either for all the modes (red domain) or for modes that are less than the critical mode ($1 \leq n \leq n_c$) (blue domain). The green domain in Figure 5.1, for which the necessary condition is satisfied for higher order modes only ($n > n_c \geq 1$), is not included in Figure 5.6 as this domain does not overlap with the domain where the sufficient condition is satisfied. This again indicates that it is highly difficult or nearly impossible to achieve

quantum levitation in systems with material properties that satisfies the necessary condition for $n > n_c \geq 1$.

In this chapter, we have studied the Casimir force between a dispersive magneto-dielectric plate and a dispersive dielectric plate. For this configuration, we have derived an explicit upper analytical bound of the Casimir force. Using this bound we have obtained a necessary and a sufficient condition for quantum levitation in terms of the specular functions of the plates at zero and thermal frequencies. The complete parametric domain corresponding to the Casimir force reversal have been investigated.

CHAPTER 6

ELECTROMAGNETIC METAMATERIALS

6.1 Introduction

Recently, a rapid progress in the field of electromagnetic metamaterials (EMM) allows have open the possibility to design materials with optical properties that are not observed in nature [47, 54, 55, 57–59, 71, 85, 90–96]. These artificial materials could be used to control the flow of electromagnetic waves. The EMMs are engineered to have unique optical properties, for instance, to demonstrate strong magnetism at optical frequencies [54, 73, 90]. In a way, the EMMs can be viewed as a composite material comprised of artificial atoms or molecules in the form of small metal-dielectric resonators that can have either magnetic or electric responses or both. The unique properties of EMMs have attracted researchers' attention in the fields of physics, optics, and engineering. The permittivity and permeability of the materials can be nanofabricated by incorporating resonant structures that are smaller in size compared to the incident wavelength, but much larger compared to the atomic length scale. One of the well-known designs for engineering such metamaterials is the use of metal wires [79] or split ring resonators (SRRs) [73] in a host medium.

The vast majority of naturally existing optical materials, such as air and glass, are characterized with positive electric permittivity. Noble metals and highly doped semiconductors can also exhibit negative values of the permittivity at frequencies below

the plasma frequency [70, 89]. However, no natural materials have yet been found with negative permeability in the optical range. Recently, the electromagnetic metamaterials (EMM) that mimic the atomic response of a conventional media through assembling large number of electromagnetic resonators have been proposed as a mean to design the electric permittivity and magnetic permeability at will.

Figure 6.1 shows a typical composite medium with a host medium with permittivity ϵ_1 and permeability μ_1 in which another material with permittivity ϵ_2 and permeability μ_2 of a specific structure like a sphere, a spheroidal, a cylindrical, etc. is imbedded. The entire medium with two or more material inclusions can act as a single material with effective optical properties (effective permittivity and effective permeability), provided the wavelength of the applied field λ is much larger than the size of the inclusions a ($\lambda \gg a$). This phenomenon is popularly known as homogenization of a media. The limit ($\lambda \gg a$) implies that no retardation plays a role on the local level [55, 97–99].

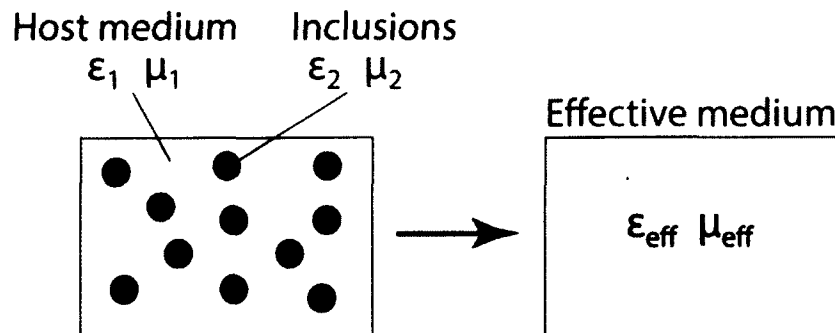


Figure 6.1: Illustration of a composite medium consisting of a host medium with ϵ_1 and μ_1 and inclusions with ϵ_2 and μ_2 .

Hence, by proper design of the inclusions, it is possible to tailor the optical response of the composite media and thus create new exotic electromagnetic materials. A particular

type of composite media for which both the permittivity and permeability are negative is commonly referred to as left handed materials (LHM) [45, 54, 55, 71, 82]. The LHM have attracted strong interest due to the possibility of reversing many optical effects including reversal of the Doppler shift and Cherenkov radiation, demonstration of negative refraction, and development of novel optical lenses that can image with resolution below the diffraction limit [55]. This dramatic progress in developing artificial electromagnetic material may provide the means to reverse the Casimir force.

Despite the dramatic increase in the parametric space, where Casimir force reversal can occur, the practical development of such levitating systems based on EMM plate remains highly challenging and requires the use of an engineering approach when designing the plates. Some particular systems that could be considered for achieving strong magnetic properties which is required for the force reversal are geometrically optimized SRR with resonance frequencies in the optical and near infrared frequency range [73], dielectric spheres [74], dielectric rectangular plates [75], or Bi-Helix structures [76] that increases the magnetic susceptibility of the composite medium. Another possible way is to use natural ferromagnetic materials and composites that have large magnetic susceptibility at low frequencies [77]. However, this approach should be considered with care since even though some ferrites have high permeability at low frequencies, the magnetic susceptibility is usually negligible when compared to the dielectric susceptibility of the ferrites at higher frequencies [77]. Probably the most promising strategy is to use structured composites where a ferromagnetic material is included within a low permittivity dielectric host [27, 30]. Few potentially promising candidates have recently been considered in the form of

nickel polystyrene nanocomposites and yttrium iron garnet (YIG) that exhibit high permeability and low permittivity [30, 32].

Therefore, to better understand the role of inclusions tailoring the permittivity and permeability of the material as a whole, we discuss in detail some of the important structures or composites such as SRR, parallel wires, and nickel polystyrene nanocomposites.

6.2 Split Ring Resonators

Split ring resonators (SRRs) are one of the most widely used structures that can provide strong magnetic response with negative permeability and thus are used to engineer NIM [45, 55, 73, 84]. If the magnetic field of the incident light is polarized perpendicular to the surface of the SRR, it generates an electromotive force and a magnetic dipole with orientation opposite to the incident field can be induced. Thus, the overall response of a composite made of SRR can manifest a negative permeability within a narrow frequency range close to the resonance. As we have demonstrated in the previous chapters, strong magnetic response is a prerequisite for any quantum levitation system with air/vacuum as the intermediate medium.

The effective permeability of the SRR is commonly modeled using Pendry's model (see Equation 4.5) [73]. Specifically, the effective permeability of such composite media will depend on the geometrical and physical characteristics of the SRRs. Though Pendry's model accurately describes the permeability of the SRR at low frequencies (compared to the width of the SRR), it is invalid at high frequencies as it provides unphysical values for permeability [$\mu(\omega \rightarrow \infty) < 1$]. Furthermore, as already discussed, Pendry's model does not satisfy causality (refer to Section 4.2). Hence, it is imperative to develop a new

analytical model for the permeability of the SRR that satisfies causality and is valid at all frequencies. This model would be highly useful for designing quantum levitation systems at the nanoscale.

In what follows, we develop an analytical model that is similar to Pendry's model but satisfying causality. This is achieved by the introduction of the radiation resistance which is absent in Pendry's model. The radiation resistance is the dominant at high frequencies and thus has important ramification for quantum levitating systems.

6.2.1 Analytical Model for Split Ring Resonator Including Radiation Resistance

6.2.1.1 RLC Model of a Split Ring Resonator

The SRR is analogous to a transmission line, with effective electrical components such as resistance due to losses in the metal, inductance due to circular flow of the current, and capacitance due to charge accumulation at the SRR termination points. The schematic of the active element (SRR) is shown in Figure 6.2. The width of the SRR is w and the mean radius is a , with outer and inner radii being $a + w$ and $a - w$, respectively. The height of the SRR is h and the split length is given in terms of split angle ($2\varphi_0$) as $d = a \sin[2\varphi_0] \approx 2a\varphi_0$. From Figure 6.2, $dx = a d\varphi$ where dx and $d\varphi$ are the length and azimuthal angles of an infinitesimally small segment of the split, respectively.

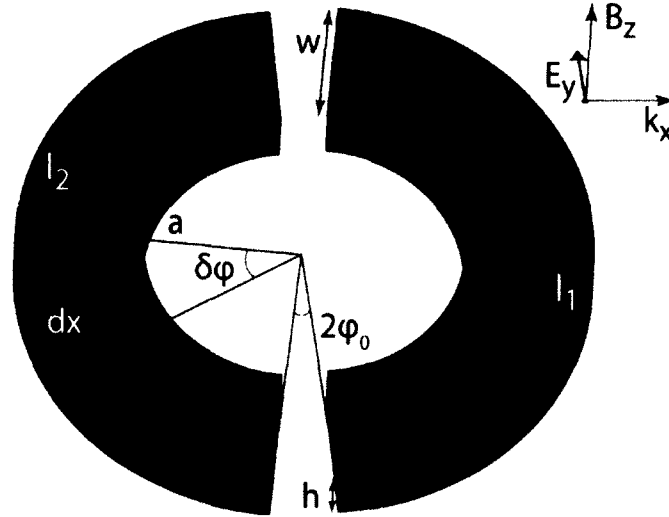


Figure 6.2: Illustration of the split ring resonator with the polarization and propagation direction of the incident electromagnetic wave indicated.

The SRR is illuminated with a transverse magnetic (TM) wave. According to Faraday's law of induction, the incident oscillating magnetic field (with frequency ω) induces an electromotive force (emf) which drives the current flow across the resonator. As mentioned, the SRR is analogous to a transmission line where a resistor R is connected to an inductor in the series with inductance L and the two splits in the SRR with a dielectric material act as two capacitors with capacitance C connected in the series with the equivalent capacitance $C_{eq} = C/2$.

To derive an analytical model for the permeability, we use Kirchhoff's voltage law involving the potential drop across each circuit element ($R, L, \& C_{eq}$),

$$u_B = I(t)R + L \frac{dI(t)}{dt} + \frac{1}{C_{eq}} \int I(t) dt. \quad \text{Eq. 6.1}$$

Assuming harmonic waves with the incident magnetic field $\vec{B}(t) = B_0 e^{-i\omega t} \hat{z}$ (assumed to propagate along the x -axis direction), we seek a solution for the current as $I(t) = I_0 e^{-i\omega t}$.

Using Faraday's law, the emf induced in the SRR is $u_B = -d\phi/dt = i\omega B_0 e^{-i\omega t}(\pi a^2)$, where ϕ is the magnetic flux. Substituting it back into Equation 6.1 we get,

$$i\omega B_0(\pi a^2) = I_0 R + L I_0(-i\omega) + \frac{I_0}{C_{eq}(-i\omega)}. \quad \text{Eq. 6.2}$$

From Equation 6.2 we determine the current I_0 in the SRR as,

$$I_0 = \frac{\pi B_0 \omega^2 a^2}{L(\omega_0^2 - \omega^2 - i\omega\omega_\tau)}, \quad \text{Eq. 6.3}$$

where $\omega_0 = 1/\sqrt{LC_{eq}}$ is the resonant frequency and $\omega_\tau = R/L$ is the relaxation frequency.

The magnetic dipole moment as,

$$\vec{m} = IA\hat{z} = \frac{\mu_0 \omega^2 (\pi a^2)^2}{L(\omega_0^2 - \omega^2 - i\omega\omega_\tau)} \vec{H}, \quad \text{Eq. 6.4}$$

where $A = \pi a^2$ is the surface area of the SRR. The magnetization of a composite material made of SRR is then $\vec{M} = n\vec{m}$ where $n = 1/V$ is the number density of the resonators, and V is the volume of the unit cell. Identifying that $p = \pi a^2 h/V$ is the volume fraction of the SRR and $\chi_m = |\vec{M}|/|\vec{H}|$, we obtain the effective permeability of the composite,

$$\mu_{eff} = 1 + \chi_m = 1 + p \frac{\mu_0 \omega^2 \pi a^2}{Lh(\omega_0^2 - \omega^2 - i\omega\omega_\tau)}. \quad \text{Eq. 6.5}$$

Next, we determine the circuit components such as the internal resistance R_{in} , inductance L , and equivalent capacitance C_{eq} . The internal resistance R_{in} of the SRR is given as,

$$R_{in} = \rho \frac{l}{A'}, \quad \text{Eq. 6.6}$$

where $\rho = 1/\omega \varepsilon'' \varepsilon_0$ is the resistivity, $l = 2\pi a$ is the length, $A' = wh$ is the cross sectional area of the SRR, ε'' is the imaginary part of permittivity of the SRR, and ε_0 is the permittivity of free space. We adopt the Drude model for the SRR metal permittivity $\varepsilon =$

$\varepsilon' + i\varepsilon'' = \varepsilon_b - \omega_p^2/\omega(\omega + i\tau)$ where ε_b is the contribution due to inter-band transitions, ω_p is the plasma frequency of the metal, and τ is the relaxation frequency of the metal. The internal resistance then follows from Equation 6.6 as,

$$R_{in} = \frac{2\pi a \omega^2 + \tau^2}{w \tau \omega_p^2 \varepsilon_0 h} = \beta(\omega^2 + \tau^2). \quad \text{Eq. 6.7}$$

The inductance of the SRR can be determined from the magnetic flux inside the ring ϕ_I and the flux in the region enclosed by the ring ϕ_{II} . The inductance of the SRR is given as $L = \phi/I$ where $\phi = \phi_I + \phi_{II}$ is the total flux. Using Ampere's law, the fluxes ϕ_I and ϕ_{II} are determined to be,

$$\phi_I = \frac{\pi\mu_0 I}{6h} w(6a - w), \quad \text{Eq. 6.8}$$

$$\phi_{II} = \frac{2\pi a}{kh} \mu_0 I J_1(ka). \quad \text{Eq. 6.9}$$

where $J_1(ka)$ is the Bessel's function of first kind. From Equations. 6.8 and 6.9, the inductance of the SRR can be written as,

$$L = \frac{\pi\mu_0}{h} \left[\frac{2a}{k} J_1(ka) + \frac{w}{6} (6a - w) \right], \quad \text{Eq. 6.10}$$

and in the large wavelength limit $ka \ll 1$ (or quasi-static limit), the inductance simplifies to,

$$L = \frac{\pi\mu_0}{h} \left[a^2 + wa - \frac{w^2}{6} \right]. \quad \text{Eq. 6.11}$$

Again, when $w \ll a$, the inductance becomes $L = \pi\mu_0 a^2/h$.

The capacitance of the SRR is determined using the relation, $C = \varepsilon_0 \varepsilon_r A'/d$ where $A' = wh$ and the split in the ring is $d = a \sin 2\varphi_0$. Then the equivalent capacitance

using $C_{eq} = C/2$. Using the parameters of the SRR the equivalent capacitance is written as,

$$C_{eq} = \epsilon_0 \epsilon_r \frac{wh}{2a \sin 2\varphi_0} \approx \epsilon_0 \epsilon_r \frac{wh}{4a\varphi_0} \quad (\sin 2\varphi_0 \ll 1). \quad \text{Eq. 6.12}$$

Hence, we have determined all the necessary electrical parameters related to the SRR. By substituting the resistance R (Equation 6.7), inductance L (Equation 6.11), and capacitance C_{eq} (Equation 6.12) in the effective permeability Equation 6.5 we get,

$$\mu_{eff} = 1 + \frac{f\omega^2}{\omega_0^2 - \omega^2 - i\omega\omega_\tau(\omega)}, \quad \text{Eq. 6.13}$$

where $f = pa^2/(a^2 + wa - w^2/6)$ is the effective filling fraction of the SRR and when the width is much smaller than the radius of the SRR $w \ll a$, $f \rightarrow p$. Hence, we obtained an analytical model for the SRR in terms of its circuit components.

When we compare our analytical model for the effective permeability of a composite made of SRR (Equation 6.13) to Pendry's model (Equations 4.5 and 4.6), we observe that the relaxation frequency ω_τ is no longer constant but is proportional to ω^2 for high frequencies. Considering the asymptotic behavior for high frequencies, we obtain $\lim_{\omega \rightarrow \infty} (\mu'_{eff} - 1) = 1/\omega^2$, satisfying the $1/\omega^2$ asymptotic required by causality. Similarly, for the imaginary part, we get $\lim_{\omega \rightarrow \infty} \mu''_{eff} \propto 1/\omega$, which violates the $1/\omega^3$ asymptotic required by the Kramers-Kronig relations [86]. While our model is an improvement compared to Pendry's model, it needs to be modified further if it is to be entirely consistent with causality. Additionally, at a high frequency, it is important to include the effects of radiation which will affect the effective resistance of the SRR.

6.2.1.2 Radiation Resistance of the SRR

The radiation resistance is related to the energy losses in the form of a radiating EM field. According to classical electrodynamics, as the electrons (charged particles) are accelerated, they radiate EM waves which results in added losses [86]. The radiation resistance of a circuit element is usually negligible at low frequencies; however, it can be the dominant dissipation process at high frequencies as we will show in this section.

First, we modify the RLC model to include higher order resonance modes that play a major role at high frequencies. The telegraph equation [100] associated with the SRR is given as,

$$\delta u = -IR \delta x - L \delta x \frac{dI}{dt} + \delta u_B, \quad \text{Eq. 6.14}$$

where R is the resistance per unit length, L is the inductance per unit length, I is the current, and u_B is the emf induced across the SRR due to the incident magnetic field $\vec{B}(x, t)$. Including the associated parameters and rewriting Equation 6.14 in terms of the azimuthal differential angle, we get

$$\delta u = -IRa \delta \varphi - La \delta \varphi \frac{dI}{dt} + \delta u_B. \quad \text{Eq. 6.15}$$

The magnetic flux (ϕ) and the corresponding induced emf (δu_B) are given as,

$$\begin{aligned} \phi &= \int \vec{B} \cdot d\vec{S} = 2 \int_{-a}^a dx \int_0^{\sqrt{a^2-x^2}} B(x, t) dy \\ &= 2\pi a^2 \frac{J_1(ka)}{ka} B(t), \end{aligned} \quad \text{Eq. 6.16}$$

$$\delta u_B = -\frac{d\phi}{dt} = i\omega B(t) J_1(ka) \frac{a}{k} \delta \varphi, \quad \text{Eq. 6.17}$$

where $k = \omega\sqrt{\epsilon_r}/c$ is the wave vector in the host medium, ω is the angular frequency of the incident wave, c is speed of light in the vacuum, and ϵ_r is the relative permittivity of the host medium.

Substituting the induced emf (Equation 6.17) in Equation 6.15, we write the telegraph equation as,

$$\frac{du}{d\varphi} = -IRa - La \frac{dI}{dt} + \frac{i\omega a}{k} J_1(ka) B(t). \quad \text{Eq. 6.18}$$

To relate Equation 6.18 to the capacitance of the SRR, we use the current conservation law $\int \frac{d\rho}{dt} + \int \vec{\nabla} \cdot \vec{J} dv = 0$ where ρ is the charge density and \vec{J} is the current density. Integrating over the split ring we obtain,

$$\frac{dI}{dx} = -C_{eq} \frac{du}{dt}, \quad \text{Eq. 6.19}$$

which can also be written in terms of the current and voltage across the infinitesimally small angular element $\delta\varphi$ as,

$$\frac{d^2I}{d\varphi^2} = -C_{eq} a \frac{d^2u}{d\varphi dt}, \quad \text{Eq. 6.20}$$

where C_{eq} is the equivalent capacitance per unit length.

Using Equations 6.18 and 6.20, we relate R, L and C_{eq} to the current I as,

$$\begin{aligned} \frac{d^2I}{d\varphi^2} &= -C_{eq} a \left[-Ra \frac{dI}{dt} - La \frac{d^2I}{dt^2} + \frac{i\omega a}{k} J_1(ka) \frac{dB(t)}{dt} \right] \\ &= -q^2 I - \gamma^2 B(t), \end{aligned} \quad \text{Eq. 6.21}$$

where $q^2 = \omega^2 a^2 L C_{eq} + i \omega a^2 R C_{eq}$ and $\gamma^2 = C_{eq} (\omega^2 a^2 / k) J_1(ka)$. Then by applying the current termination conditions $I_1(\varphi = -\varphi_0 + \pi/2) = I_1(\varphi = \varphi_0 - \pi/2) = 0$

and $I_2(\varphi = -\varphi_0 - \pi/2) = I_2(\varphi = \varphi_0 - 3\pi/2) = 0$ in Equation 6.21, we get the current in the first (I_1) and second (I_2) half rings of the SRR (see Figure 6.2) as,

$$I_1(\omega, \varphi) = I_1' + i I_1'' = B(t) \frac{\gamma^2}{q^2} \left\{ \frac{\cos(q\varphi)}{\cos\left[q\left(\frac{\pi}{2} - \varphi_0\right)\right]} - 1 \right\}, \quad \text{Eq. 6.22}$$

$$I_2(\omega, \varphi) = I_2' + i I_2'' = B(t) \frac{\gamma^2}{q^2} \left\{ \frac{\cos[q(\varphi + \pi)]}{\cos\left[q\left(\frac{\pi}{2} - \varphi_0\right)\right]} - 1 \right\}. \quad \text{Eq. 6.23}$$

From Equations 6.22 and 6.23, we obtain the resonant condition for the currents as,

$$q_r = \frac{\pi(n - 1/2)}{\frac{\pi}{2} - \varphi_0}, \quad \text{Eq. 6.24}$$

where n is the mode number. Using the resonant condition, we could design a SRR with R, L , and C_{eq} with resonances at given (preset) frequencies. The circulating current resonances will lead to a strong magnetic response of the SRR and thereby high μ_{eff} of the metamaterial.

Equations 6.22 and 6.23 show that the current I_1 reaches its peak value at $\varphi = 0$ and the current I_2 reaches its peak value at $\varphi = \pi$ which is given as,

$$I_{1,max}(\varphi = 0) = B(t) \frac{\gamma^2}{q^2} \left[\sec q \left(\frac{\pi}{2} - \varphi_0 \right) - 1 \right], \quad \text{Eq. 6.25}$$

$$I_{2,max}(\varphi = \pi) = B(t) \frac{\gamma^2}{q^2} \left[\cos(2\pi q) \sec q \left(\frac{\pi}{2} - \varphi_0 \right) - 1 \right], \quad \text{Eq. 6.26}$$

$$I_{2,max}(\varphi = \pi) = B(t) \frac{\gamma^2}{q^2} \left[\cos(2\pi q) \sec q \left(\frac{\pi}{2} - \varphi_0 \right) - 1 \right],$$

where $I_{1,max}(\varphi = 0) = I_{2,max}(\varphi = \pi) = I_0$. The current profiles are shown in Figure 6.3.

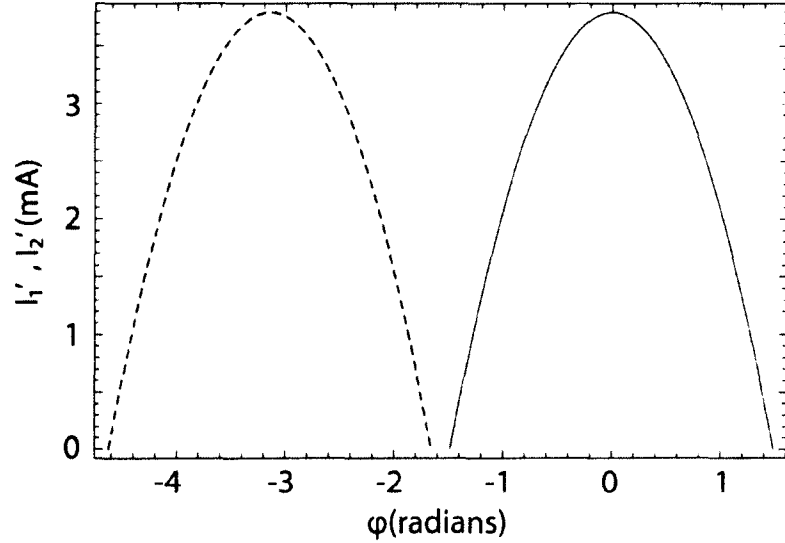


Figure 6.3: Plot of real part of the current I_1 (dashed blue) and I_2 (solid red) for $a = 20 \mu\text{m}$, $w = 1 \mu\text{m}$, $h = 1 \mu\text{m}$, $2\varphi_0 = 5^\circ$, $\lambda = 100a$, and $B_0 = 1$. The material considered for the SRR is gold with plasma frequency $\omega_p = 1.396 * 10^{16} \text{ rad/sec}$ and relaxation frequency $\gamma = 3.25 * 10^{13} \text{ rad/sec}$.

Now the radiation resistance can be determined using the currents I_1 and I_2 . To begin, we write the magnetic vector potential \vec{A} in terms of the current as follows:

$$\vec{A}(x) = \frac{\mu_0}{4\pi} \frac{e^{ikr}}{r} \int \vec{J}(x') d^3x', \quad \text{Eq. 6.27}$$

$$\vec{A}(x) = \frac{\mu_0 a}{\pi} \frac{e^{ikr}}{r} B(t) \frac{\gamma^2}{q^3} (q\varphi_r - \tan q\varphi_r). \quad \text{Eq. 6.28}$$

Then the vector potential for the radiation field in terms of magnetic dipole moment \vec{p} [86] is written as,

$$\vec{A}(x) = \frac{-i\omega\mu_0}{4\pi} \frac{e^{ikr}}{r} \vec{p}, \quad \text{Eq. 6.29}$$

and when compared with Equation 6.28 we identify the dipole moment as,

$$\vec{p} = \frac{i4a}{\omega} B(t) \frac{\gamma^2}{q^3} (q\varphi_r - \tan q\varphi_r). \quad \text{Eq. 6.30}$$

The power radiated by the SRR due to the flow of the current is related to the radiation resistance (R_{rad}) and the dipole moment \vec{p} as [86],

$$P = I_0^2 R_{rad} = \frac{c^2 Z_0 k^4}{12\pi} |\vec{p}|^2, \quad \text{Eq. 6.31}$$

where $Z_0 = \sqrt{\mu_0/\epsilon_0}$ is the impedance of the free space. Finally, from Equation 6.31 we obtain the radiation resistance of the SRR as,

$$R_{rad} = \frac{c^2 Z_0 k^4}{12\pi} \frac{|\vec{p}|^2}{|I_0|^2}. \quad \text{Eq. 6.32}$$

It is clear from Equations 6.30 and 6.32 that the radiation resistance depends on the resistance, the capacitance, and the inductance of the SRR. Therefore, by using Equations 6.7, 6.11, and 6.12 for R_{in} , C_{eq} and L , we write the radiation resistance as,

$$R_{rad} = \frac{c^2 Z_0 k^4}{3\pi} \frac{4a^2 \vartheta}{\varphi_r \omega^3 a^2 C_{eq} \sqrt{R^2 + L^2 \omega^2}}, \quad \text{Eq. 6.33}$$

where

$$\vartheta = \sum_{q=X,Y} \left\{ -\frac{\pi q}{2} + q\varphi_0 + \frac{\sin[q(\pi - 2\varphi_0)]}{\cos[X(\pi - 2\varphi_0)] + \cosh[Y(\pi - 2\varphi_0)]} \right\}^2,$$

$$\varphi_r = \frac{2(\cos[X(\pi/2 - \varphi_0)] - \cosh[Y(\pi/2 - \varphi_0)])^2}{\cos[X(\pi - 2\varphi_0)] + \cosh[Y(\pi - 2\varphi_0)]},$$

$$X = a \sqrt{\frac{C_{eq}\omega(L\omega + \sqrt{R^2 + L^2\omega^2})}{2}}, \text{ and } Y = \frac{Ra\sqrt{C_{eq}\omega}}{\sqrt{2L\omega + 2\sqrt{R^2 + L^2\omega^2}}}$$

To simplify the expression for the radiation resistance in Equation 6.33, we expand in power series about ka and consider the quasi-static limit ($ka \ll 1$). This is because, in principle, an effective permeability and/or permittivity can be assigned only for composite materials with inclusions having sizes that are much smaller than the wavelength $\lambda \gg a$. Only in this limit the material can be considered as a homogeneous material. When $\lambda \geq a$,

increased scattering and multi-pole interactions between adjacent SRRs in the medium need to be included in the calculation, which is out of scope of this work. After expansion in the series, we obtain a rather simplified form of the radiation resistance as,

$$R_{rad} = \frac{16Z_0\epsilon_r^2\omega^2 a^2 \left(\frac{\pi}{2} - \varphi_0\right)}{27\pi c^2} = \chi\omega^2. \quad \text{Eq. 6.34}$$

Figure 6.4 compares the internal resistance, radiation resistance, and the total resistance as a function of ka and for different split angles $2\varphi_0$. It is evident that for $ka \approx 0$ the radiation resistance is much smaller compared to the internal resistance and can be neglected from the calculations. However, with an increase in the frequency, the radiation resistance becomes dominant and for $ka \rightarrow 1$ the internal resistance becomes negligible and can be neglected. In addition, Figure 6.4 shows that the approximated radiation resistance in the limit of $ka \ll 1$ in Equation 6.34 is virtually the same as the actual radiation resistance due to Equation 6.33. Nevertheless, for extremely small values of the split angle $2\varphi_0$, the error between the approximated and the actual radiation resistance increases [see Figures 6.4 (a) and (b)].

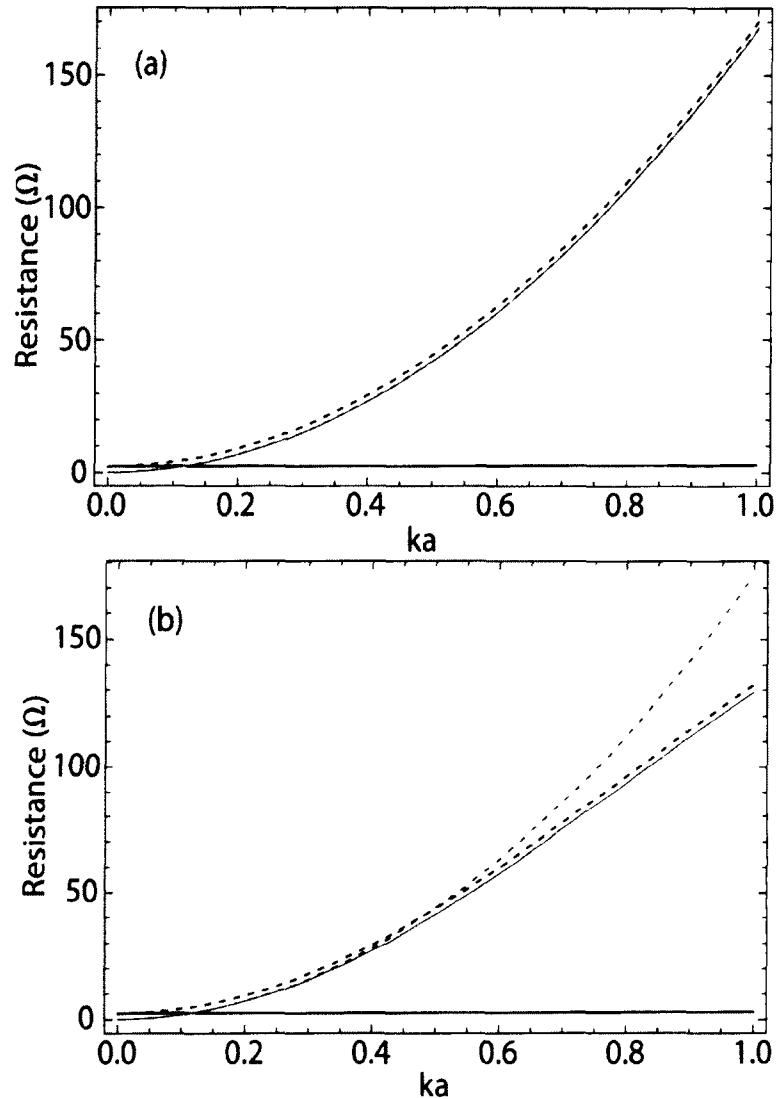


Figure 6.4: Plot of internal resistance (solid blue, Equation 6.7), exact radiation resistance (solid green, Equation 6.33), analytical radiation resistance (dashed red, Equation 6.34) and total resistance $R_{rad} + R_{in}$ (black dashed) for $a = 20 \mu m$, $w = 1 \mu m$, $h = 1 \mu m$, (a) $2\varphi_0 = 2^\circ$, and (b) $2\varphi_0 = 0.02^\circ$.

To further analyze the nature of the radiation resistance and the validity of our approximated result, in Figure 6.5 we plot the relative error between actual radiation resistance (Equation 6.33) and the approximated radiation resistance (Equation 6.34). We consider two parameters, the retardation factor ka and the width to radius ratio (w/a) of the SRR.

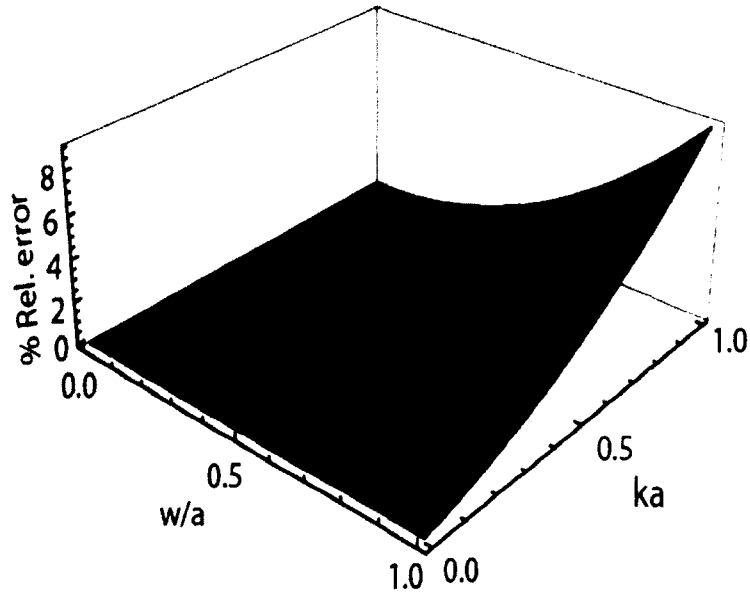


Figure 6.5: Percentage relative error between the actual radiation resistance (Equation 6.33) and the approximated radiation resistance (Equation 6.34) with $a = 20 \mu\text{m}$ and $2\varphi_0 = 2^\circ$ for different ka and w/a ratio.

The relative error between the actual and approximated radiation resistance increases with an increase in the SRR width to radius ratio w/a and incident frequency (ka) for fixed a . Even for the worst case of $w \rightarrow a$ and $ka \rightarrow 1$, the maximum possible error is approximately 8%, which suggests that the approximated radiation resistance can be used for $0 \leq ka \leq 1$ and any w/a provided that $2\varphi_0$ is not extremely small. It is important to note that the limit of $w \rightarrow a$ may not be considered as the structure will not be a SRR anymore, and it will become a system of two half spheres separated by $2\varphi_0$ measured from the center. To further analyze the validity of our approximation, we calculated the relative error as a function of the size parameter ka and split angle (see Figure 6.6).

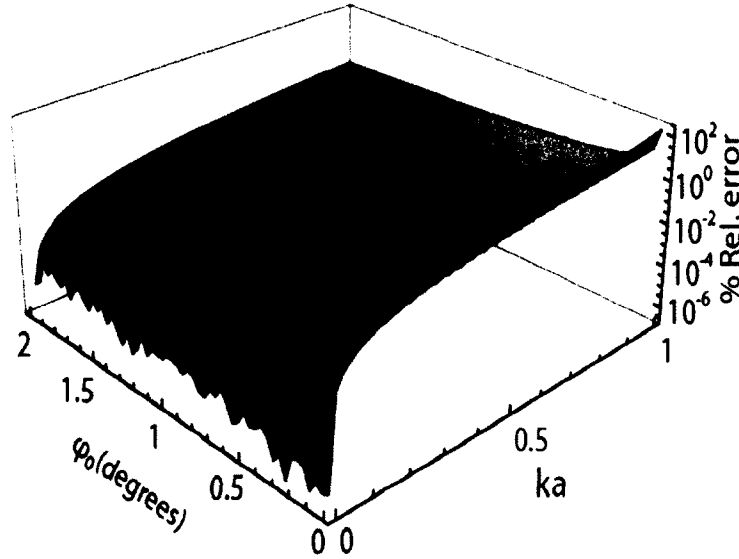


Figure 6.6: Percentage relative error between the actual radiation resistance (Equation 6.33) and the approximated radiation resistance (Equation 6.34) with $a = 20 \mu\text{m}$ for different ka and $2\varphi_0$.

Figure 6.6 shows that the relative error is extremely small in the limit of $ka \ll 1$; however, for extremely low value of $2\varphi_0$ the relative error increases with an increase in ka . Hence, from our analysis it is clear that the approximation holds for any w/a and $0 \leq ka \leq 1$ provided $\varphi_0 > 1^\circ$. This constraint is not an issue since it is practically difficult to fabricate SRR with such small split angles. In addition, the SRR is generally designed to achieve resonance at high frequencies whereas with $\varphi_0 \rightarrow 0$, the capacitance $C \rightarrow \infty$ and the resonance frequency becomes $\omega_0 \rightarrow 0$, which is the opposite of the design needs. Therefore, for all practical purposes, we can consider the approximation of Equation 6.34 to be highly accurate.

6.2.2 Analytical Model for Split Ring Resonator Satisfying Causality

In this section, we include the effects due to the radiation resistance on the effective permeability of the SRR based metamaterial composite which is thus given as,

$$\mu_{eff} = \mu'_{eff} + i\mu''_{eff} = 1 + \frac{f\omega^2}{\omega_0^2 - \omega^2 - i\omega\omega_\tau(\omega)}, \quad \text{Eq. 6.35}$$

where $\omega_\tau(\omega) = R/L$ is the relaxation frequency and $R = R_{in}(\omega) + R_{rad}(\omega)$ is the total resistance of the SRR. Using Equations 6.7 and 6.34, we can write the relaxation rate as $\omega_\tau(\omega) = [\beta\tau^2 + (\beta + \chi)\omega^2]/L = \omega_{\tau 0} + \alpha\omega^2$, where $\omega_{\tau 0} = \omega_\tau(0)$ is the relaxation frequency at zero frequency.

The real and imaginary part of the effective permeability can be explicitly written as,

$$\mu'_{eff} = 1 + \frac{f\omega^2(\omega_0^2 - \omega^2)}{(\omega_0^2 - \omega^2)^2 + \omega^2\omega_\tau^2(\omega)}, \quad \text{Eq. 6.36}$$

$$\mu''_{eff} = \frac{f\omega^3\omega_\tau(\omega)}{(\omega_0^2 - \omega^2)^2 + \omega^2\omega_\tau^2(\omega)}. \quad \text{Eq. 6.37}$$

Considering the asymptotic behavior for large frequencies, we obtain $\lim_{\omega \rightarrow \infty} \mu'_{eff} \propto 1/\omega^2$ (obeying the asymptotic required by the Kramers-Kronig relation) and $\lim_{\omega \rightarrow \infty} \mu''_{eff} \propto 1/\omega \neq 1/\omega^3$ (violating the asymptotic required by the Kramers-Kronig relation) [86]. Clearly, μ_{eff} in Equation 6.35 does not satisfy the causality and may not be used to define the permeability of a medium.

According to Kramers-Kronig relation, the real and imaginary parts of the permeability of a material are interrelated as [86],

$$\mu'(\omega) = 1 + \frac{2}{\pi} \mathbb{P} \int_0^\infty \frac{\omega' \mu''(\omega')}{\omega'^2 - \omega^2} d\omega', \quad \text{Eq. 6.38}$$

$$\mu''(\omega) = -\frac{2\omega}{\pi} \mathbb{P} \int_0^\infty \frac{\mu'(\omega') - 1}{\omega'^2 - \omega^2} d\omega', \quad \text{Eq. 6.39}$$

where $\mu'(\omega)$ and $\mu''(\omega)$ are the real and imaginary parts of the relative permeability of a medium and \mathbb{P} in the integral refers to the principal part (determined by using the Cauchy

principal value method). The Kramer-Kronig relation is derived based on the basic principle of nature that the effects follow the cause (causality) which any material should satisfy. If an analytical model is causal, we should be able to get the imaginary part from its real part and vice versa (using Equations 6.38 and 6.39).

The permeability model of Equation 6.35 is inconsistent with the Kramer-Kronig relations. The reason for this inconsistency is the incorrect high frequency asymptotic of μ''_{eff} . Therefore, we proceed to obtain the imaginary part of the permeability using the real part which we have already shown to have the proper asymptotic. By employing the Cauchy principal value method to perform the integration in Equation 6.39, we obtain,

$$\mu''_{eff} = \frac{2\omega}{\pi} \left| \int \frac{\mu'_{eff}(\omega') - 1}{\omega'^2 - \omega^2} d\omega' \right|_{\omega' \rightarrow 0} . \quad \text{Eq. 6.40}$$

A closed form solution of the above equation can be obtained as,

$$\mu''_{SRR} = \frac{-p\omega}{2\pi\{\omega_0^4 + \omega^2[\omega^2 - 2\omega_0^2 + (\omega_{\tau 0} + \alpha\omega^2)^2]\}} \quad \text{Eq. 6.41}$$

$$\sum_{i=1,2,3} \frac{\omega_0^4(R_i - \omega_0^2) + A_i\omega^2 - R_i\alpha^2\omega^4(R_i - \omega_0^2)}{\sqrt{R_i B_i} / [2 \text{Log}(-\sqrt{R_i}) - \text{Log}(R_i)]} ,$$

where

$$A_i = \omega_0^4 + \omega_0^2 R_i(R_i\alpha^2 + 2\omega_{\tau 0}\alpha - 1) + \omega_{\tau 0}^2 R_i,$$

$$B_i = (\omega_{\tau 0} + R_i\alpha)(\omega_{\tau 0} + 3R_i\alpha) + 2(R_i - \omega_0^2),$$

$$R_1 = \frac{-\{4 + 8\omega_{\tau 0}\alpha - [2^{7/3}(1 + 4\omega_{\tau 0}\alpha + \omega_{\tau 0}^2\alpha^2 + 6\alpha^2\omega_0^2)]\}}{12\alpha^2 m(1 + 2^{2/3})},$$

$$R_2 = \frac{-\{4 + 8\omega_{\tau 0}\alpha + [2^{4/3}(1 + i\sqrt{3})(1 + 4\omega_{\tau 0}\alpha + \omega_{\tau 0}^2\alpha^2 + 6\alpha^2\omega_0^2)]\}}{12\alpha^2 m[1 + 2^{2/3}(1 - i\sqrt{3})]},$$

$$m = (\beta + \sqrt{\zeta})^{1/3},$$

$$\beta = -2 - 15\omega_{\tau 0}^2 \alpha^2 + 2\omega_{\tau 0}^3 \alpha^3 - 18\alpha^2 \omega_0^2 - 27\alpha^4 \omega_0^4 - 12\omega_{\tau 0}(\alpha + 3\alpha^3 \omega_0^2),$$

$$\zeta = 27\alpha^4 (\omega_{\tau 0} + \alpha \omega_0^2)^2 (-\omega_{\tau 0}^2 - 4\omega_{\tau 0}^3 \alpha + 4\omega_0^2 + 18\omega_{\tau 0} \alpha \omega_0^2 + 27\alpha^2 \omega_0^4),$$

and R_3 is the complex conjugate of R_2 .

Figure 6.7 shows the real and imaginary parts of the analytical model (μ'_{SRR} and μ''_{SRR}). Since we obtained the imaginary part from the real part using the Kramer-Kronig relation, it is obvious that the imaginary part is causal. Hence, we derived an analytical model for the permeability of the SRR that satisfies causality. However, as the analytical μ''_{SRR} is complicated, it needs further simplification. Hence, our future work is to simplify the current analytical μ''_{SRR} to a much simplified form so that it could be used universally.

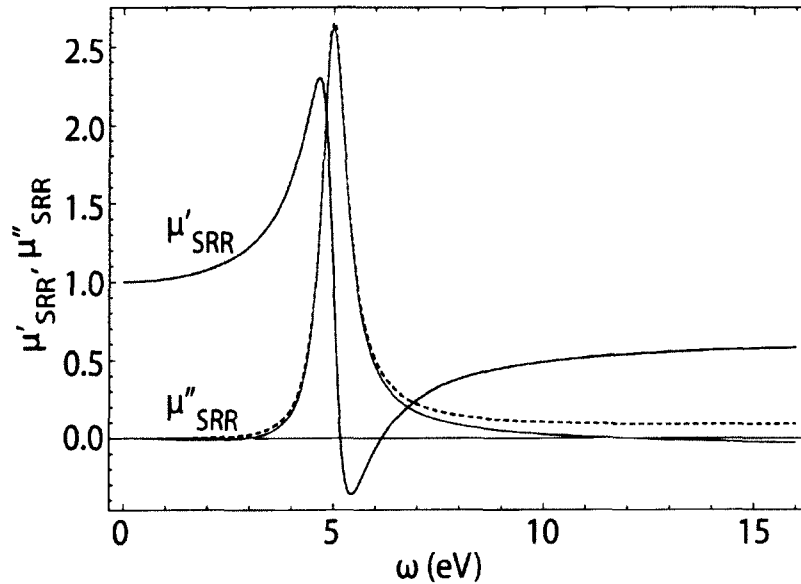


Figure 6.7: The analytical model of the permeability μ'_{SRR} (solid blue, Equation 6.36), μ''_{SRR} (solid red, Equation 6.41), and μ''_{SRR} (dashed black, Equation 6.37). Plotted for $\omega_{\tau 0} = 0.5$, $\alpha = 0.01$, $\omega_0 = 5eV$, and $p = 0.4$.

Most importantly, we compare μ''_{SRR} that satisfies causality in Equation 6.41 with the analytical model that is not causal in Equation 6.37 (see Figure 6.7). Although the non-

causal μ''_{SRR} is similar to causal μ''_{SRR} near resonance, for higher frequencies, both are dissimilar, and therefore the non-causal μ''_{SRR} cannot be used in the calculation of the Casimir force.

To conclude, we have derived the internal resistance, radiation resistance, equivalent capacitance, and inductance of a split ring resonator (SRR) and developed an analytical model for the effective permeability of a composite made of SRRs. We have also showed the importance of the radiation resistance at high frequencies, which is generally omitted. The approximated radiation resistance and its parametric domain for which it is valid is also provided. Based on the Kramers-Kronig relation, we have obtained a causal analytical result for the imaginary part of the effective permeability. This model can be used to properly calculate the Casimir force between metamaterial plates.

6.2.3 Permeability of the SRR at Imaginary Frequencies

Due to the approximation we have made earlier for the radiation resistance (see Equation 6.34), the analytical model for the effective permeability of the SRR composite is valid only within the limit $ka \leq 1$. Assuming that the lower order vacuum modes especially $n = 1$ falls in the range of $0 \leq ka \leq 1$, we analyze the permeability of the SRR at imaginary frequencies, as we intend to use in the application of the Casimir force. Figure 6.8 shows the permeability of the SRR for different thickness w and height h of the ring for a fixed radius a . Although the SRR provides strong magnetic properties at real frequencies, it behaves like a diamagnetic material at imaginary frequencies. We plot $\mu_{eff}(i\omega)$ for $0 \leq ka \leq 1$, the range for which the material is homogeneous.

Figure 6.8 shows that with an increase in the width and height of the SRR, the material becomes highly diamagnetic. The line denoted by $n = 1$ shows that the first

vacuum mode falls in the range of $0 \leq ka \leq 1$ when $a = 1 \mu\text{m}$ and $T = 300 \text{ K}$. Therefore, the material is diamagnetic at the first Matsubara frequency, a fact that can be used when designing quantum levitating systems. It is important to note that $\mu_{eff}(0) = 1$, regardless of the SRR geometrical properties.

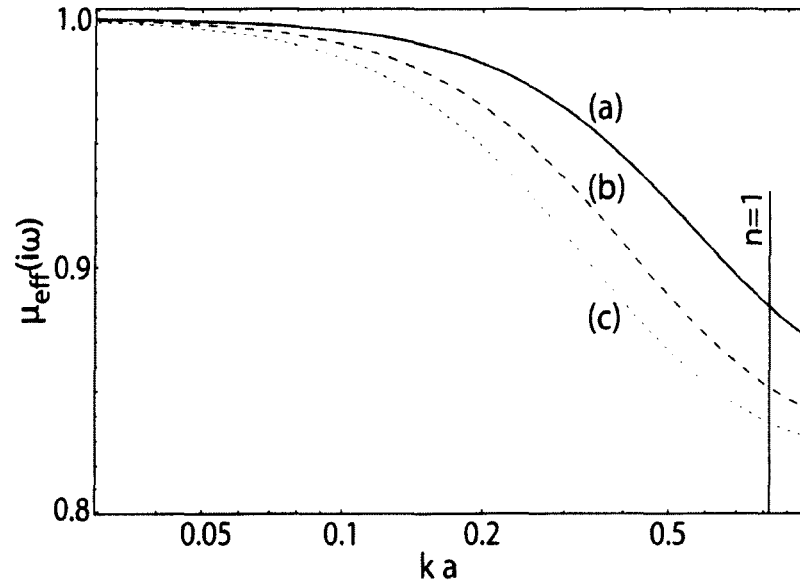


Figure 6.8: Permeability of the SRR for $a = 1 \mu\text{m}$, $2\varphi_0 = 2^\circ$ and (a) $w = h = 0.1a$, (b) $w = h = 0.2a$, and (c) $w = h = 0.3a$. The solid black line denoted by $n = 1$ represents the frequency corresponding to the first vacuum mode $k_T a = 2\pi a / \lambda_T$.

Figure 6.9 shows the maximum allowable radius of the SRR for the different number of the vacuum modes that falls in the limit $0 \leq ka \leq 1$, obtained by assuming $ka = 1$. This shows that the higher the number of vacuum modes for which a diamagnetic response is achieved, the smaller the radius of the SRR must be. This result can be explicitly written as $a \leq c / \omega_n = c / n\omega_T = \lambda_T / 2\pi n$.

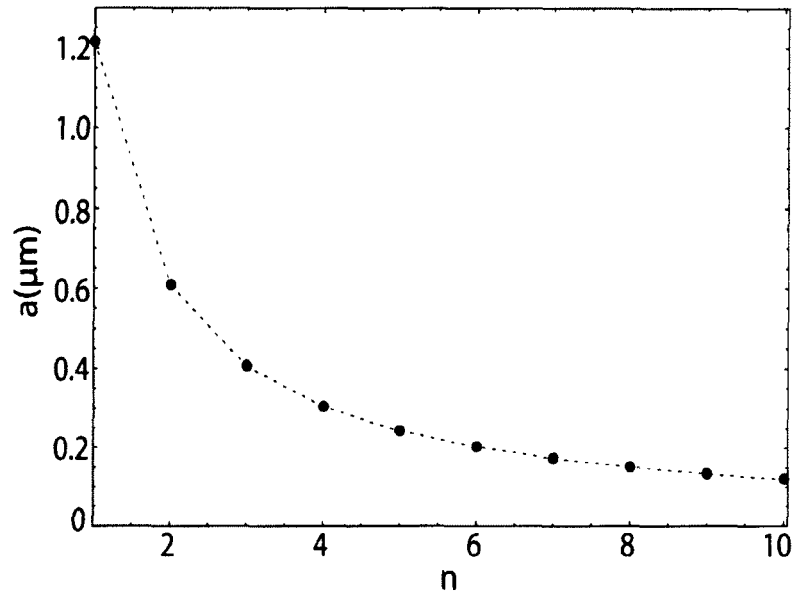


Figure 6.9: Maximum radius of the SRR a (red dots) allowable in the limit of $ka \leq 1$.

6.3 Ferromagnetic Nanocomposites

Ferromagnetic materials like nickel, yttrium iron garnet, magnetite, etc. have high permeability than other materials, especially at low frequencies in the GHz range. Although these materials have high permeability $\mu \gg 1$, the permittivity is generally even higher $\epsilon > \mu \gg 1$ and the necessary condition for force reversal is not satisfied [70]. However, in using composites with ferromagnetic materials included in a low permittivity dielectric host, it may be possible to satisfy the condition $\epsilon < \mu$ at low frequencies. Recently, this prospective has been considered by Inui with nickel nanopowder, a ferromagnetic material infused in to polystyrene spheres [30–32, 88].

Figure 6.10 illustrates the material composition of nickel polystyrene nanocomposites. The polystyrene acts as the framework which holds the nickel nanoparticles. The nickel nanoparticles can be viewed as discrete quasi-atoms with high magnetic moments that give rise to strong magnetization of the composite material. Since

the permittivities of the polystyrene and the air (the host) is low, it is also expected that the effective permittivity of the composite will also be relatively low as well [32].

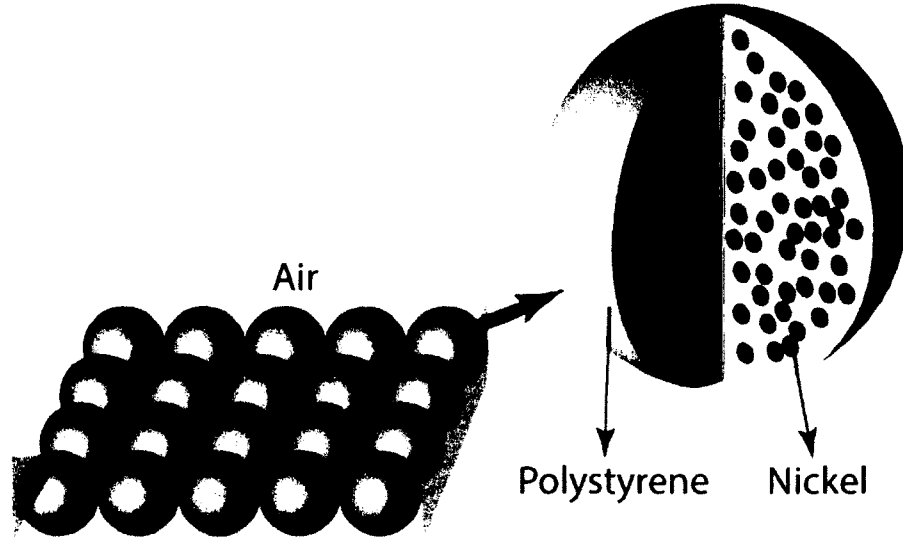


Figure 6.10: Nickel polystyrene nanocomposites with air as a host medium.

The effective permittivity/permeability of the nickel-polystyrene nanocomposites can be modeled using the Maxwell-Garnett theory [101,102], according to which the effective permittivity $\varepsilon_{eff}(i\omega)$ is related to the permittivity of the nickel and the polystyrene as [32],

$$\frac{\varepsilon_{eff}(i\omega) - 1}{\varepsilon_{eff}(i\omega) + 2} = f_1 \frac{\varepsilon_{Ni}(i\omega) - 1}{\varepsilon_{Ni}(i\omega) + 2} + f_2 \frac{\varepsilon_{poly}(i\omega) - 1}{\varepsilon_{poly}(i\omega) + 2}, \quad \text{Eq. 6.42}$$

where ε_{Ni} and f_1 are permittivity and filling fraction of the nickel and ε_{poly} and f_2 are permittivity and filling fraction of the polystyrene.

The effective permeability μ_{eff} of the composite material can be determined using Onsager's theory [103,104], according to which when the size of the nickel particles is much smaller than the field penetration depth (or skin depth) we have,

$$\mu_{eff}(i\omega) = \frac{1}{4} \left[1 + \frac{4\pi R f_1}{1 + \omega\tau} + \sqrt{8 + \left(1 + \frac{4\pi R f_1}{1 + \omega\tau}\right)^2} \right], \quad \text{Eq. 6.43}$$

where τ is Debye relaxation time, $R = 4\pi a_{Ni}^3 \bar{m}_0^2 / k_B T$, and \bar{m} is saturation magnetization.

Figure 6.11 depicts the effective permittivity and effective permeability of the composite material with filling fractions $f_1 = 0.2$, $f_2 = 0.1$ and the size of the nickel nanoparticles $a_{Ni} = 5 \text{ nm}$. Clearly, we have $\mu_{eff}(0) > \epsilon_{eff}(0)$ and the necessary condition for the Casimir force reversal can be satisfied for at least the $n = 0$ vacuum mode. Using cryogenic temperatures can substantially decrease the Matsubara frequencies and higher order modes may also be made to satisfy the condition $\mu_{eff}(i\omega_n) > \epsilon_{eff}(i\omega_n)$. Furthermore, modification of the permittivity/permeability can also be facilitated by changing the relative filling fractions of the nickel and polystyrene, or by choosing a different ferromagnetic material such as ferrite, yttrium iron garnet, etc.

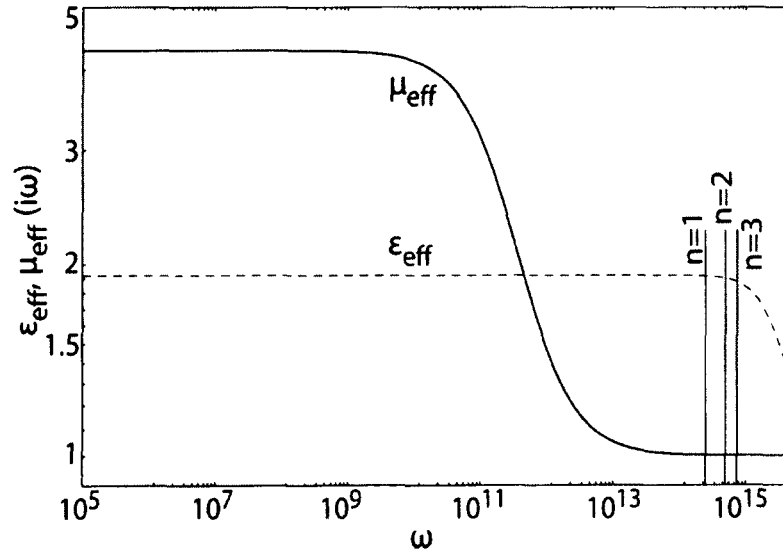


Figure 6.11: Effective permittivity ϵ_d (dashed red) and effective permeability μ_d (solid blue) of the nickel polystyrene nanocomposites. The solid black lines denotes the first, second, and third Matsubara frequencies.

6.4 Nanowire Composite Materials

A composite media made of pairs of parallel metal nanowires is another promising candidate for achieving repulsive Casimir force. The nanowire composite can manifest strong diamagnetic response, and if matched with a second paramagnetic plate, it can satisfy Dzyaloshinskii's condition for Casimir force reversal or $\mu_2 > 1 > \mu_1$ if the intermediate medium is non-magnetic. A nanowire-pair composite media has been proposed by A.N. Lagarkov and A.K. Sarychev as a means to introduce strong magnetic response in the near-infrared and optical spectral ranges [79]. A schematic of the composite is shown in Figure 6.12 (a) and it consists of metal nanowire pairs of permittivity ϵ_m dispersed in a dielectric host medium of permittivity ϵ_d .

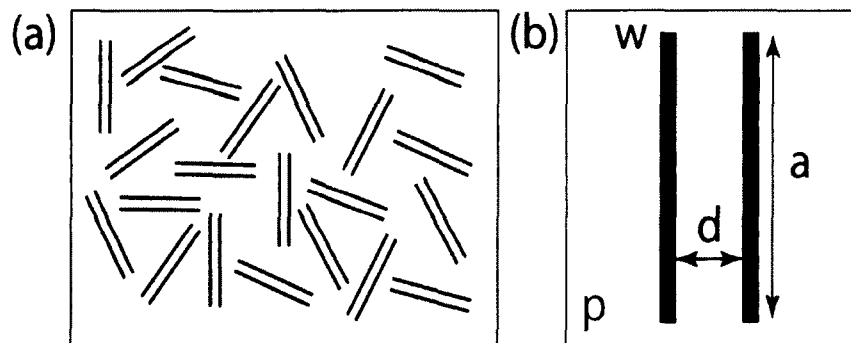


Figure 6.12: (a) Illustration of the nanowire composite media. (b) The composite is made of nano-wire pairs where w and a are the diameter and length of the wire, respectively, d is the separation distance between the wires.

Similar to that of the split ring resonator (SRR), a circulating current is generated in a pair of nanowires due to the incident time-varying magnetic field, which is assumed to be polarized perpendicularly to the surface of the pair. The basic response of the system can be simulated as a system of RLC elements with the gap between the nanowires acting as the capacitor. In the model developed by A.N. Lagarkov and A.K. Sarychev [79], the radiation resistance associated with the parallel-wire system was not considered.

If the host material is air, then the effective permittivity and permeability of the nanowire composite is given as,

$$\varepsilon_{eff}(i\omega) = 1 + \frac{4p}{awd} d_E, \quad \text{Eq. 6.44}$$

$$\mu_{eff}(i\omega) = 1 + \frac{4p}{awd} m_H, \quad \text{Eq. 6.45}$$

where p is the volume fraction of the nanowire, the d_E and m_H are the electric and magnetic dipole moments, respectively. If the permittivity nanowires is ε_m and $\mu_m = 1$ and a magnetic field is perpendicular to the surface of the material, the electric and the magnetic dipole moments are given as,

$$d_E = \frac{(2/3)aw^2\varepsilon_m}{1 + \varepsilon_m(w/a)^2 \ln[1 + \varepsilon_d a/w] \cosh[\varphi]}, \quad \text{Eq. 6.46}$$

$$m_H = 2a^3 C_2 \left(\frac{\omega d}{c}\right)^2 \frac{\tanh[g] - g}{g^3}, \quad \text{Eq. 6.47}$$

where $\varphi = (a\omega/c)\sqrt{\varepsilon_d \sqrt{\ln(a/w)/\ln(1 + \varepsilon_d a/w)}}$, $\Delta = w^2 2\pi\sigma_m\omega/c^2$, $g = a(\omega/c)\sqrt{\varepsilon_d \sqrt{1 + 1/2 \Delta f_{dei} \ln(d/w)}}$, $C_2 = \varepsilon_d/[4\ln(d/w)]$, and $\sigma_m = \omega\varepsilon_m/4\pi$.

Figure 6.13 shows the effective permittivity and permeability of the nanowire composite for different separation distances between the pair of gold nanowires. The spatial characteristics of the nanowires considered in the calculation are $a = 350 \text{ nm}$, $w = 30 \text{ nm}$, and $d = 150 \text{ nm}$ with a filling fraction of $p = 0.1$. The Drude model is used to model the permittivity of the gold nanowire, which is $\varepsilon_m(i\omega) = 5 + (\lambda/\lambda_p)^2/[1 + (\lambda/\lambda_\tau)]$, where $\lambda_p = 0.135 \mu\text{m}$ is the plasma wavelength and $\lambda_\tau = 58 \mu\text{m}$ is the relaxation wavelength [70]. Our results clearly show that for the system under consideration, the composite material is purely dielectric for low frequencies

with $\mu_{eff}(i\omega) \approx 1$ and $\epsilon_{eff}(i\omega) > 1$, whereas for higher frequencies the material acquires diamagnetic property with $\mu_{eff}(i\omega) < 1$ and $\epsilon_{eff}(i\omega) \approx 1$.

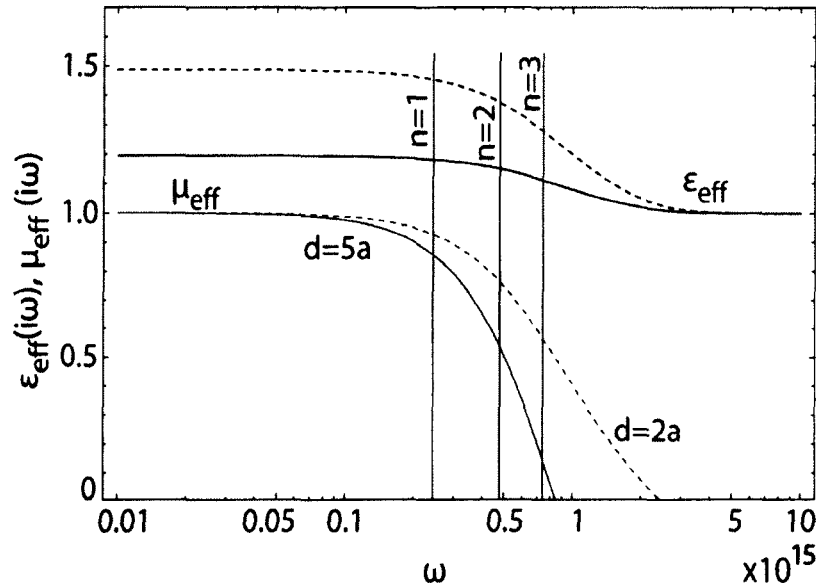


Figure 6.13: The permittivity and the permeability of the wire media showing diamagnetic properties at high frequencies. The solid black lines denotes the first, second, and third Matsubara frequencies.

The diamagnetic property could be extended for a broad range of frequencies, especially for the first few vacuum modes, by changing the permittivity of the host medium, dimensions and separation of the nanowires, and material of the nanowires. From Figure 6.11 the material is diamagnetic for the higher order modes $n \geq 1$ and becomes strongly diamagnetic with an increase in the separation distance between the nanowires, from $d = 2a$ to $d = 5a$.

In this section we have designed three potential electromagnetic metamaterials that manifest strong diamagnetic/paramagnetic across broad frequency ranges. These composite materials use nanoscopic resonators such as split ring resonators, parallel wires, and ferromagnetic nanoparticles that play a role similar to that of the atoms and molecules

in nature. Due to the relatively large sizes (compared to those of the atomic world), the nanostructured composites can manifest a much stronger electric and magnetic response at a pre-set frequency range. These materials can be utilized to realize (a) a system consisting of a pure dielectric material and a magneto-dielectric material, and (b) a system consisting of a diamagnetic plate and a paramagnetic plate satisfying Dzyaloshinskii's condition. A detailed design of these two systems will be discussed in Chapter 7.

CHAPTER 7

PRACTICAL MATERIAL CONFIGURATIONS FOR CASIMIR FORCE REVERSAL

7.1 Introduction

In the previous chapters, we have developed several theories for the Casimir force repulsion by considering specific cases and provided the necessary and the sufficient conditions that would help us in designing materials with such properties. In Chapter 6, we have discussed some of the most promising artificial material designs with high permeability and diamagnetic properties that can be considered for designing a quantum levitation system. The practical realization of such system is a challenging endeavor. For instance, the material properties required for repulsion (sufficient condition) needs to be satisfied for both plates and for a sufficiently broad spectral range. For example, in the case of a system with a dielectric and a highly magnetic materials satisfying the sufficient condition, the EMM plates based on SRRs or ferromagnetic nanocomposites needs to be predominantly magnetic for the frequencies corresponding to at least a few low order vacuum modes; otherwise, the repulsive force may not be achieved. Similar requirements must be imposed in case of a system with a diamagnetic plate and a paramagnetic plate (Dzyaloshinskii's condition) [17, 33].

Therefore, in this chapter we discuss some prospective material configurations and the possibility of satisfying the necessary condition for a sufficient number of vacuum

modes, which can lead to force reversal. We also present a technique for achieving quantum levitation without involving an exceedingly strong magnetic response by designing the plates to have substantially dissimilar magnetic and electric resonant frequencies.

7.2 Materials with Dissimilar Magnetic and Electric Resonant Frequencies

We begin by discussing an important technique which relies on a mismatch between the magnetic and electric resonance frequencies to design quantum levitation systems with substantially relaxed requirements for the magnetic response. We have already established that the necessary condition for force reversal $\mu > \epsilon$ provided for one of the plates is purely dielectric. However, it is unphysical to assume that this condition can be satisfied for all Matsubara frequencies as materials are nonmagnetic at high frequencies and there is substantial mismatch between the magnetic and electric oscillator strengths for naturally existing materials. Hence, as discussed in the previous chapters, we focus on designing artificial optical materials such that the sufficient condition is satisfied for one or a few of the lowest order vacuum modes, preferably for $n = 0$ and $n = 1$. In the analysis that follows, again we use the Lorentz oscillator model to model the plate's permittivities and the permeabilities (Equations 4.1 and 4.2).

First, we consider a case where the magnetic and electric resonance frequencies of the magneto-dielectric plate are the same. In this case, to satisfy the necessary condition we need a material with stronger magnetic dipole moments than the electric dipole moment or a higher magnetic plasma frequency than the electric plasma frequency, which is rather difficult to realize practically.

Figure 7.1 shows the permittivity and the permeability of the magneto-dielectric plate, assuming the magnetic and electric resonant frequencies are the same. In Figure 7.1

we showcase two possibilities, one with $\mu > \epsilon$ (corresponding to $\omega_{pm}/\omega_{pe} > 1$) and the other with $\mu < \epsilon$ (corresponding to $\omega_{pm}/\omega_{pe} < 1$).

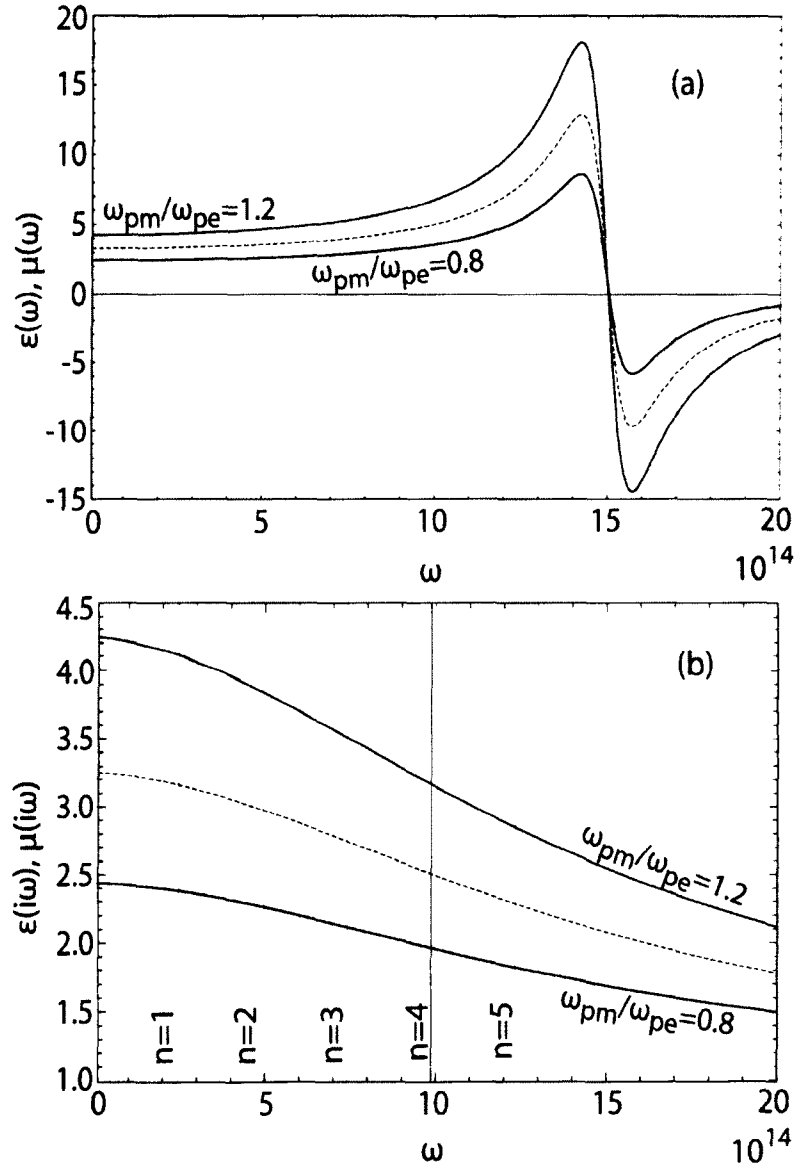


Figure 7.1: Permittivity and permeability of a magneto-dielectric material with equal magnetic and electric resonance frequencies. The dashed red line, blue, and black solid lines correspond to the permittivity, and the permeabilities with $\omega_{pm}/\omega_{pe} = 1.2$ and $\omega_{pm}/\omega_{pe} = 0.8$, respectively. We have also fixed the resonant frequencies $\omega_{0e} = \omega_{0m} = 1.5 \times 10^{15}$ rad/sec, the plasma frequency $\omega_{pe} = 1.5\omega_{0e}$ and the relaxation frequencies $\gamma_e = \gamma_m = 0.1\omega_{0e}$. The first few Matsubara frequencies are included with gray vertical lines.

Figure 7.1 (b) shows the material parameters plotted for imaginary frequencies. Provided $\omega_{pm}/\omega_{pe} < 1$ [solid black line in Figure 7.1 (b)], the permittivity is greater than the permeability $\epsilon > \mu$ for all frequencies. The first few vacuum modes corresponding to temperature $T = 300\text{ K}$ are also shown in Figure 7.1 (b) as a reference. We must note that the necessary condition $\mu > \epsilon$ is satisfied for all vacuum modes if the magnetic plasma frequency is higher than the dielectric plasma frequency $\omega_{pm}/\omega_{pe} > 1$ [solid blue line in Figure 7.1 (b)]. However, having $\omega_{pm}/\omega_{pe} > 1$ is practically challenging if not impossible. Hence, we seek an alternative approach based on magneto-dielectric materials with highly mismatched magnetic and electric resonant frequencies.

Figure 7.2 (a) shows a particular case where $\omega_{0e} > \omega_{0m}$. Figure 7.2 (b) clearly shows that for such materials the permeability is greater than the permittivity for the lower order vacuum modes even if the magnetic plasma frequency is less than the electric plasma frequency $\omega_{pm}/\omega_{pe} = 0.5$. This suggests that it may be advantageous to design EMMs based on SRRs, parallel slabs, etc. with highly mismatched magnetic and electric resonant frequencies. This will relax the seemingly unphysical conditions for having a magnetic plasma frequency larger than the dielectric plasma frequency. There is thus high confidence that such metamaterial plates may provide the possibility of realizing quantum levitation in practice.

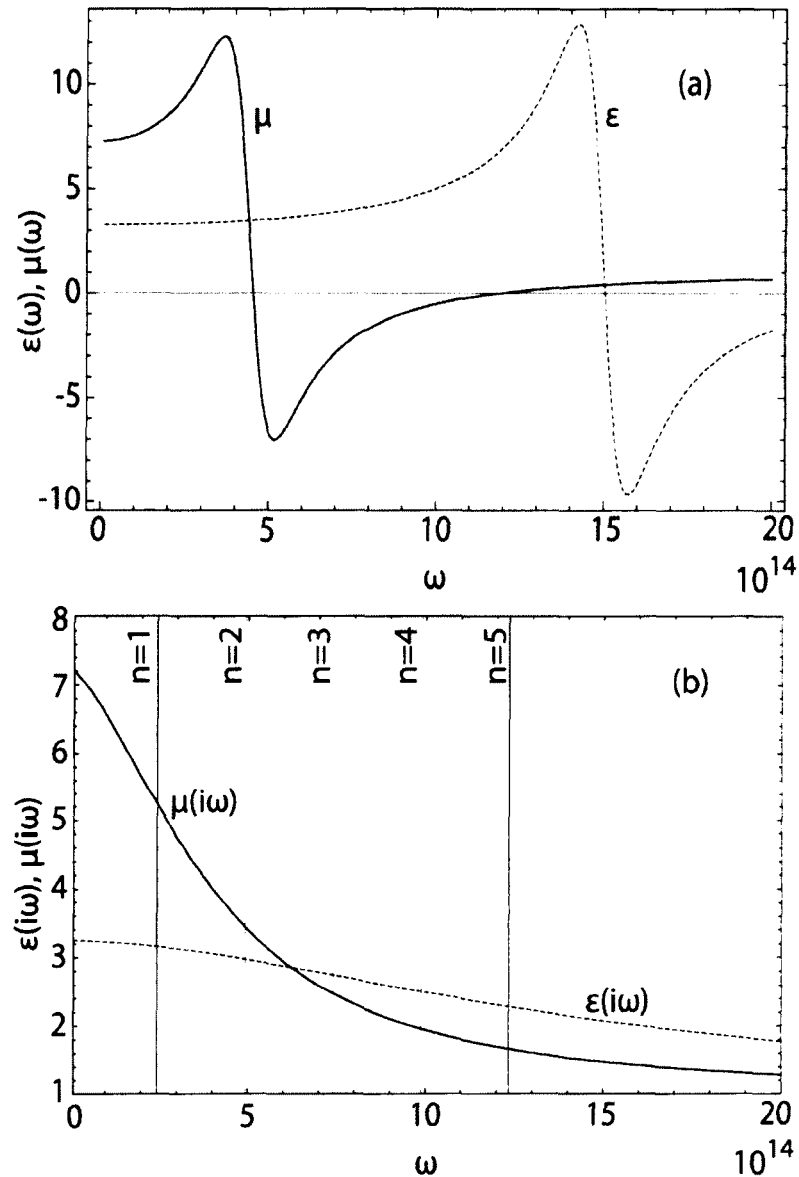


Figure 7.2: Permittivity and permeability of a magneto-dielectric material with highly mismatched resonance frequencies plotted for (a) real and (b) imaginary frequencies with the parameters of the Lorentz model used in the plots are as follow: $\omega_{0e} = 1.5 * 10^{15}$ rad/sec, $\omega_{pe} = 1.5\omega_{0e}$, $\omega_{0m} = 0.3\omega_{0e}$, $\omega_{pm} = 0.5\omega_{pe}$, and $\gamma_e = \gamma_m = 0.1\omega_{0e}$.

7.3 A Dielectric Plate and a Magneto-Dielectric Plate

We have already studied this particular configuration in Chapter 4 and obtained the necessary and the sufficient conditions for force reversal. According to the analysis, it was clear that this is probably the most promising configurations for the realization of repulsive

Casimir force in practice. Here, we study a system consisting of one of the plates being made of polystyrene ferromagnetic nanocomposites (metamaterial plate) and the other plate being a purely dielectric plate with $\mu = 1$. The polystyrene ferromagnetic nanocomposite was already discussed in Chapter 6. Figure 7.3 illustrates the parallel-plate configuration under consideration.

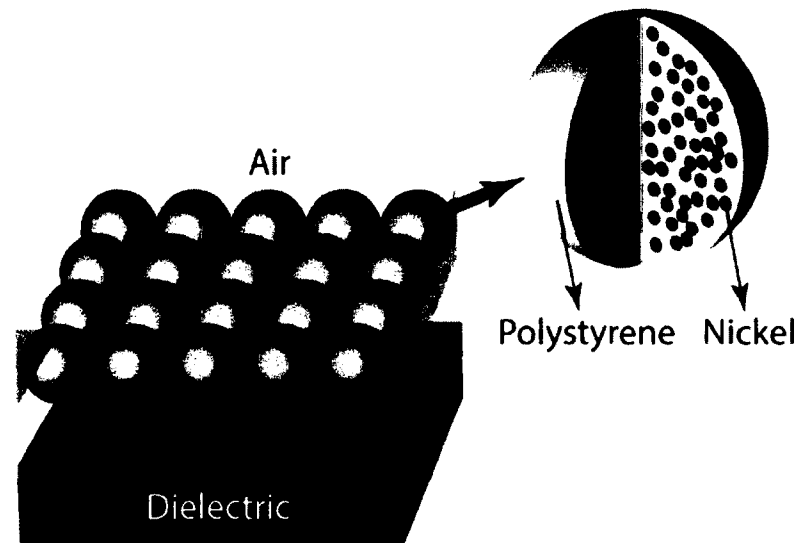


Figure 7.3: Parallel-plate system with one plate made of polystyrene ferromagnetic nanocomposites and the other being a pure dielectric plate.

The polystyrene ferromagnetic nanocomposites plate consists of nickel (ferromagnetic) nanoparticles embedded in polystyrene ($\epsilon_{pol} \approx 1.253$) with the host material being air [32, 88]. As shown in Figure 6.11 (in Chapter 6), the permeability of the metamaterial plate is greater than the permittivity at low frequencies. Specifically, at ambient temperatures we have $\mu(0) = 4.32 > \epsilon(0) = 1.92$. However, in that particular example the necessary condition is no longer satisfied for the Matsubara frequencies with $n \geq 1$ (for instance $\mu(n = 1) = 1.013 \not> \epsilon(n = 1) = 1.911$). More modes can be

included by changing the volume fractions of the constituents, the temperature or the radius of the nickel nanoparticles so that we can tune the magnetic permeability.

Hence, to identify the parametric domain for which the necessary condition for force reversal is satisfied, we varied the size of the nickel nanoparticles a_{Ni} for the different vacuum mode number at $T = 300 K$. Figure 7.4 shows the parametric domain where the necessary condition for force reversal is satisfied ($\mu_{eff} > \epsilon_{eff}$) as function of the size of the nickel nanoparticles a_{Ni} and mode number. Clearly, increasing the size of the nickel nanoparticles increases the number of modes that will contribute to repulsion.

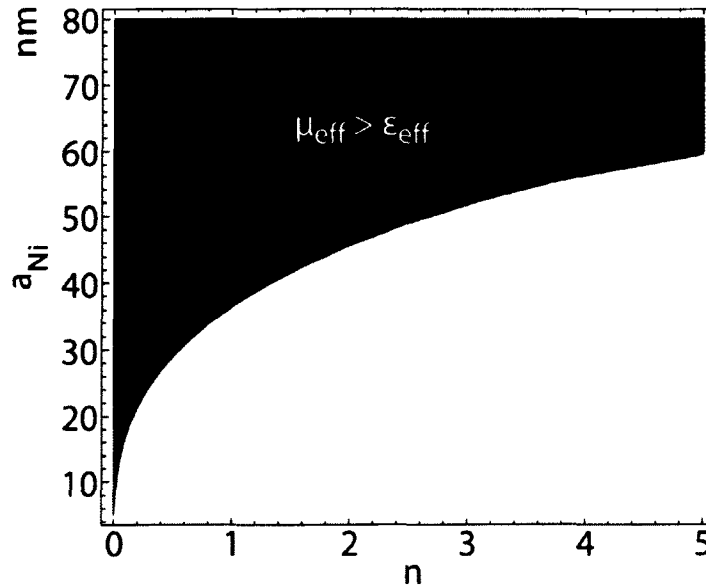


Figure 7.4: Parametric domain satisfying the necessary condition for repulsive Casimir force. In the calculations, we have fixed the volume fractions of the constituents $f_1 = 0.2$ (nickel) and $f_2 = 0.1$ (polystyrene).

The Casimir force calculated for three different nickel nanoparticle sizes is shown in Figure 7.5. In the calculations, the permittivity of the pure dielectric plate (plate 1) is set at $\epsilon_1 = 2$ ($\mu_1 = 1$). For $a_{Ni} = 60 nm$, even though the material is strongly magnetic for the lower order modes, the Casimir force is attractive for all plate separations [case (a) in

Figure 7.5]. However, by increasing the size of the nickel particles, the force becomes repulsive for intermediate plate separation distances and with a further increase in the particle size, the repulsive window increases [case (b) & (c) in Figure 7.5]. As expected, for a parallel-plate configuration with one of the plates being purely dielectric, the force is attractive for large and small plate separations and quantum levitation can only be achieved for intermediate plates separations (refer to Chapters 4 and 5).

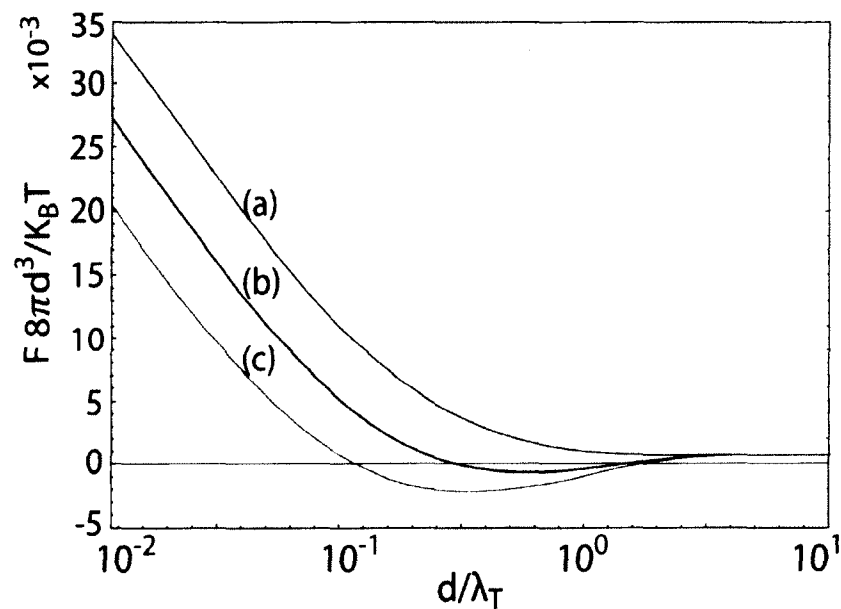


Figure 7.5: Casimir force for different nickel nanoparticle sizes a_{Ni} . (a) 60 nm, (b) 80 nm, and (c) 100 nm.

Furthermore, a wider repulsive window and/or stronger force may be achieved by varying the filling fraction of the ferromagnetic inclusions and polystyrene. Alternatively, we can also consider using a variety of ferromagnetic materials such as yttrium iron garnet, magnetite, etc. Similarly, the polystyrene could also be replaced with other low permittivity dielectric materials.

7.4 A Diamagnetic and a Paramagnetic Plate

Another promising parallel-plate configuration that can be used for Casimir force repulsion is a system consisting of a paramagnetic plate (plate 1) and a diamagnetic plate (plate 2) that satisfies the Dzyaloshinskii's condition for μ , see Figure 7.6. For the paramagnetic plate, we can consider the polystyrene ferromagnetic nanocomposites studied above (with $\mu(i\omega) > 1$) [32,88] while the diamagnetic plate can be engineered as a composite made of metal nanowires pairs (with $\mu(i\omega) < 1$) [79]. The nanowires composite was already studied in Chapter 6 (Section 6.4) where we showed that its magnetic and dielectric response can be modeled as a lumped RLC circuits. Since the magnetic and electric resonance frequencies depend on the geometrical properties of the metal nanowires they could be easily tailored in order to fit the requirements for Casimir force reversal.

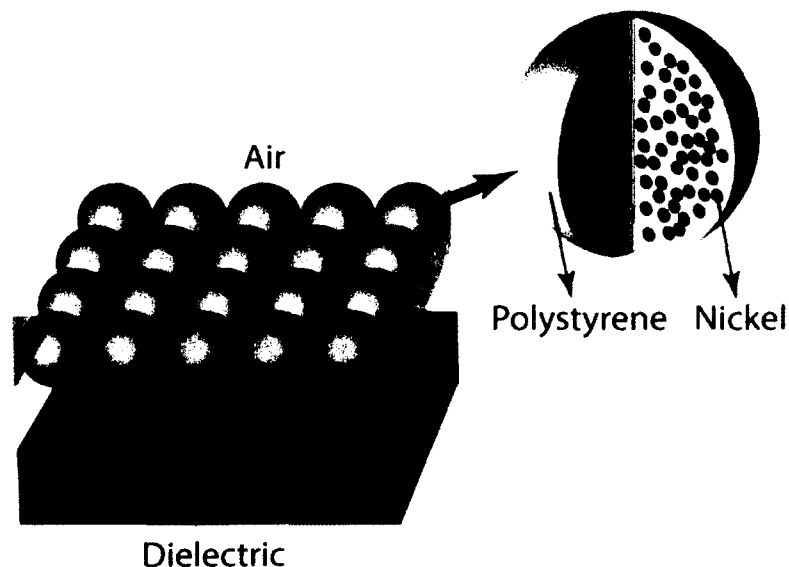


Figure 7.6: Quantum levitation system with a paramagnetic plate (plate 1) made of polystyrene ferromagnetic nanocomposites and a diamagnetic plate (plate 2) made of parallel nanowires dispersed in a dielectric host.

The composite media made of parallel nanowires can be either paramagnetic [$\mu(\omega) > 1$] or diamagnetic [$\mu(\omega) < 1$] for the complex Matsubara frequencies depending on the dimensions and spacing between the wires. Figure 7.7 shows the parametric domain for a nanowire composite with diamagnetic response. In the calculations we have we utilized a gold nanowire with the fixed diameter $w = 10 \text{ nm}$.

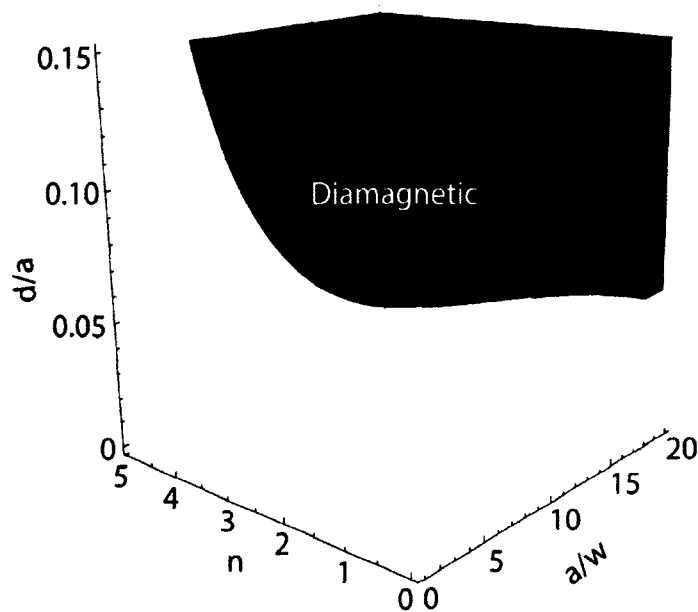


Figure 7.7: Parametric domain for which the nanowire composite plate is diamagnetic.

The general design rule for achieving quantum levitation based on the above described configuration is as follows. Using the parametric domain calculated in Figure 7.7, choose a set of geometrical parameters such that the metal nanowire composite is diamagnetic for a sufficient number of modes. We must note that the diamagnetic properties of the nanowire composite are stronger if the ratio of the nanowire's length vs. diameter (a/w) increases. We have already identified that the nickel polystyrene nanocomposites is paramagnetic for all frequencies and its permeability increases with the

increase of the nickel nanoparticle's size. It is thus expected that a large number of composite configurations may lead to quantum levitation.

As an example, we depict in Figure 7.8 the Casimir force as a function of the plate separation for three configurations, each having different nanowire sizes a .

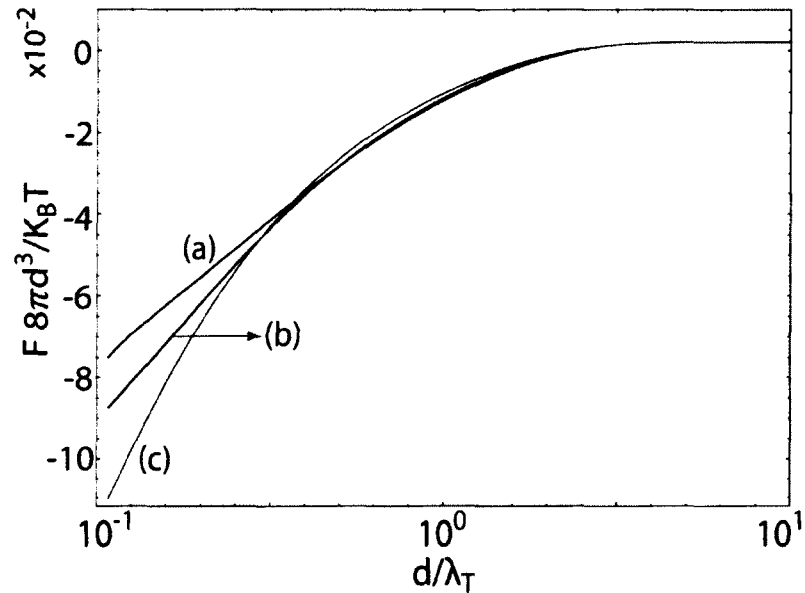


Figure 7.8: Casimir force for different lengths of the nanowire pairs (plate 2), (a) $a = 200 \text{ nm}$, (b) $a = 400 \text{ nm}$, and (c) $a = 600 \text{ nm}$. The fixed size of the nickel nanoparticles (plate 1) is fixed at $a_{Ni} = 20 \text{ nm}$.

Our results show that the repulsive Casimir force increases with an increase in the diamagnetic response of plate 2 (increasing a/w ratio) for small plate separations. For the ferromagnetic plate (plate 1), we have fixed the filling fractions of the nickel and polystyrene as $f_1 = 0.2$ and $f_2 = 0.1$, respectively. The diamagnetic plate (plate 2) is made of nanowires with equal diameters $w = 10 \text{ nm}$ and separated by distance $d = 0.1a$. When considering the dependence of the force on the plate's separation distance, we note that at zero frequency the two plates are nonmagnetic. Hence, the Casimir force at large plate separations will always be attractive (see the large distance asymptotic result from

Equation 2.37). The repulsion can only occur at plate separation less than a given critical value and increases with an increase in the nanowire size a .

Similarly, in Figure 7.9 we investigate the Casimir force for three different configurations of the paramagnetic plate (plate 1). Specifically, we vary the size of the nickel particles keeping in mind that an increase in size translates into a stronger magnetic response (see Figure 7.5). In the calculation we have fixed the dimensions of the gold nanowires (plate 2) (see Figure 7.9). As expected, the Casimir force is again positive at large plate separations, and it becomes negative below some critical separation distance. The force also increases with an increase of the nickel nanoparticle's size.

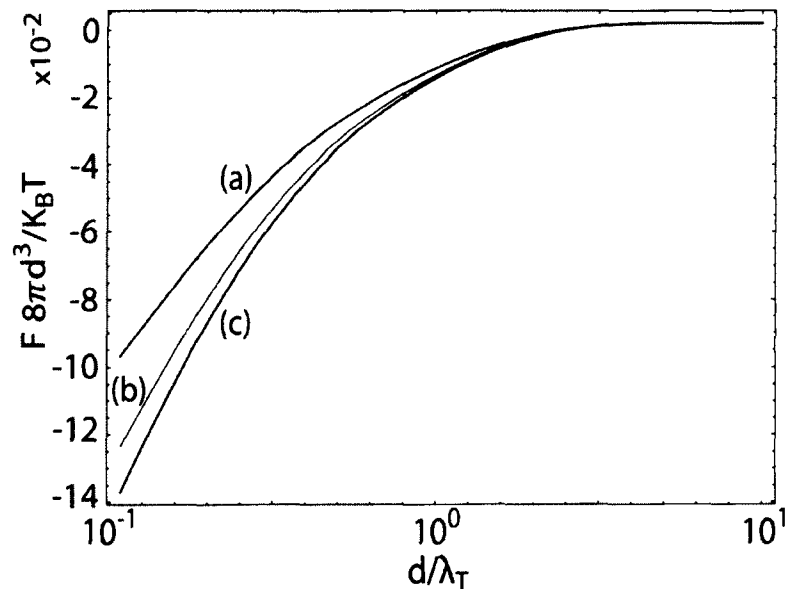


Figure 7.9: Casimir force for different nickel nanoparticle sizes (plate 1), (a) $a_{Ni} = 20 \text{ nm}$, (b) $a_{Ni} = 40 \text{ nm}$, and (c) $a_{Ni} = 80 \text{ nm}$. The length and diameter of the nanowires (plate 2) are fixed as $a = 100 \text{ nm}$ and $w = 10 \text{ nm}$, respectively, and separated by $d = 0.1a$.

To conclude, in this section, we have proposed and studied a realistic quantum levitation system based on two parallel plates made of ferromagnetic and diamagnetic composites, respectively. We show that regardless of the composite's geometry and hence

magneto-dielectric properties, the Casimir force is attractive for large plate separations and can turn into repulsive if the plate separation is smaller than a critical value. The critical plate separation distance is thus a stable (equilibrium) point of the system. This points toward possible applications such as frictionless transport in the nanoscale (nano- maglev) and contact free MEMS based actuators and mechanical micro machines.

CHAPTER 8

CONCLUSIONS AND FUTURE WORK

8.1 Conclusions

In this dissertation we have performed a comprehensive study of the Casimir force reversal (quantum levitation) in parallel-plate configurations. We have considered the practically important case of air as a host medium and have obtained both necessary and sufficient conditions for force reversal. Practical achievable designs based on the current state of nanotechnology have been proposed.

Specifically, we have provided a general mathematical description of the effect of quantum levitation (repulsive Casimir forces) for both dispersive and non-dispersive material plates. We have established the necessary and sufficient conditions for force reversal as functions of the plate's spectral response functions. For the case of non-dispersive plates, we have identified six universal types of the Casimir force based on which various types of devices such as sensors and actuators could be engineered. Considering the practical limitations on the permittivities and permeabilities of naturally existing materials as well as recently developed artificial electromagnetic material, i.e. metamaterials, we have concluded that the use of a dominantly magnetic non-dispersive plate in connection with a purely dielectric second plate is the most promising configuration for achieving quantum levitation.

In the case of dispersive materials, we have studied two distinct configurations. First, we consider a system consisting of a non-dispersive dielectric plate (simulating a nanoscale device) coupled to a dispersive magneto-dielectric plate (acting as a substrate). For this configuration, we have derived an explicit upper analytical bound of the Casimir force. In using this bound, we have obtained a sufficient condition for quantum levitation in terms of the specular functions of the plates at zero and the thermal frequencies. The second configuration that has been considered consists of dispersive magneto-dielectric plate and dispersive dielectric plate.

Again, we were able to derive, for the first time, both the necessary and sufficient condition for quantum levitation. The complete parametric domains corresponding to Casimir force reversal have been investigated in details and possible directions for practical realization of quantum levitation have been outlined. Specifically, we have shown that (1) in both cases, the Casimir force is attractive for large and small plate separations, (2) if the two plates are identical, the Casimir force is always attractive, and (3) we have identified that the magneto-dielectric plate must be dominantly magnetic for a substantial frequency range encompassing at least a few of the low order Matsubara frequencies. Based on these conclusions, we have designed three potential electromagnetic metamaterials that manifest strong diamagnetic/paramagnetic across broad frequency ranges. These composite materials use nanoscopic resonators such as split ring resonators, parallel wires, and ferromagnetic nanoparticles that play a role similar to that of the atoms and molecules in nature. Due to the relatively large sizes (compared to those of the atomic world), the nanostructured composites can manifest much stronger electric and magnetic response at a

pre-set frequency range. By using such designed metamaterials, we have presented two realistic quantum levitation systems.

The first system consists of a dielectric plate and a dominantly magnetic plate made of nickel polystyrene nanocomposites. The second system consists of a diamagnetic plate made of parallel nanowire composites and a second paramagnetic plate made of the nickel polystyrene nanocomposites. We have shown that for both systems, and regardless of the composite's geometry and hence magneto-dielectric properties, the Casimir force is attractive for large plate separations. However, depending on the design parameters, the Casimir force can reverse into repulsive provided the plate separation is smaller than a critical value. The critical plate separation distance corresponds to a stable (equilibrium) point for both system, which allows for applications involving frictionless transport at the nanoscale (nano-maglev), contact free MEMS based actuators, and mechanical micro-machines.

8.2 Future Work

In this dissertation, we have provided a comprehensive theoretical investigation of quantum levitation systems based on magneto-dielectric materials in the parallel-plate configuration. While we have theoretically demonstrated that quantum levitation can be achieved using designed composite materials, an experimental verification of the described effects has not been provided. Furthermore, there are a number of reasonable assumptions that have been made as part of the developed theory that may need to be reconsidered when compared with actual experimental data. For example, in the theory the plates are assumed to be semi-infinite with perfectly smooth surfaces, which will be difficult to achieve in an actual experiment. Any surface discontinuities (roughness) will introduce a large number

of scattering centers and hence the modes inside the plates cannot be modeled as plain waves (which is the basis of the main result of Equation 2.30). In what follows, we identify a number of possible issues that may rise in actual experiments and also provided possible research directions that may improve the overall performance of the quantum levitation system.

1. For all plate configurations discussed in this dissertation, we have assumed that the plates are semi-infinite in size (having a thickness much larger than the plate separation distance and for all practical purposes assumed to be infinitely large). However, in practice the plates will have a finite thickness and only if the electromagnetic modes are evanescent or strongly decaying (due to energy dissipation) within the plates the developed theory can be trusted. Otherwise, an analysis using the proper specular functions (for multi-interface configurations) must be performed.
2. From the point of view of practically designing a quantum levitation system, the use of an artificially engineered material may require another material as a substrate for achieving required mechanical strength for proper operation of a device. Furthermore, in some cases, the system may require the magneto-dielectric as a coating on the surface of other material. For such cases, the plate involving the magneto-dielectric material can be viewed as a multi-layered plate. Therefore, a detailed study of Casimir force reversal conditions for multi-layered plates are highly desirable.
3. The Casimir force reversal analysis presented for a system with a dielectric plate and a predominantly magnetic metamaterial plate (in Chapter 7, Section

7.3), could be extended for other ferromagnetic materials like yttrium iron garnet, magnetite, etc. and the polystyrene could be replaced with other low permittivity dielectric host, such that a stronger repulsive force is achieved.

4. In all the analyses performed (in Chapters 4 and 5) for obtaining a condition for quantum levitation, we have omitted a material with optical gain, as the Lifshitz theory may not be applicable due to possible thermal fluctuations in the system. However, the Casimir force for thermally non-equilibrium systems has already been studied and a correction factor to the Casimir force based on Lifshitz theory, to account for the thermal fluctuations in an amplifying media, have been derived. Therefore, using the modified theory, the role of optical gain in the reversal of Casimir force could be investigated.

The above mentioned are the prospective areas of research, as an extension to our work, which would provide a comprehensive knowledge on the possibility of achieving quantum levitation. The resulting material conditions for Casimir force reversal for a single layered and/or multi-layered plates may include the effect of surface roughness and the role of amplifying media. Based on these knowledge, one can design a variety of Casimir force based actuators and/or sensors with a wide range of applications.

BIBLIOGRAPHY

- [1] H. B. G. Casimir and D. Polder, *Phys. Rev.* **73**, 360 (1948).
- [2] E. M. Lifshitz, *Sov. Phys. JETP.* **2**, 73 (1956).
- [3] A. W. Rodriguez, F. Capasso, and S. G. Johnson, *Nat Phot.* **5**, 211.
- [4] P. Milonni, *The Quantum Vacuum An Introduction to Quantum Electrodynamics* (Academic Press Inc, London, 1993).
- [5] K. A. Milton, *The Casimir Effect Physical Manifestations of Zero-Point Energy* (World Scientific, Singapore, 2001).
- [6] P. W. Milonni and M.-L. Shih, *Contemp. Phys.* **33**, 313 (1992).
- [7] M. Bordag, G. L. Klimchitskaya, U. Mohideen, and V. M. Mostepanenko, *Advances in the Casimir Effect* (Oxford University Press, Oxford, 2009).
- [8] Natl. Inst. Stand. Technol. Gaithersburg, MD 20899, <http://physics.nist.gov/cgi-bin/cuu/Value?plkt> (accessed May 4, 2014).
- [9] H. B. G. Casimir, *Proc. K. Ned. Akad. Wet.* **51**, 793 (1948).
- [10] M. Bordag, U. Mohideen, and V. M. Mostepanenko, *Phys. Rep.* **353**, 1 (2001).
- [11] V. Adrian Parsegian, *Van Der Waals Forces* (Cambridge University Press, New York, 2006).
- [12] D. J. Griffiths, *Introduction to Quantum Mechanics* (Pearson Prentice Hall, New Jersey, 2005).
- [13] *Quantum vacuum fluctuations*, <http://www.lactamme.polytechnique.fr/images/VIDE.21.0128.D/display.html> (accessed May 4, 2014).
- [14] H. Yokoyama and K. Ujihara, *Spontaneous Emission and Laser Oscillation in Microcavities* (CRC Press, Boca Raton, 1995).
- [15] M. O. Scully and M. S. Zubairy, *Quantum Optics* (Cambridge University Press, New York, 1997).

- [16] L. D. Landau, E. M. Lifshitz, and L. P. Pitaevskii, *Electrodynamics of Continuous Media*, 2nd ed. (Elsevier Science and Technology, Oxford, 1984).
- [17] I. E. Dzyaloshinskii, E. M. Lifshitz, and L. P. Pitaevskii, *Sov. Phys. Uspekhi* **4**, 153 (1961).
- [18] M. J. Sparnaay, *Physica* **24**, 751 (1958).
- [19] S. K. Lamoreaux, *Phys. Rev. Lett.* **78**, 5 (1997).
- [20] U. Mohideen and A. Roy, *Phys. Rev. Lett.* **81**, 4549 (1998).
- [21] A. Meurk, P. F. Luckham, and L. Bergström, *Langmuir* **13**, 3896 (1997).
- [22] E. Buks and M. L. Roukes, *Phys. Rev. B* **63**, 33402 (2001).
- [23] F. M. Serry, D. Walliser, and G. J. Maclay, *J. Appl. Phys.* **84**, 2501 (1998).
- [24] S. L. Boersma, *Am. J. Phys.* **64**, (1996).
- [25] K. Autumn, M. Sitti, Y. A. Liang, A. M. Peattie, W. R. Hansen, S. Sponberg, T. W. Kenny, R. Fearing, J. N. Israelachvili, and R. J. Full, *Proc. Natl. Acad. Sci.* **99**, 12252 (2002).
- [26] E. Buks and M. L. Roukes, *Nature* **419**, 119 (2002).
- [27] B. Geyer, G. L. Klimchitskaya, and V. M. Mostepanenko, *Phys. Rev. B* **81**, 104101 (2010).
- [28] C. Henkel and K. Joulain, *Europhys. Lett.* **72**, 929 (2005).
- [29] D. Iannuzzi and F. Capasso, *Phys. Rev. Lett.* **91**, 29101 (2003).
- [30] N. Inui, *J. Appl. Phys.* **111**, 74304 (2012).
- [31] N. Inui, *Phys. Rev. A* **84**, 52505 (2011).
- [32] N. Inui, *Phys. Rev. A* **83**, 32513 (2011).
- [33] O. Kenneth, I. Klich, A. Mann, and M. Revzen, *Phys. Rev. Lett.* **89**, 33001 (2002).
- [34] I. G. Pirozhenko and A. Lambrecht, *J. Phys. A Math. Theor.* **41**, 164015 (2008).
- [35] F. S. S. Rosa, *J. Phys. Conf. Ser.* **161**, 12039 (2009).
- [36] L. Rosa and A. Lambrecht, *Phys. Rev. D* **82**, 65025 (2010).

- [37] J.-N. Ding, S.-Z. Wen, and Y.-G. Meng, *J. Micromechanics Microengineering* **11**, 202 (2001).
- [38] F. Capasso, *IEEE J. Sel. Top. Quantum Electron.* **88**, 053602 (2007).
- [39] A. K. Popov and V. M. Shalaev, *Opt. Lett.* **31**, 2169 (2006).
- [40] J. Faist, F. Capasso, D. L. Sivco, C. Sirtori, A. L. Hutchinson, and A. Y. Cho, *Sci.* **264**, 553 (1994).
- [41] Y. Sherkunov, *Phys. Rev. A* **72**, 052703 (2005).
- [42] A. Sambale, D.-G. Welsch, S. Y. Buhmann, and H. T. Dung, *Phys. Rev. A* **80**, 5 (2009).
- [43] T. H. Boyer, *Phys. Rev. A* **9**, 2078 (1974).
- [44] U. Leonhardt and T. G. Philbin, *New J. Phys.* **9**, 254 (2007).
- [45] V. G. Veselago, *Sov. Phys. Uspekhi* **10**, 509 (1968).
- [46] J. Valentine, S. Zhang, T. Zentgraf, E. Ulin-Avila, D. A. Genov, G. Bartal, and X. Zhang, *Nature* **455**, 376 (2008).
- [47] W. Cai, D. A. Genov, and V. M. Shalaev, *Phys. Rev. B* **72**, 193101 (2005).
- [48] F. S. S. Rosa, D. A. R. Dalvit, and P. W. Milonni, *Phys. Rev. Lett.* **100**, 183602 (2008).
- [49] J. N. Munday, F. Capasso, and V. A. Parsegian, *Nature* **457**, 170 (2009).
- [50] A. D. Phan and N. A. Viet, *Phys. Status Solidi - Rapid Res. Lett.* **6**, 274 (2012).
- [51] I. G. Lambrecht, A. and Pirozhenko, *Phys. Rev. A* **78**, 62102 (2008).
- [52] V. Yannopoulos and N. V. Vitanov, *Phys. Rev. Lett.* **103**, 120401 (2009).
- [53] V. K. Pappakrishnan, P. C. Mundru, and D. A. Genov, *Phys. Rev. B* **89**, 45430 (2014).
- [54] V. M. Shalaev, *Nat Phot.* **1**, 41 (2007).
- [55] S. A. Ramakrishna, *Reports Prog. Phys.* **68**, 449 (2005).
- [56] W. Cai, U. K. Chettiar, A. V. Kildishev, and V. M. Shalaev, *Nat Phot.* **1**, 224 (2007).

- [57] P. C. Mundru, V. Pappakrishnan, and D. A. Genov, *Phys. Rev. B* **85**, 45402 (2012).
- [58] D. A. Genov and P. C. Mundru, *J. Opt.* **16**, 15101 (2014).
- [59] S. Zhang, D. A. Genov, C. Sun, and X. Zhang, *Phys. Rev. Lett.* **100**, 123002 (2008).
- [60] C. Genet, A. Lambrecht, and S. Reynaud, *Phys. Rev. A* **67**, 43811 (2003).
- [61] E. M. Lifshitz and L. P. Pitaevskii, *Statistical Physics, Part II* (Pergamon, Oxford, 1980).
- [62] S. M. Rytov, *Theory of Electrical Fluctuations and Thermal Radiation* (Publishing House, Academy of Sciences, USSR, 1953).
- [63] N. G. Van Kampen, B. R. A. Nijboer, and K. Schram, *Phys. Lett. A* **26**, 307 (1968).
- [64] B. Ninham, V. A. Parsegian, and G. Weiss, *J. Stat. Phys.* **2**, 323 (1970).
- [65] K. Schram, *Phys. Lett. A* **43**, 282 (1973).
- [66] D. Langbein, *Solid State Commun.* **12**, 853 (1973).
- [67] G. L. Klimchitskaya, U. Mohideen, and V. M. Mostepanenko, *Phys. Rev. A* **61**, 62107 (2000).
- [68] B. Geyer, G. L. Klimchitskaya, and V. M. Mostepanenko, *Phys. Rev. A* **67**, 62102 (2003).
- [69] Mark Fox, *Optical Properties of Solids* (Oxford University Press, UK, 2001).
- [70] E. D. Palik, *Handbook of Optical Constants of Solids* (Academic Press, San Diego, 1985).
- [71] S. Xiao, V. P. Drachev, A. V Kildishev, X. Ni, U. K. Chettiar, H.-K. Yuan, and V. M. Shalaev, *Nature* **466**, 735 (2010).
- [72] K. A. M. and E. K. A. and P. P. and N. P. and I. B. and S. Å. Ellingsen, *J. Phys. A Math. Theor.* **45**, 374006 (2012).
- [73] J. B. Pendry, A. J. Holden, D. J. Robbins, and W. J. Stewart, *IEEE Trans. Microw. Theory Tech.* **47**, 2075 (1999).
- [74] M. S. Wheeler, J. S. Aitchison, and M. Mojahedi, *Phys. Rev. B* **72**, 193103 (2005).
- [75] B.-I. Popa and S. A. Cummer, *Phys. Rev. Lett.* **100**, 207401 (2008).

- [76] A. N. Lagarkov, V. N. Semenenko, V. A. Chistyayev, D. E. Ryabov, S. A. Tretyakov, and C. R. Simovski, *Electromagnetics* **17**, 213 (1997).
- [77] O. Acher, P. M. Jacquart, J. M. Fontaine, P. Baclet, and G. Perrin, *IEEE Trans. Magn.* **30**, 4533 (1994).
- [78] H. Chen, L. Huang, X. Cheng, and H. Wang, *Prog. Electromagn. Res.* **115**, 317 (2011).
- [79] A. N. Lagarkov and A. K. Sarychev, *Phys. Rev. B* **53**, 6318 (1996).
- [80] I. S. Nefedov, A. C. Tarot, and K. Mahdjoubi, in *Antenna Technol. Small Smart Antennas Metamaterials Appl. 2007, IWAT '07*, pp. 101–104.
- [81] A. Demetriadou and J. B. Pendry, *J. Phys. Condens. Matter* **21**, 326006 (2009).
- [82] J. B. Pendry, *Phys. Rev. Lett.* **85**, 0 (2000).
- [83] J. Rekosova, R. Dosoudil, M. Usakova, E. Usak, and I. Hudec, *IEEE Trans. Magn.* **49**, 38 (2013).
- [84] D. Smith, W. Padilla, D. Vier, S. Nemat-Nasser, and S. Schultz, *Phys. Rev. Lett.* **84**, 4184 (2000).
- [85] B. Wood and J. B. Pendry, *J. Phys. Condens. Matter* **19**, 76208 (2007).
- [86] J. D. Jackson, *Classical Electrodynamics*, 3rd ed. (John Wiley & Sons, Inc., New York, 1999).
- [87] A. Sambale, S. Y. Buhmann, H. T. Dung, and D.-G. Welsch, *Phys. Rev. A* **80**, 51801 (2009).
- [88] K. Akamatsu, S. Adachi, T. Tsuruoka, S. Ikeda, S. Tomita, and H. Nawafune, *Chem. Mater.* **20**, 3042 (2008).
- [89] Mark Fox, *Optical Properties of Solids* (Oxford University Press, New York, 2001).
- [90] W. Cai, U. K. Chettiar, A. V Kildishev, and V. M. Shalaev, *Nat Phot.* **1**, 224 (2007).
- [91] M. Iwanaga, *Sci. Technol. Adv. Mater.* **13**, 53002 (2012).
- [92] M. M. and Z. Jakšić, *J. Opt. A Pure Appl. Opt.* **8**, 355 (2006).
- [93] J. Jose, *J. Phys. B At. Mol. Opt. Phys.* **40**, 497 (2007).
- [94] Z. J. and O. J. and Z. D. and C. Kment, *J. Opt. A Pure Appl. Opt.* **9**, S377 (2007).

- [95] C. Sohl, M. Gustafsson, and G. Kristensson, *J. Phys. D. Appl. Phys.* **40**, 7146 (2007).
- [96] F. Magnus, B. Wood, J. Moore, K. Morrison, G. Perkins, J. Fyson, M. C. K. Wiltshire, D. Caplin, L. F. Cohen, and J. B. Pendry, *Nat. Mater.* **7**, 295 (2008).
- [97] I. M. Lifshitz, *Reports Prog. Phys.* **133**, A750 (1966).
- [98] D. R. Smith and J. B. Pendry, *J. Opt. Soc. Am. B* **23**, 391 (2006).
- [99] C. R. Simovski, *J. Opt.* **13**, 13001 (2011).
- [100] S. Ramo, J. R. Whinnery, and T. Van Duzer, *Fields and Waves in Communication Electronics*, 2nd ed. (John Wiley & Sons, Inc., New York, 1984).
- [101] Ari Sihvola, *Electromagnetic Mixing Formulae and Applications* (The Institution of Engineering and Technology, London, 1999).
- [102] T. C. Choy, *Effective Medium Theory: Principles and Applications* (Oxford University Press, New York, 1999).
- [103] L. Onsager, *J. Am. Chem. Soc.* **58**, 1486 (1936).
- [104] P. Sheng and M. Gadenne, *J. Phys. Condens. Matter* **4**, 9735 (1992).